TWO PROBLEMS IN MANY BODY PHYSICS

I. Photon production: a probe of heavy ion collisions

II. Structure of matter in strong magnetic fields

Thesis by

Daniel Neuhauser

In Partial Fulfillment of the Requirements

for the Degree of

Doctor of Philosophy

California Institute of Technology

Pasadena, California

1987

(Submitted November 24, 1986)

To My Family

ACKNOWLEDGMENTS

It was a great pleasure to work under the supervision of Dr. S. E. Koonin. I thank him for his support, encouragement, and interest in my work. I also thank the following people with whom I held helpful discussions: Dr. R. Blandford, Dr. V. Brown, M. Butler, C. M. Chu, Dr. C. M. Ko, Dr. K. H. Langanke, D. Meredith, Dr. V. Pönisch, D. Wasson, Dr. K. Wolf, and Dr. M. Zirnbauer. Dr. Blandford first introduced me to atomic structure in strong fields. V. Pönisch supplied me with the radial wavefunctions code used in Part 1, C. M. Ko supplied me with the VUU code, and K. H. Langanke collaborated with me on the calculations in Part 2. This work was made possible by financial support from Caltech and the National Science Foundation.

ABSTRACT

In Part 1 we examine the theoretical framework for the use of photon spectra to probe heavy ion collisions. We first calculate single photon emission spectra from nuclear matter in the incoherent limit and combine them with the simplified participant-spectator model and with the semiclassical VUU model, to predict photon production cross sections in heavy ion collisions. The spectra differ from previous estimates based on a classical soft-photon approximation and lead to good agreement with experiment, except for an overall normalization factor of order (2-5), which we interpret as direct evidence for medium effects.

We then proceed to examine the Hanbury-Brown-Twiss correlation of high-energy photons emitted from heavy ion collisions. We find that both the polarization average and a possible coherent component complicate the extraction of the size and lifetime of the emitting source from the correlation function.

In Part 2 we calculate the binding energies of atoms and molecular chains in 10^{12} G magnetic fields using the Hartree-Fock method. Our calculations are the first self-consistent ones treating exchange properly for atoms heavier than helium in high fields. For $Z > 2$ at 10^{12}G and $Z > 4$ at 5×10^{12}G the isolated atom is energetically favored over the molecular chains.

TABLE OF CONTENTS

LIST OF TABLES

LIST OF FIGURES

PART 1

PHOTON PRODUCTION:

A PROBE OF HEAVY ION COLLISIONS

INTRODUCTION

The development of heavy ion accelerators has considerably expanded the forefront of nuclear physics. A little more than a decade ago, the highest attainable collision energies were 20-30 Mev per nucleon; nowdays, the limit is 2 GeV/A, and in the near future 50 GeV/A may be reached. These developments make possible the study of the transformation from collective to single-particle phenomena near the Fermi energy, E_F =38 MeV. At higher collision energies, where the single-particle aspect dominates, the colliding nuclei are in a fluid or gaseous state; from the experiments we hope to extract their equation of state, which for large atomic numbers should approach that of nuclear matter. At very high collision energies (100 GeV/A or more) we may be able to observe the transition to quark gluon plasma; we will not discuss that possibility here, but will rather limit ourselves to the relevant range for the equation of state studies, 50-2000 MeV/A.

The equation of state is desired because it is an elegant and concise description of the properties of nuclear matter. Moreover, heavy nuclei are the only example we have on earth of a large system of strongly interacting fermions; it is hoped that by comparing the experimentally extracted equation of state with the properties of few-nucleon systems, we may learn more about the many-body physics of such systems. In addition, the equation of state has astrophysical importance, as it influences supernovae evolution and neutron stars' abundance and structure.

To reach the goal of extracting the equation of state, one has to overcome a fundamental difficulty: the colliding system goes through expansion and breakup stages, so the most obvious probe, the distribution and yield of fragments and nucleons, is determined by the late stages of the expansion and cannot be used directly to study the equation of state. In principle, it should be possible to relate the maximum temperature and density to their values at breakup, but this requires a complete and reliable theory of heavy-ion reactions, and no such theory is available. The problem of breakup effects is common to all probes that use strongly interacting particles. We are therefore led naturally to examine the possibility of using photon spectra to probe heavy ion reactions.

High-energy photons ($E_\gamma > 50$ MeV) offer several distinct advantages as a probe of intermediate-energy heavy ion reaction dynamics. The photon-hadron coupling is weak ($\sim 1/137$), and therefore photons couple perturbatively to the well-defined electromagnetic current. Moreover, the photon mean-free-path exceeds by orders of magnitudes the size of the colliding system, so once photons are created they escape without absorption, and their spectrum is not complicated by the final state interactions or sequential decay processes suffered by hadronic fragments. They can therefore provide relatively clean information about the flow of nuclear matter during a collision, if they can be interpreted properly.

This part is organized as follows: after a review of the basic concepts in Chapter I, we present (Chapters II-III) a review of previous efforts to extract the equation of state. In Chapter II we give a brief survey of various probes that carry information on the high density stage, without losing it completely in the final stages.

The probes covered are: entropy production, momentum distribution of fragments, meson production (especially production below threshold), and two-particle correlations. The review is presented because, in our opinion, it is necessary to understand other efforts before we can fully appreciate the the relative merits and capabilities of the probe that we examine. In Chapter III we review some of the dynamical models that have been devised to describe the collision dynamics.

We then proceed to discuss our work on probing nuclear reactions with photons. In Chapter IV we present our calculation of the inclusive photon spectra in heavy ion collisions. This calculation uses the correct quantum mechanical nucleon-nucleon bremsstrahlung cross sections, which we calculate *systematically* for the first time. We find that the cross sections, and therefore the emission spectra, differ (sometimes by an order of magnitude) from previous estimates based on classical soft-photon approximations. Armed with the calculated cross sections, we study the effects of the collision dynamics on the spectra. These studies can be used to fit the collision dynamics when more experimental data become available.

In the last Chapter (V) we present our calculation of two-photon interferometry. This calculation extends previous work on pion correlations, in anticipation of experimental efforts to measure two-photon correlations.

I. BASIC CONCEPTS

I.1 Probing the equation of state of nuclear matter

The main motivation of studying heavy ion collisions at high and medium energies is to probe the nuclear matter equation of state; here we will outline the basic concepts relevant to this goal.

The equation of state is defined by

$$P = P(\rho, T), \tag{1.1}$$

where P, ρ, and T are the pressure, number density, and temperature of the excited nuclear matter. *

Fig. (1) shows the different phases of nuclear matter in the (ρ, T) plane and the regions that are probed by the three available methods to study the equations of state: monopole excitations, supernovae evolution, and heavy ion collisions. Monopole excitations ("breathing modes") of nuclei are observable only at very low temperatures and at near-equilibrium densities, so they can determine only the

* A word of caution: we follow the bad habit of others in this field and use the term "equation of state" interchangably to denote either Eq. (1.1) or its integrated form,[1]

$$U = U(\rho, T); \qquad P = \rho^2 \left.\frac{\partial U}{\partial \rho}\right|_S .$$

where U and S are the internal energy and entropy per nucleon.

curvature of the equation of state near equilibrium. But this method has the advantage of being the most accurate of the three, leading to compressibilities (the term is defined below) of $220 \pm 30\,\mathrm{MeV}$.[2]

Supernova theorists use a prescribed equation of state in their stellar evolution models. They then determine whether and how often a stellar evolution will end in a supernova, and what remains after the explosion. The equation of state is then fitted to lead to best agreement with observations. But there is a wealth of other physics that is relevant to the evolution, most notably nuclear reaction cross sections, which are not yet well known. Moreover, the physical processes are so complex that the calculations must include many approximations. As of 1986, the extracted equations of state were rather "soft" (i.e., the pressure is a slowly increasing function of density). During a supernova explosion matter is compressed to high densities, but temperatures remain "low" ($\sim 0.5\,\mathrm{MeV}$ [3]), so this method can, at best, explore the low-temperature equation of state.

In heavy ion reactions there are *two* collision parameters : energy and impact parameter. (Atomic number, A, is an additional parameter; however, nuclear forces saturate and therefore for large A the experiments should simply scale with A.) We could, in principle, then probe a large *two*-dimensional region of the phase plane. However, at high impact parameters only a small part of the nuclei participate in the collision, too small to resemble nuclear matter, and therefore this method can probe only a strip of phase space plane. Notice also that the interpretation of heavy ion collisions at very low collision energies is complicated by Coulomb interactions, angular momentum, and the finite size of the colliding nuclei, so that low-energy

reactions cannot be used to extract the equation of state near equilibrium. Since this is just the region that monopole excitations probe, it is impossible to compare directly the equation of state as extracted from heavy ion collisions and that extracted from monopole excitations. Only heavy ion collisions will be considered here, but it is important to remember that they probe only a small strip of the whole (ρ, T) plane. Notice also that inferring isospin-symmetric nuclear matter properties from heavy ion reactions is somewhat complicated by the neutron excess in heavy nuclei.

Often the temperature dependence of (1.1) is neglected,

$$P(\rho, T) \sim P(\rho, 0) \qquad U = U(\rho, 0). \tag{1.2}$$

For the nonrelativistic Fermi-gas, this approximation holds at high temperatures; at low temperatures, the dependence on T is also weak (T^2 rather than T). For nuclear matter at the range of temperatures and densities that are probed in heavy ion reactions, this approximation may or may not be valid. The discrepancies (or at least part of them)[1] between the equations of state that are extracted by different methods may be just an artifact of this approximation. For example, the high-temperature equation of state that heavy-ion reactions probe can be very different from the equation of state at the low temperatures in a supernova.

The anstaz (1.2) reduces the equation of state to a one variable equation, but sometimes this is expanded about the equilibrium density

$$U(\rho, 0) \sim \frac{K}{18} \frac{(\rho - \rho_0)^2}{\rho_0^2} + E_0, \quad \rho \sim \rho_0, \tag{1.3}$$

where ρ_0 ($0.15\,\mathrm{fm}^{-3}$), K, and E_0 (-16 MeV) are the nuclear-matter equilibrium

number density, compressibility, and binding energy, respectively. Typically , an equation of state with compressibility below 200 MeV is considered "soft," and above 250 MeV, "hard." Different studies suggest compressibilities in the whole range $100\,\mathrm{MeV} < K < 350\,\mathrm{MeV}$.[4] The form (1.3) is strictly valid only near equilibrium but is also often used far from equilibrium. Therefore, the remark made on the replacement (1.2) is even more appropriate here: much of the discrepancy among different methods that extract the equation of state may be just an artifact of the approximation employed.

I.2 Evolution of Heavy Ion Reactions

At intermediate and high energies, (see below), a heavy ion reaction can be schematically divided into four stages (see Fig. (2)). In the first stage the colliding nuclei approach each other and begin to penetrate, the density rises above equilibrium, the two nuclei heat, and pressure builds up. The pressure eventually stops the contraction (second stage), and the combined system stays near the maximum pressure point for a relatively long time.† The system then expands (third stage)

† The natural measure of the collision time is

$$\tau \sim \frac{2R}{v},$$

where R is the sum of the projectile and target radius, and v is the projectile velocity. The duration of the maximum density stage is expected to be an appreciable fraction $(0.2 - 0.3)$ of τ; for typical parameters, $R \sim 5 - 10\,\mathrm{fm}$ and $v \sim 0.3 - 1c$, that time may reach 20 fm/c.

and eventually breaks up into various fragments (fourth stage). At low energies some large fragments are observed, but as the collision energy is increased, the probability to emit large fragments is reduced, and the system breaks up mostly into nucleons with some additional light nuclei.

The high-density stage (the second) is the most relevant for the understanding of the equation of state, because the system stays for a long time around the same density and temperature, so it may (it is hoped) resemble a piece of hot, dense, and *static* nuclear matter. A large percentage of the theoretical and experimental work in this field is devoted to devising probes of this stage that will not be obscured by the subsequent evolution of the system. Chapter II describes some of these probes, and Chapters IV and V are devoted to a discussion of one of them, photon emission.

Before closing this chapter, let us comment on, and clarify, the nomenclature that we use. The reaction energy is denoted by its value per nucleon, E/A. The symbol E is reserved for the center-of-mass energy of two colliding nucleons inside the reacting system and is sometimes explicitly written as "E_{nn}." In the subsequent chapters we assume that the reaction is nonrelativistic, so that the colliding system contains only neutrons and protons. At relativistic collision energies ($E/A > 1$ GeV) other degrees of freedom are excited: mesons, deltas and higher resonances, strange particles, and for very high collision energies, even a quark-gluon plasma may form[6]. But we will restrict ourselves to the lower energy range, so the term "high-energy reactions" applies to energies that are considerably above the Fermi energy $E_F = 38$ MeV but are still not too relativistic: $E/A \sim 300 - 2000$ MeV. By "intermediate energy reactions," we mean reactions in which two-nucleon interactions and the

mean-field potential are both affecting the dynamics, $E/A \sim 50 - 300$ MeV. The effects of the mean-field potential and two-body collisions are described in more detail in Chapter III.

II. PROBES OF HEAVY ION REACTIONS

In this chapter we give a brief survey of various probes that carry information on the high-density stage, without losing it completely in the final stages. The probes covered are: entropy production, momentum distribution of fragments, meson production (especially production below threshold), and two-particle correlations. More complete lists of probes, with many references, can be found in Refs. (5, 7).

A word of caution is in order: in this chapter we repeatedly use the term temperature, even though temperature is strictly defined only in local thermal equilibrium. At low reaction energies the mean-free-path of nucleons is large, and local thermal equilibrium is not achieved, so that "temperature" should be replaced by "average energy."

Intuitively, one expects that most of the entropy in a collision will be created in the initial, more violent, stages of the reaction, and the final-states interactions will not change its value. Therefore, entropy should be a good probe of the high density stage. Siemens and Kapusta[8] first suggested measuring the entropy, S, by using the deuteron to proton ratio, R_{dp}. In chemical equilibrium the result they obtained is :

$$S = 3.95 - \log(R_{dp}). \tag{2.1}$$

A comparison of data on deuteron-proton ratio with recent theoretical calculations

seems to favor a stiff equation of state.[5]

The angular distributions of the emitted fragments is another possible probe.[5] The simplest way to characterize the angular distribution is by a collective flow angle, as in Fig. 3. The figure shows the dependence of the flow angle on the impact parameter, as predicted by the Nuclear Fluid Dynamics model. One can see that even for low impact parameters the flow angle is substantial, and this indicates that pressure plays an important role in the dynamics. For a long time this prediction was doubted, but it has been verified by recent data.[5] Unfortunately, the dependence of the flow angle on the equation of state is not large, so it is necessary to use the finer details of the observed angular distribution to distinguish between different equations of state.[9]

Pions are stongly interacting particles so that, in principle, they suffer from the same absorption effects that obscure the distribution of nucleons.[1] However, the total pion yield is fixed earlier than pion energy distribution. During the latest stages of the reaction nucleon-nucleon collisions do not have sufficient energy to create new pions, and due to the low density, pion-nucleon-nucleon collisions leading to pion absorption are rare; but pion-nucleon elastic collisions are common and bring the pions into thermal equilibrium with the nucleons. Therefore, the total pion yield is a good probe of the high-density stage. Kaons can also be used to probe heavy ion reactions.[10,11] Kaons have an advantage over pions in that they interact weakly with nucleons, so absorption effects are not so severe for them, and the kaon yields probe a more "primordial" stage of the reaction.

Subthreshold meson production is a very promising reaction probe.[10,11,12] The

term "subthreshold production" means production at nucleus-nucleus collision energies, per nucleon, that are smaller than the nucleon-nucleon threshold energy; i.e., two nucleons moving with the target and projectile velocity, respectively, do not have enough energy to create that meson. The most natural explanation of subthreshold production is the presence of high momentum "tails" in the nucleon momentum distribution. However, one could conceive of other production mechanisms: few-body collisions, where a few nucleons all share their energy to create the meson, meson-bremsstrahlung by the collective deacceleration of the colliding nuclei, and wide resonance excitations.[7] Indeed, it seems that pion subthreshold yields are too large to be explained by the high-energy tail of the nucleon distribution (especially when the energy is far below threshold), and are probably related to resonance excitations. On the other hand, it is believed that for kaons the alternative mechanisms will not be effective, at least for collision energies that are not too far below threshold. Because of the exponential decrease of the momentum distribution in high energies, the high-energy tail depends strongly on the maximum temperature of the system, so subthreshold kaon production should be a very good thermometer.

Many probes are useful only for central nucleus-nucleus collisions, because in collisions with high impact parameter the nuclei do not overlap strongly and essentially slide sidewards, so the combined system does not reach a high-density stage. For the measurements of the collective flow angle it is also necessary to identify the impact parameter of the collision, in order to study the dependence of the flow angle on the impact parameter. Thus, central and almost central collisions have to

be identified experimentally, out of the large background of high impact parameter collisions. Central collisions are more violent and create more fragments, so they can be selected by restricting measurements to events with large fragment multiplicity. The identification of high multiplicity events requires a 4π solid angle detector that will catch all emitted fragments, and these detectors have to be fast enough to allow identifications of individual reactions. Such sophisticated detectors have become available only in the last few years.[13] They also allow a measurement of two (and many) particle correlations,[14] which, when applied to identical particles, can be used to infer the properties of the region that emits these particles (Chapter V explains this method, pioneered by Hanbury-Brown and Twiss[15]).

III. MODELS OF HEAVY ION REACTION DYNAMICS

It is unrealistic to hope for a *complete* description of a nucleus-nucleus collision in terms of the interacting nucleons. Even in the nonrelativistic approximation we cannot solve numerically the quantum $N-$body problem for more than three particles. Therefore, to describe a nucleus-nucleus collision with complex nuclei that contain a large number of nucleons, we have to resort to approximations. In this chapter we briefly describe and motivate some of the most popular approximations: time-dependent Hartree-Fock (TDHF), [16] the Cascade,[17] the Vlasov-Uehling-Uhlenbeck equation for the average one-body phase space distribution function (VUU),[18] Nuclear Fluid Dynamics,[5] and static fragmentation models.[5,19] For a more complete review of the topic of this chapter, we refer the reader especially to Ref. (5), which includes a detailed comparision of theoretical predictions of different methods with the experimental data. A critical examination of the basic assumptions that enter into different models can be found in Ref. (20).

At very low collision energies, heavy ion reactions are well described by the time-dependent Hartree-Fock approach, where the total wavefunction of the reacting system is approximated by a Slater determinant of time-dependent single-nucleon orbitals. Slater determinants do not include the correlations that elementary nucleon-nucleon collisions induce, and the motion of nucleons is governed only by the smooth (time-dependent) mean-field potential. TDHF is therefore unsuit-

able to describe reactions whenever two-nucleon collisions dominate the dynamics. TDHF is a good approximation only at very low collision energies, $E/A \ll E_F = 38$ MeV, because at these energies the nucleon distribution is similar to the ground-state distribution (i.e., nearly fully occupied orbitals below the Fermi energy, E_F, nearly empty orbitals above E_F), so that most two-nucleon collisions are forbidden by the Pauli principle.

TDHF is successful in describing quantitatively many phenomena at low collision energies: fusion, compound nucleus formation, strongly damped collisions, and dissipation. However, at higher energies ($E/A > 10$ MeV) TDHF fails because it ignores two-nucleon correlations. For example, TDHF predicts that nuclei should become almost transparent for high collision energies, $E/A > E_F$, while in reality, collisions at high energies are extremely violent and produce many fragments. TDHF is the only successful fully quantum approach to heavy ion reaction dynamics, and, at intermediate and high collision energies where TDHF fails, we must resort to classical or semiclassical approximations.

One of the most popular semiclassical approximations of the heavy ion reaction dynamics is the cascade model, originally developed to describe high-energy proton-nucleus reactions.[17,21] In this model a nucleus-nucleus reaction is modeled as a series of sequential elementary nucleon-nucleon collisions. Nucleons are treated as point-like particles that move along straight-line trajectories between collisions. A collision occurs whenever two nucleons get within a distance "r_0" of each other, where πr_0^2 is the nucleon-nucleon reaction cross section, and $\sigma_{nn}(E_{cm})$ is the nucleon-nucleon cross section in free space, which depends on the energy E_{cm} of the two

nucleons in their center-of-mass. The directions of the nucleons that emerge from a collision are chosen randomly according to the angular distribution of the nucleon-nucleon cross section, $d\sigma_{nn}/d\Omega$.

The cascade is accurate in the dilute gas limit when nucleons reach their asymptotic scattering states between successive collisions, and indeed its *qualitative* success in describing heavy ion reactions is due to the low density of nucleons in nuclear matter (nucleons occupy about one-fourth of the volume). However, nuclear matter is not dilute enough to justify *quantitatively* the approximations inherent in the cascade, unless the collision energies are high. To see this, notice that the condition that nucleons reach their asymptotic scattering states between collisions is equivalent to the condition for the validity of the classical dynamics approximation,

$$p\,r \gg \hbar, \tag{3.1}$$

where p and r are typical values of the relative momentum and spatial separation of neighboring nucleons. A typical value for r is 1.5 fm, and it follows that the condition is satisfied only when a typical nucleon's energy exceeds ~300 MeV. Another deficiency of the cascade at intermediate collision energies is that it does not include the effects of Pauli blocking. The blocking is important up to very high collision energies; for example, a study with the VUU of blocking effects shows that for a collision of symmetric nuclei at $E_{LAB}/A = 137$ MeV, 80 % of the nucleon-nucleon collisions are blocked. The cascade also does not include the effects of the mean-field potential and is therefore unsuitable for a direct study of the equation of state.[1]

Some attempts have been made to include Pauli blocking and mean-field potential effects in the cascade model. However, these effects are incorporated much

more naturally in the VUU approach. This approach describes the reaction by the evolution of the average single-particle phase space distribution function (average number of particles per unit three-momentum and volume) - $f(\mathbf{x},\mathbf{p},t)$. This definition of f is meaningful only in the classical limit, where one can define the distribution in x and p spaces simultaneously. The proper quantum-mechanical extension was first given by Wigner[5] ($\hbar = c = 1$):

$$f(\mathbf{x},\mathbf{p},t) = \frac{1}{4}\int d\mathbf{s}\, e^{i\mathbf{p}\cdot\mathbf{s}} \langle \mathbf{x} + \frac{\mathbf{s}}{2}|\rho|\mathbf{x} - \frac{\mathbf{s}}{2}\rangle = \frac{1}{4}\int d\mathbf{q}\, e^{-i\mathbf{q}\cdot\mathbf{x}} \langle \mathbf{p} + \frac{\mathbf{q}}{2}|\rho|\mathbf{p} - \frac{\mathbf{q}}{2}\rangle. \quad (3.2)$$

Here, ρ is the (time-dependent) spin-isospin summed density operator, and we assume that the colliding matter is spin-isospin symmetric. The extension to neutron excess in real nuclei is trivial. The Wigner function is not positive-definite and therefore is not a distribution; however, its integral is positive-definite:

$$4\int \frac{d\mathbf{p}}{(2\pi)^3} f(\mathbf{x},\mathbf{p},t) = \rho(\mathbf{x},t), \quad (3.3a)$$

$$4\int \frac{d\mathbf{x}}{(2\pi)^3} f(\mathbf{x},\mathbf{p},t) = \rho(\mathbf{p},t). \quad (3.3b)$$

In the classical approximation, f satisfies the Boltzman equation[5]

$$\frac{df}{dt} \equiv \frac{\partial f}{\partial t} + \frac{d\mathbf{x}}{dt}\frac{\partial f}{\partial \mathbf{x}} + \frac{d\mathbf{p}}{dt}\frac{\partial f}{\partial \mathbf{p}} = \frac{\partial f}{\partial t} + \frac{\mathbf{p}}{m}\frac{\partial f}{\partial \mathbf{x}} - \frac{\partial U(f)}{\partial \mathbf{x}}\frac{\partial f}{\partial \mathbf{p}} = \text{Collision term}, \quad (3.4)$$

where m is the mass of a nucleon and U is the mean-field potential, given by the equation of state. In the absence of collisions, (3.4) is reduced to the Liouville equation,

$$\frac{df}{dt} = 0. \quad (3.5)$$

Uehling and Uhlenbeck's ansatz for the collision term was

$$\frac{df_1}{dt} = \int \frac{\mathbf{dp_2}\,\mathbf{dp_1'}\,\mathbf{dp_2'}}{(2\pi)^6} \frac{d\sigma}{\mathbf{d}(\mathbf{p_{12}'}/2)} |\mathbf{v}_{12}|\,\delta(\mathbf{p}_1 + \mathbf{p}_2 - \mathbf{p_1'} - \mathbf{p_2'}) \\ [-f_1 f_2 (1 - f_1')(1 - f_2') + f_1' f_2' (1 - f_1)(1 - f_2)] \quad (3.6)$$

where we abbreviate: $f_1 \equiv f(\mathbf{x}, \mathbf{p_1}, t)$, $f_2 \equiv f(\mathbf{x}, \mathbf{p_2}, t)$, etc., and label f by the subscript "1" in order to show the symmetry of the collision term. $\mathbf{v}_{12}$ and $\mathbf{p}_{12}$ are the relative velocity and momentum of two nucleons with momenta $\mathbf{p}_1$ and $\mathbf{p}_2$, and $d\sigma/\mathbf{dp}$ is the spin-isopin summed nucleon-nucleon differential cross section in free-space. The first term in the square brackets represents scattering of two nucleons that drives one of them outside the phase space cell centered around $(\mathbf{x}_1, \mathbf{p}_1)$, and the second term represents scattering into that phase space cell. The $1 - f$ terms are due to Pauli blocking. Notice that collisions are really not instantaneous and take place over an extended region of space-time, and therefore (3.6) is meaningful only when the phase space distributions are smoothly varying over space and time.

Eq. (3.6) can be obtained either from the semiclassical limit of the TDHF if the Born approximation is assumed,[5] or from an ensemble average of the cascade model with modifications to account for the mean-field potential and the Pauli blocking.[18] Ultimately, the justification of the VUU model is phenomenological, since the fundamental conditions for the validity of the VUU are not fulfilled in heavy ion reactions, unless the collision energies are very high. Therefore, it is probably better to extract the fundamental input to the VUU - the differential nucleon-nucleon cross section - from heavy-ions experiments, rather than to use the cross sections in free space, as in the original ansatz. Indeed, we know from the Bruckner-Hartree-Fock theory of nuclear matter that nucleon-nucleon cross sections

in infinite nuclear matter are smaller (by a factor of ~ 2) than cross sections in free-space. The "best" values of nucleon-nucleon cross sections in heavy ions reactions are not yet known, but with the improvement of experimental probes they will most probably be extracted soon. As we show below (Section IV.6), photon emission can conceivably be used to extract the cross section in nuclear medium; comparison of VUU simulations with preliminary data shows that the cross section is decreased by a factor of 2-5.

The VUU is successful in describing single particle distributions in intermediate- and high-energy heavy-ion reactions. (At high energies a relativistic extension of Eqs. (3.4, 3.6) is used.[5]) However, since it describes only the evolution of the average single-particle distribution and not of the two-particle distributions (or, in general, the *many*-particle distributions), it is not capable of describing any phenomena that depend on fluctuations. Most importantly, it cannot describe the final stage (fragmentation) in a heavy ion reaction. This obviously limits the number of observables that can be used with the VUU to study the equation of state, because many processes that depend strongly on the central density also have a strong dependence on fluctuations (pion production yields, for example).

When the mean-free-path of a nucleon is much shorter than the size of the colliding nuclei and the scale of temperature variations,

$$\lambda \ll L, \qquad \lambda \ll \frac{T}{\partial T/\partial r} \ , \tag{3.7}$$

the colliding system reaches local thermal equilibrium (except near the boundaries), and the momentum distribution has the Fermi-Dirac form

$$f(\mathbf{x},\mathbf{p},t) = \left(1+\exp\left(\left(\sqrt{p^2+m^2}+\mu(\mathbf{x},t)\right)/T(\mathbf{x},t)\right)\right)^{-1}, \tag{3.8}$$

where the chemical potential μ is determined by the local density and temperature. In this local equilibrium limit, the VUU equations reduce to the familiar Euler equations.[5] These are partial differential equations in four dimensions (space+ time) and are therefore more tractable numerically than the VUU equations in seven dimensions. However, fluid dynamics is not valid at intermediate energies, because Pauli blocking increases the nucleon mean-free-path. For example, a study with the VUU shows that for a collision of similar nuclei at $E_{LAB}/A = 300$ MeV, 60 % of the nucleon-nucleon collisions are blocked. The Pauli-blocked cross section is therefore

$$\lambda_{blocked} \sim \frac{\lambda}{\langle 1-f \rangle} \sim \frac{1}{\langle 1-f \rangle \sigma \rho}, \tag{3.9}$$

where σ is the nucleon-nucleon cross section in nuclear matter, and ρ is the nuclear matter density. At these collision energies, a reasonable estimate for these parameters are $\sigma \sim 50\,\mathrm{mb}$, $\rho \sim 0.2\,\mathrm{fm}^{-3}$, and therefore $\lambda_{blocked} \sim 3\,\mathrm{fm}$. A typical radius of the colliding system for heavy ions is $L \sim 10$ fm , so local equilibrium (Eq. 3.7) is not fully achieved.

All models described so far (TDHF, Cascade, VUU, and Nuclear Fluid Dynamics) can be solved only numerically, so they may be inappropriate in some cases where a simple physical characterization of the collision is sought. Moreover, in many cases data are not sufficiently detailed, and can be explained with the same (sometimes limited) success by other models with differing physical assumptions, so that use of sophisticated models is neither necessary nor justified.

The participant-spectator model is one of the more popular qualitative descriptions of heavy ion collisions. This model assumes that in each collision an equilibrated "fireball" is formed from all participant nucleons (Fig. 4). The tem-

perature of the fireball is determined by the condition that all of the collision energy is converted to thermal energy. The fireball expands adiabatically (the nucleons do not collide), and, in the nonrelativistic, nondegenerate, approximation

$$f(\mathbf{x},\mathbf{p},t) = \frac{A}{4(mT_0)^{\frac{3}{2}}R_0^3}\exp\left(-\frac{1}{2mT_0}p^2 - \frac{1}{2R_0^2}(\mathbf{r}-\mathbf{p}t/m)^2\right), \tag{3.10}$$

where T_0, R_0 are the fireball initial temperature and radius, and A is the average number of participant nucleons. The factor of 4 is due to isospin-spin degeneracy. The evolution in time of the fireball temperature (related to the coefficient of p^2) and radius is easily derived from (3.10)

$$T(t) = \frac{T_0}{1+T_0t^2/mR_0^2}$$

$$R(t) = \frac{R_0}{\sqrt{1-T_0t^2/mR_0^2}}. \tag{3.11}$$

For very large times ($t \sim R_0\sqrt{m/T_0}$) the fireball description breaks down as the radius of the fireball diverges.

The participant-spectator model describes qualitatively the single nucleon distribution in the later stages of the collision, and the final distribution of emitted nucleons (but not of clusters). But since the model assumes complete and immediate equilibration , it cannot be used reliably to predict observables that depend mainly on the initial stage of the interaction.

In this chapter we have concentrated on dynamical models, i.e., models that describe the temporal evolution of the system. The complex fragmentation process is best described by statistical models, and among them the most conceptually simple is of thermodynamical breakup.[19] In this model all different events (after

breakup) are assumed to fill the $6N$ phase space homogeneously (N is the total number of nucleons participating in the reaction). Therefore, the probability that a cluster with M nucleons is formed is proportional to the phase space volume that is occupied by events that include at least one such cluster. Other fragmentation models are based on radically different assumptions; e.g., glass-shattering and even percolation models have been suggested. It is not possible yet to pick the "right" fragmentation model, because they all fit the available data.[22] Since the main topic of this part of the thesis is production of photons in heavy ion reactions, a process that occurs mainly in the high-density stage of the reaction, the problem of the cluster formation in the last stages will not be discussed further.

IV. SPECTRA OF PHOTONS FROM HEAVY ION REACTIONS

IV.1 Introduction

Photon emission data are still scarce and nondefinitive. Spectra were measured for the systems C+U and C+C at 84 MeV/A,[23] C+Pb and C+N at 20, 30, and 40 MeV/A,[24] N+Ni at 35 MeV/A,[25] Kr+Au at 44 MeV/A,[26] and for few other systems at lower collision energies. Different groups get contradictory results. Some groups report isotropic photon distributions, while others report dipole shapes; absolute yields are also different, sometimes by an order of magnitude. But all sets of data show exponentially falling spectra, and for many sets the falloff is more gentle for higher photon energies ($E_\gamma \sim 100$ MeV) than for lower energies (Fig. 5). As shown below, both features emerge from our calculations. As new experiments with higher resolution will most probably soon resolve the discrepancies, we will not describe here further the data or the experiments.

Historically, the first theoretical model for high-energy photon emission in heavy ion collisions invokes bremsstrahlung emitted by coherent deacceleration of the colliding nuclei during the initial stages of a collision.[12] Such a model leads to a quadratic dependence of the photon yield on the nuclear charge, a spectrum whose hardness depends upon the deacceleration timescale, and, most importantly, a strongly anisotropic (mixture of dipolar and quadrupolar) angular distribution. As we explained, it is not yet clear whether the last prediction is confirmed by data.

Moreover, in order to fit the data, the coherent bremsstrahlung approach must assume very short deacceleration times must be assumed ($\sim 0.1\tau_r$; see footnote in p. 8). However, such short times are not supported by experiment or simulation. In any event, other emission mechanisms must be considered before coherent bremsstrahlung can be firmly established.

A thermal or statistical picture is, perhaps, the opposite limit. Here, each volume of space-time occupied by hadrons during the collision emits photons at a rate determined by its local conditions (density, temperature, etc.), and the net experimental spectra are the superposition of these many incoherent contributions. Note that this does *not* imply that the photons emitted from each space-time volume are in thermal equilibrium with the hadrons there (i.e., have a blackbody spectrum at the appropriate temperature), as the photon mean-free-path is very large. Rather, the number and spectrum of photons emitted from a given volume are determined by the nature of the elementary nucleon-nucleon collision processes that occur within it.

When the classical formula for photon production is used (i.e., the proton current-operator is replaced by a delta function), the transition between the coherent and statistical limits can be clearly seen. However, we show below that calculations based on the classical approximation do not give quantitatively correct answers, as the nucleus-nucleus collisions in which a photon is emitted are quantum-mechanical in nature.

In this chapter, we explore the implications of a purely thermal picture of high-energy photon emission on the inclusive photon emission spectrum (two-photon

correlations are considered in the next chapter). Clearly, two ingredients are necessary to calculate the photon spectra: *i)* the conditions of the nuclear matter at each space-time point during the collision, and *ii)* the number and spectrum of photons emitted by nuclear matter at a given temperature and density. The first of these requires a model of the collision dynamics, and here we use both the participant-spectator model and the VUU (Chapter III). The second ingredient we calculate, for the first time, below.

The balance of this chapter is organized as follows. In Section 2, we relate, under certain plausible assumptions, the photon spectrum from nuclear matter to the elementary nucleon-nucleon bremsstrahlung cross sections. In Section 3, we present systematic calculations of these cross sections and use them to calculate nuclear matter emission rates. In Section 4 we compare the rates to the classical formulas. In Section 5, we combine these rates with the fireball model and compare with selected experimental data. Finally, in Section 6 we combine the rates with the more realistic VUU model, and compare with data and results from previous VUU simulations that were based on a phenomenologically fitted expresssion for the elementary emission cross section.

IV.2 Incoherent photon emission from heavy ion collisions and from nuclear matter

Neglecting the coherent current, the emission of photons in a nuclear collision is described by a local differential rate of emission, $d^7N/d^4x\,dk\,d\Omega$ (number of photons with energy k and solid angle Ω emitted per space-time volume, d^4x). The impact

parameter averaged photon production cross section in a heavy ion collision is then

$$\frac{d\sigma_\gamma}{dk\,d\Omega} = \int 2\pi b\,db \int \frac{d^7N}{d^4x\,dk_d\,d\Omega_d}(k_d, f)\,\frac{k}{k_d}\,d^4x. \tag{4.1}$$

Here, b is the nucleus-nucleus impact parameter, f is the single nucleon momentum distribution at the space time point $(\mathbf{r}, t)$, and k_d and Ω_d are the photon energy and solid angle, respectively, Doppler-shifted to the frame moving with the nucleons local average velocity; the factor k/k_d is the Jacobian of the Doppler transformation. The differential emission rate depends on the momentum distribution of emitting nucleons at the point $(\mathbf{r}, t)$, which is in turn a function of the nucleus-nucleus collision energy and impact parameter. Since the photon emission spectrum is falling rapidly for high photon energies, we cannot ignore the Doppler shifting of the photons.

Eq. (4.1) is valid only when the emitted photons are not absorbed in the colliding matter. It is easy to see that this condition is satisfied in heavy ion reactions: the small electromagnetic coupling constant and the large proton mass imply that the Thompson cross section, typical for the interaction of photons with protons,[28] is very small,

$$\sigma_{\gamma P} \equiv \frac{8\pi}{3}\frac{e^4}{m^2} \sim 0.2\,\mu\text{b}, \tag{4.2}$$

where e and m are the proton charge and mass. A typical value for the proton density in heavy ion collision is $\rho_P \sim \rho_0/2 \sim 0.1\,\text{fm}^{-3}$, so the photon mean-free-path is

$$\lambda_\gamma \sim \frac{1}{\rho_P\,\sigma_{\gamma P}} \sim 5 \times 10^5\,\text{fm}, \tag{4.3}$$

exceeding by orders of magnitude the size of the colliding ions, $L \sim 10$ fm.

The differential spectrum is calculated by approximating locally the emitting region as a piece of nuclear matter with the same momentum distribution function and average velocity. To calculate the rate and spectrum of photons emitted from the nuclear matter, we consider a uniform spin-isospin symmetric system characterized by the single-particle momentum distribution $f(\mathbf{p})$ (see Eq. 3.2).

We assume that photons are emitted as the result of incoherent nucleon-nucleon bremsstrahlung processes (P+N $\rightarrow$ P+N+γ, P+P$\rightarrow$ P+P+γ) in which nucleons 1 and 2 with initial momenta $\mathbf{p}_{1i}$ and $\mathbf{p}_{2i}$ collide to produce a photon with momentum $\mathbf{k}$ while changing their momenta to $\mathbf{p}_{1f}$ and $\mathbf{p}_{2f}$. The differential rate of emission can then be written as

$$\frac{d^7N}{d^4x\,dk\,d\Omega} = \frac{8}{4\pi}\int \frac{\mathbf{dp}_{1i}}{(2\pi)^3}\frac{\mathbf{dp}_{2i}}{(2\pi)^3} f(\mathbf{p}_{1i})\, f(\mathbf{p}_{2i})\, v_{12i}\, \frac{d\bar{\sigma}}{dk}\,. \tag{4.4}$$

Here, v_{12i} is the initial relative velocity of the colliding nucleons and $d\bar{\sigma}/dk$ is the angle-integrated, Pauli-blocked nucleon-nucleon bremsstrahlung cross section:

$$\frac{d\bar{\sigma}}{dk} = \frac{k^2}{(2\pi)^3}\,\frac{1}{v_{12i}}\int d\Omega_k \frac{\mathbf{dp}_f}{(2\pi)^3}\,(1-f(\mathbf{p}_{1f}))(1-f(\mathbf{p}_{2f}))\,|T_{fi}|^2\,2\pi\,\delta(E_i-E_f-k). \tag{4.5}$$

In this expression, $|T_{fi}|^2$ is the square of the photon production amplitude (averaged over isospin and initial spins and summed over the final nucleon spins and photon polarizations), and $\mathbf{p}_f$ is the relative momentum of the outgoing nucleons:

$$\mathbf{p}_{f\,1,2} = \frac{\mathbf{P}_f}{2} \pm \mathbf{p}_f, \qquad \mathbf{P}_f = \mathbf{P}_i - \mathbf{k}, \tag{4.6}$$

so for fixed incoming momentum, $d\Omega_{cm\,f} = d\Omega_k$. Due to the approximate isotropy of the strong interaction cross section and the smooth form of the amplitude, it is a good approximation to replace the Pauli blocking factors by their average:

$$\frac{d\bar{\sigma}(E,k,\mathbf{p}_{1f},\mathbf{p}_{2f})}{dk} \simeq \frac{d\sigma_{free}(E,k)}{dk}\int (1-f(\mathbf{p}_{1f}))(1-f(\mathbf{p}_{2f}))\frac{d\Omega_k}{4\pi}\frac{d\Omega_f}{4\pi}\,, \tag{4.7}$$

where $d\sigma_{free}/dk$ is the nucleon-nucleon bremsstrahlung cross section in free space.

In closing this section, we note that Eq. (4.4) neglects the effects of coherent photon production in different elementary collisions, as it adds cross sections rather than amplitudes.[12,29,30] Very energetic photons (higher than 50 Mev) are produced incoherently since the phase factor, e^{ikt}, varies rapidly between collisions. [The time between the successive collisions a nucleon suffers is $\sim x/v \sim 2\,\mathrm{fm}/0.3\,\mathrm{c} \sim 1/(30\mathrm{Mev})$, x is the mean-free-path and v is a typical nucleon velocity.] However, if the colliding nuclei deaccelerate abruptly in the initial collision phase, adjacent nucleons will slow down coherently and the coherent electromagnetic current will be large compared with the incoherent cross section we have calculated, even for hard photons. The relative strength of the coherent and incoherent components depends crucially on the heavy-ion collision dynamics. These two components might be distinguished by the marked angular dependence of the coherent component, or by two-photon interferometry (Chapter V).

IV.3 The nucleon- nucleon bremsstrahlung cross section

We now turn to the evaluation of the elementary nucleon-nucleon bremsstrahlung cross section appearing in Eq. (4.7). For the photon energies of interest (less than 150 MeV), the dipole approximation is adequate and, in this limit, the proton-proton (and obviously neutron-neutron) cross sections vanish identically. The isospin-averaged cross section is then one-half of the neutron-proton value. (However, our calculations of neutron-proton collisions do take into account the much smaller multipoles beyond dipole through a partial-wave expansion of the nucleon wavefunctions.)

Theoretical and experimental interest in photon bremsstrahlung from nucleon-

nucleon collisions flourished in the late sixties and early seventies, because it was hoped that this process could be used to extract the "right" nuclear potential.[31] This is because the strong interaction is not constrained to conserve energy in a bremsstrahlung process. Only the combined processes, strong interaction between the nucleons and photon emission from one of the interacting nucleons, conserve the total energy. In other words, bremsstrahlung emission depends on the off-shell matrix elements of the strong interaction, unlike elastic nucleon-nucleon cross sections, which depend only on the on-shell elements, as shown schematically in Fig. 6. The usual procedure of fitting nuclear potentials to phase shifts in elastic collisions can accommodate many physically different nucleon-nucleon potentials, and researchers hoped to distinguish between them by bremsstrahlung. However, eventually, explicit calculations for many potentials showed that potentials that fit the elastic scattering data also give bremsstrahlung cross sections that are almost identical (they differ by less than two percent); on the other hand, experimental measurements have large uncertainties, twenty percent or more, because of the small emission probabilities (due to the small electromagnetic coupling constant).[32,33]

Notice that for our purposes it is fortunate that bremsstrahlung calculations show almost no dependence on the nucleon-nucleon potential, because this implies that our predictions are independent of the nuclear potential that we use. Ideally we should use experimental cross sections, but these are too scarce and uncertain.

There have been several previous calculations of neutron-proton photon production cross sections.[32] These were oriented largely toward direct experimental measurements of photon-production in two-nucleon collisions. Only differential cross sections for several specific emission angles were presented and then only for the case where all of the momenta of the incoming and outgoing particles lie in the same

plane. These results are clearly insufficient in view of the complete and systematic values of the angle-integrated cross section that we need to evaluate the rates (4.4). We have therefore written a computer code using the formalism and methods of Ref. 32, although with a variation that allows us to extract the angle-integrated cross section directly. We evaluate the photon production amplitude in a neutron-proton collision within the generalized Born approximation.[32,34] In this non-relativistic formulation, the strong interaction is treated nonperturbatively. Coupling to the photon is taken only to first order in the electromagnetic coupling constant. The amplitude for photon emission in a nucleus-nucleus emission is

$$T_{fi} = \langle \psi_f^- | \delta H | \psi_i^+ \rangle, \tag{4.8}$$

where ψ^+ , ψ^- are the usual two-nucleon scattering wavefunctions of the strong-interaction Hamiltonian, satisfying outgoing and incoming boundary conditions. The indexes i, f refer to the initial and final nucleons, respectively. δH is the difference between the full Hamiltonian including the electromagnetic coupling and the strong interaction Hamiltonian alone:

$$\delta H = H_{em+N} - H_N = \sum_{l=1,2} \frac{-e_n \mathbf{p}_n \cdot \mathbf{A}(\mathbf{r}_n)}{m_n} - \mu_n \mathbf{S_n} \cdot \mathbf{B}(\mathbf{r}_n) + i\sqrt{\frac{2\pi}{k}}\, \epsilon \cdot [e_n \mathbf{r_n}, V_N] + O(kR_{n.l.}), \tag{4.9}$$

where n labels the colliding nucleons, and $\mathbf{r_n}$, $\mathbf{p_n}$, m_n, e_n, μ_n, and $\mathbf{S}_n$ are the position, momentum, mass, electrical charge, magnetic moment, and spin of the $n-$th nucleon, respectively. k and ϵ denote the photon energy and polarization. $\mathbf{A}$ and $\mathbf{B}$ are the vector potential and magnetic field of the photons

$$\mathbf{A}(\mathbf{r}_n) = \sqrt{\frac{2\pi}{k}}\, \epsilon\, (e^{-i\mathbf{k}\cdot\mathbf{r}_n} a_k^+ + H.C.).$$

$$\mathbf{B} = \nabla \times \mathbf{A} \tag{4.10}$$

$R_{n.l.}$ is the range of the non-local parts of the nuclear potential. The calculation is facilitated by transforming to the nucleons' center-of-mass and relative coordinates,

$$\mathbf{r}_{1,2} = \mathbf{R} \pm \frac{\mathbf{r}}{2}.$$

In the nonrelativistic approximation, the nucleons' center-of-mass remains fixed during the collision, so it can be fixed at $\mathbf{R} = 0$.

The right-hand side of (4.9) includes the usual terms associated with the nucleons' momenta and spins, as well as a term due to the non-locality and exchange nature of the nucleon-nucleon interaction. A physical interpretation of the latter is that, in a neutron-proton collision, the direction of the electromagnetic current is changed if the nucleons are exchanged. Further details can be found in Ref. 32.

For our numerical calculations, we perform a partial-wave expansion of the initial and final two-nucleon wavefunctions and the photon plane wave, so that the amplitude has an explicit spherical-harmonic dependence upon the final nucleon and photon momenta. Quantizing the nuclear spin along the photon axis, we find that the two-nucleon wavefunction in the center-of-mass is:

$$\psi^{+(-)}_{\mathbf{p}S\nu} = \sum C^{l\,S\,J}_{m\nu M}\ (y^m_l(\hat{\mathbf{p}}))^*\ Y^M_{J\lambda S}(\hat{\mathbf{r}})\ \psi^+_{p\lambda lJS}(r), \tag{4.11}$$

where $\mathbf{p}$ and $\mathbf{r}$ are the relative momentum and position in the center of mass, S is the total spin, and ν is the spin projection along k. In (4.11) we have introduced the usual Clebsh-Gordan coefficients, the spherical harmonics, and the spin angle functions. The factor $e^{i\mathbf{k}\cdot\mathbf{r}/2}$ in A is also decomposed in partial waves:

$$e^{i\mathbf{k}\cdot\mathbf{r}/2} = \sum_l \sqrt{4\pi(2n+1)}\, i^n j_n(kr/2) y^0_n(\hat{\mathbf{r}}), \tag{4.12}$$

where $\mathbf{k}$ is taken parallel to the z axis. V_N is eliminated from (4.8) using

$$V_N|\psi^{+(-)}\rangle = \left(\frac{\triangle}{m} + E\right)|\psi^{+(-)}\rangle, \tag{4.13}$$

where E is the total center-of-mass energy of the colliding nucleons. The neutron-proton isospin wavefunction is decomposed in the total isospin (I) basis

$$|N\rangle\,|P\rangle = |\,\frac{1}{2}\,\rangle\,|-\frac{1}{2}\rangle = \frac{|I=1,I^z=0\rangle + |0,0\rangle}{\sqrt{2}}, \tag{4.14}$$

and the total wavefunction is symmetrized

$$|\psi_{\mathbf{p}S\nu I}\rangle \to \frac{|\psi_{\mathbf{p}S\nu I}\rangle - (-1)^{I+S}|\psi_{-\mathbf{p}S\nu I}\rangle}{\sqrt{2}}. \tag{4.15}$$

In the partial wave expansion (4.11), the symmetrization induces a factor

$$\frac{1-(-1)^{I+S+l}}{\sqrt{2}} = \begin{cases} \sqrt{2} & l+S+I \text{ odd;} \\ 0 & l+S+I \text{ even.} \end{cases} \tag{4.16}$$

The amplitude is evaluated for positive photon helicity. By symmetry, the angle-averaged cross section is independent of helicity. The positive helicity components of $\mathbf{r}$ and $\mathbf{p}$ are

$$\epsilon^+ \cdot \mathbf{r} \equiv r^+ = \sqrt{\frac{4\pi}{3}}y_1^0$$

$$\epsilon^+ \cdot \mathbf{p} = -i\nabla^+ = -i\sqrt{\frac{4\pi}{3}}\left[y_1^1(\frac{\partial}{\partial r} - \frac{L_z}{r}) + y_1^0\frac{L^+}{r}\right], \tag{4.17}$$

where here (and in the following) we adopt the convention that a spherical harmonic with no arguments refers to $\hat{\mathbf{r}}$, $y_l^m \equiv y_l^m(\hat{\mathbf{r}})$.

Inserting $(4.9 - 4.16)$ into (4.8), we easily see that the resulting amplitude will have the form

$$T_{fi} = \sum B_{\nu\, S\, l\, m\, I}^{\nu' S' l' m' I'}(p_i, p_f)\; y_{l'}^{m'}(\hat{\mathbf{p}}_f)\;\; (y_l^m(\hat{\mathbf{p}}_i))^*\,, \tag{4.18}$$

where a lengthy but straightforward calculation shows that

$$B^{\nu' S' l' m' I'}_{\nu\, S\, l\, m\, I} = \left(\sqrt{2}\right)^2 \sqrt{\frac{2\pi}{k}} \sum C^{lSJ}_{m\nu M} C^{l'S'J'}_{m'\nu'M'} \langle Y^{M'}_{J'\lambda'S'} | \Xi | Y^{M}_{J\lambda S} \rangle,$$

where

$$\begin{aligned}
\Xi = & \\
& \sum_n \left[\frac{i}{m} \sqrt{\frac{4\pi}{3}} \delta_{SS'} \left((-i)^n \langle I' | e_1 | I \rangle - i^n \langle I' | e_2 | I \rangle \right) \left(y^0_n y^1_1 G_1 + (y^0_n y^0_1 L^+ - y^0_n y^1_1 L_z) G_2 \right) \right. \\
& \left. + k G_3 y^0_n \left((-i)^n \langle I' | \mu_1 | I \rangle S^+_1 + i^n \langle I' | \mu_2 | I \rangle S^+_2 \right) \right] \sqrt{4\pi(2n+1)} \\
& - \delta_{I'+I,1} \frac{i}{2} \sqrt{\frac{4\pi}{3}} y^1_1 \left(G_4 - \left(\lambda(\lambda+1) - \lambda'(\lambda'+1) \right) G_5 + (-p'^2 + p^2) G_6 \right). \qquad (4.19)
\end{aligned}$$

Here,

$$G_\alpha = \int \psi^{(-)*}_{p_f \lambda' l' J' S'}(r)\; g_\alpha \psi^{(+)}_{p_i \lambda l J S}(r)\; r^2\, dr\,, \qquad \alpha = 1, \ldots 6 \qquad (4.20)$$

and the operators g_α are

$$\begin{aligned}
& g_1 = j_n(\frac{kr}{2}) \frac{\partial}{\partial r} \qquad g_2 = j_n(\frac{kr}{2}) \frac{1}{r} \qquad g_3 = j_n(\frac{kr}{2}) \\
& g_4 = \frac{\vec{\partial}^2}{\partial r^2} r - r \frac{\partial^2}{\partial r^2} \quad g_5 = \frac{1}{r} \qquad g_6 = r. \qquad (4.21)
\end{aligned}$$

In $(4.18 - 4.19)$ the l and l' are included subject to the Pauli principle (4.16). The matrix elements of the the charge and magnetic moment are calculated by decomposing in isospin space; for example,

$$e_1 = e(\frac{1}{2} - I^z_1). \qquad (4.22)$$

From (4.18), the spin-averaged, angle-integrated cross section can be expressed as:

$$\frac{d\sigma_{free}}{dk} = \frac{1}{8} \frac{p^2_f k^2}{(2\pi)^5 |\mathbf{v}_{12}|} \frac{dp_f}{dE} \sum |B^{\nu' S' l' m'}_{\nu\, S\, l\, m}|^2, \qquad (4.23)$$

where the orthogonality of the spherical harmonics was used. The $\frac{1}{8}$ factor is due to the isospin decomposition (Eq. 4.14), the spin average and the polarization sum, which contribute, respectively, factors of $(\frac{1}{4})$, $(\frac{1}{4})$, and (2).

The coefficients $B_{\nu\ S\ l\ m\ I}^{\nu' S' l' m' I'}$ are calculated by numerous summations over Clebsh-Jordan coefficients (from the kinematic and angular momentum factors) and a set of radial integrals, (4.20), involving the initial and final nucleon radial wavefunctions and (in some integrals) spherical Bessel functions. It is straightforward to evaluate the radial wavefunctions by solving the two-nucleon Schröedinger equation, but evaluation of the radial integrals themselves is complicated by the non-convergent, oscillatory behavior of the integrands at large radii. The integrals are evaluated by separation into two parts: from the origin to a radius R (beyond the range of the nuclear force), and from R to infinity. We integrate over the former region numerically. For the latter region, we note that outside the range of the nuclear force the radial wavefunctions are linear combinations of spherical Hankel functions. The asymptotic behavior of the Hankel functions is

$$h_l(r) \to e^{i(r-l\pi)}/r \qquad \text{as } r \to \infty, \tag{4.24}$$

so the integrals are converged by deforming the path of integration into the complex plane: $\int_R^\infty \to \int_R^{iR} + \int_{iR}^{i\infty}$. Along the imaginary r line the Hankel functions decrease exponentially, and numerical integration converges rapidly. Notice that Ref. 32 used a different method to evaluate the integrals. There the integrals were evaluated by expanding them in terms of the exponential integrals; however, the coefficients of the expansion are large and of opposite sign, and that creates numerical instabilites.

Our calculations used nucleon-nucleon wavefunctions generated by the Reid soft core potential[35] in all partial waves with total angular momentum $J \leq 4$. We verified the accuracy of our results by comparison to previous calculations of the

bremsstrahlung cross section at several energies and angles.[32,33] We then calculated angle-integrated cross sections for systematic discrete values of the initial nucleon and emitted photon energies and interpolated these with cubic bi-splines. In particular, we considered nucleon energies between 0 and 300 MeV in 15 MeV steps, and photon energies between 0 and 200 MeV in 10 MeV steps.

IV.4 Comparison with classical expressions

It is instructive to compare our formulation with classical formulas that have been used in previous studies to predict photon production cross sections. Classically, the differential probability to emit a photon during a nucleus-nucleus collision is[28]

$$\frac{d^2P}{dkd\Omega} = \frac{k}{4\pi^2}\left\langle \sum_{\epsilon} \left| \int dt \int d\mathbf{x}\ \epsilon\cdot\mathbf{J}(\mathbf{x},t)\ e^{i(kt-\mathbf{k}\cdot\mathbf{x})} \right|^2 \right\rangle , \tag{4.25}$$

where the probability is summed over the two polarizations of the photon, and the current density $\mathbf{J}(\mathbf{x},t)$ is the sum of contributions from all protons:

$$\mathbf{J}(\mathbf{x},t) = e\sum_{i=1}^{Z}\delta\left(\mathbf{x}(t)-x_i\right); \tag{4.26}$$

Z is the total number of protons in the colliding nucleus. The cross section is averaged over the ensemble of different collisions (e.g., different impact parameters). The coherent part is defined by replacing (in 4.26) the average of the square by the square of the average.

If we assume that the motion of nucleons is described by the cascade model, (i.e., the nucleons move along straight lines between collisions, and collisions occur instantaneously) then it can be easily shown[29] from (4.25, 4.26) that

$$\frac{d^2P}{dkd\Omega} = \frac{ke^2}{4\pi^2}\left\langle \sum_{\epsilon}\left|\sum_i\sum_{t_\alpha} e^{i(kt_\alpha - \mathbf{k}\cdot\mathbf{x}_\alpha)}\right.\right.$$
$$\left.\left[\frac{\mathbf{v}_i^{(+)}(t_\alpha)\cdot\epsilon}{-k+\mathbf{k}\cdot\mathbf{v}_i^{(+)}(t_\alpha)} - \frac{\mathbf{v}_i^{(-)}(t_\alpha)\cdot\epsilon}{-k+\mathbf{k}\cdot\mathbf{v}_i^{(-)}(t_\alpha)}\right]\right|^2\Bigg\rangle, \quad (4.27)$$

where the index i lables the protons in the colliding nuclei, α labels the collisions of each proton (with a neutron or another proton), and $v^{(+)}$ and $v^{(-)}$ are the velocities of the proton before and after each collision.

In the soft photon limit ($kx_\alpha \sim k\,\tau_r \ll 1$, τ_r is the total reaction time), the phase factors in (4.27) are all 1, and the photons are produced coherently.[12] In the opposite limit ($k\ \tau_{nn} \gg 1$, τ_{nn} is the average time between collisions of neighboring nucleons), the radiation is incoherent; i.e., it is a superposition of many incoherent contributions from nucleon- nucleon collisions. In the nonrelativistic limit, the cross section for emission from neutron-proton collisions has the form

$$k\frac{d\sigma_{cl}}{dk} = \int \frac{2}{3\pi}\frac{e^2}{c^3\,m^2}|\mathbf{p}_f - \mathbf{p}_i|^2\frac{d\sigma_{NP}}{d\Omega_f}\,d\Omega_f$$
$$= \int \frac{2}{3\pi}\frac{e^2}{c^3m^2}(p_f^2 + p_i^2 - 2p_fp_i\cos(\theta))\frac{d\sigma_{NP}}{d\Omega_f}d\Omega_f, \quad (4.28)$$

where $d\sigma_{NP}/d\Omega_f$ is the quantal elastic neutron-proton cross section at total center-of-mass energy E_{cm}, and θ is the center-of-mass scattering angle.† Naively, it seems possible to determine from (4.27) and (4.28) the correct balance between the coherent and incoherent components. However, for high-energy photons the expression

† Eq. (4.28) is derived from (4.27) by neglecting the $\mathbf{k}\cdot\mathbf{v}$ terms in the denominator, neglecting the interference terms in the ensemble average, replacing the ensemble average for one collision by the integral over emission angle (weighted by the cross section), and summing over polarizations.[28]

(4.27) greatly overestimates the data. It leads to total cross sections with a very slow $1/k$ decrease,[29] compared to exponentially falling data. The discrepancy occurs because it is inconsistent to apply Eq. (4.28) in the incoherent limit, due to two related reasons. The first point is that nucleon-nucleon collisions are not instantaneous, and for high photon energies the phase factor e^{ikt} varies during each collision, leading to a sharp decrease of the production probability whenever $k > \tau_c$; τ_c is a typical time of a nucleon-nucleon collision. The second point is that photons are produced in a nucleon-nucleon collision only if the collision energy excceeds the photon energy. This is a purely quantum, effect because classically the photon has no energy. The last effect can be imposed *ad hoc* in the incoherent limit by multiplying (4.28) by a theta-function that insures that the final energy of the colliding nucleons is positive

$$\frac{d\sigma_{cl}}{dk} \rightarrow \frac{d\sigma_{cl}}{dk}\,\Theta(E_{cm}-k). \tag{4.29}$$

Notice that this modification cannot be applied to the full formula (4.27), so in intermediate and high photon energies only the totally incoherent part can be calculated, even in the classical-currents approximation.

The *ad hoc* substitution (4.29) has been applied for many years in calculations of bremsstrahlung in plasmas[36] and was recently applied to the problem of heavy ion collisions.[26] We now turn to compare it to the quantum cross section we calculated, remembering again that formula (4.29) is valid only for photon energies much smaller than the total center-of-mass energy. In contrast, the method of Ref. 32 that we use is valid for photon energies smaller than the inverse range of the non-local parts in the nucleon-nucleon force:

$$k \leq R_N^{-1} \sim 300 \text{ MeV}. \tag{4.30}$$

In Fig. 7 we show our calculated angle-integrated photon-production cross

section as a function of photon energy for several different collision energies, together with the corresponding classical approximation (4.29), calculated with the same nuclear potential (Reid soft-core). The large error in the latter for hard photons is evident, and if we naively try to correct the classical formula by taking into account the reduced phase space of the outgoing nucleons for high photon energies (a factor of p_f/p_i), the error becomes even worse.

The breakdown of the classical formula can be partially understood by realizing that the outgoing nucleons have a small relative energy when the emitted photon is hard. The final wavefunction then has a very different large-distance behavior from the initial one. In particular, since the nucleon-nucleon cross section (and hence the scattering component of the wavefunction) increases with decreasing relative energy, the photon production amplitude increases as the photon becomes harder, compensating for the decrease in final nucleon phase space. Indeed, (4.29) is improved when the elastic cross section is replaced by the more symmetric expression in the initial and final momenta:

$$\frac{d\sigma_{NP}}{d\Omega} \to \sqrt{\frac{d\sigma_{NP}(E_i)}{d\Omega}\frac{d\sigma_{NP}(E_f)}{d\Omega}}. \tag{4.31}$$

However, even this replacement does not account for the large cross section at photon energies that are not very close to the kinematical limit, as can be seen from Fig. 7. It is possible that a better fitting can be obtained by a different replacement (maybe an arithmetical average is more suitable) but we have not pursued this point.

As we have already explained, another reason for the invalidity of (4.28) is the breakdown of the soft photon hypothesis at high k. The cross section for hard photons, even for weakly interacting e^+e^- collisions, does not follow the $1/k$ form unless the photon energy is very small.

IV.5 Photon emission rates

We calculate the emission spectrum for nucleons in the fluid-dynamic model, where one assigns to each space-time point a local density, temperature, and average velocity, and assumes local thermal equilibrium. The Fermi-Dirac equilibrium distribution function in the local rest frame,

$$f(\mathbf{x},\mathbf{p}) = \left(1+\exp\left((\sqrt{p^2+m^2}+\mu(\mathbf{x}))/T(\mathbf{x})\right)\right)^{-1}, \tag{4.32}$$

was used in (4.4), where the chemical potential μ is specified by the density. The resulting expression was evaluated using relativistic kinematics, the integrals were done by the Monte-Carlo method, and the results were fitted by a cubic bi-spline curve as a function of the temperature and the density. Details can be found in Appendix A. The emission rates are shown in Fig. 8 for various temperatures at $n = 0.15$ fm^{-3}. Three distinct regions are immediately clear. For low photon energies, the emitted spectrum has the $1/k$ dependence of the cross section. For very high photon energies, the spectrum decreases exponentially with k because of the Boltzman factor for the emitting nucleons, and the rate of this decrease is given by the temperature of the system. For intermediate photon energies, the Pauli blocking reduces the emission rate, and, since this reduction is less important for higher energies, it softens somewhat the exponential Boltzman decrease. The more gently falling spectrum at these energies is therefore characterized by an effective photon temperature that is higher than that of the nuclear matter. This apparent temperature is further elevated because of the increase of the elementary nucleon-nucleon bremsstrahlung cross section with energy (Fig. 7). Curves at lower densities are similar, with a characteristic n^2 dependence for high photon energies and a softer density dependence at lower energies due to Pauli blocking.

In Fig. 9 we show the ratio of the emission rate to that calculated using the

classical cross section for various densities at $T = 16$ MeV. The ratio is large, and it is clearly necessary to employ the exact cross section for a quantitative comparison of data and theory. Moreover, this ratio is energy-dependent, and thus the temperature extracted from the slope of the experimental photon spectrum has to be unfolded before an average temperature can be extracted.

For a preliminary comparison of our results with data, we followed Refs. 24 and 27 in assuming that the collision dynamics is described by the participant-spectator model. (This model is described in Chapter III). In Refs. 24 and 27 the bremsstrahlung cross section was assumed to have its classical form (4.28), so we have multiplied their results by our calculated ratio of the exact to classical emission spectrum, calculated at the fireball temperature. Multiplication of the total spectrum, instead of the differential spectrum at each density, is justified since the ratio is not very sensitive to the density (Fig. 9). As shown in Fig. 10, for the few experimentally measured systems[23,24,27] the modification brings the theory into good agreement with the data, without invoking any coherent production mechanism.[24] However, note that the calculations of Ref. 24 have been normalized to fit the data, so no conclusive evidence can be drawn from these comparisons. The agreement of the spectral shape, is, nevertheless, an indication that incoherent emission is the right production mechanism.

IV.6 Results of VUU simulations

We used the VUU code of Aichelin and Bertch, as described in detail in Ref. 18 . The reader should note that the approach of this code is different from that outlined in Chapter III. The average one-body distribution, f, is determined by

averaging over an ensemble of concurrent nucleus-nucleus collisions (Fig. 11). Individual nucleus-nucleus collisions are modeled as in the Cascade, except that nucleon-nucleon collisions can be Pauli-blocked, and between collisions the nucleons move in the Potential $V(f)$. Notice that to incorporate the separation assumption about the two-body density

$$f(1,2) = f(1)f(2), \tag{4.33}$$

we would also have to include collisions between nucleons in different ensembles; however, this would increase considerably the numerical effort. As the ultimate justification of the VUU is phenomenological, the ensemble approach should not be regarded as worse than a full-collisions approach, as long as its results are compatible with experiment.

Photon production is easily incorporated into the VUU code. We let the ensemble evolve in time, and whenever a neutron and a proton get to within a collision distance in one of the colliding systems, we calculate the probability of emitting a photon

$$\frac{1}{\sigma_{NP}} \frac{d\sigma_{free}}{dk}, \tag{4.34}$$

where σ_{NP} is the neutron-proton elastic collision cross section. The total emission cross section is the sum of the probabilities over all collisions, with Doppler shifts and Pauli-blocking factors included. The result is integrated over impact parameter and then averaged over the ensemble

$$\frac{d\sigma_\gamma}{dk d\Omega} = \int 2\pi b\, db \frac{1}{N_e} \sum \frac{1}{\sigma_{NP}} \frac{k}{k_d} \frac{1}{4\pi} \frac{d\sigma_{free}}{dk} (1 - f(\mathbf{p}_{1f}))(1 - f(\mathbf{p}_{2f})), \tag{4.35}$$

where N_e is the ensemble size, and the sum extends over all neutron-proton collisions. The factor of 8 in Eq. (4.4) disappears, because the neutron and the proton can be in two spin states and have different isospins (i.e., they are different particles). Notice that the probability (4.34) is included regardless of whether the *elastic*

neutron-proton collision is Pauli-blocked. Since in this procedure the emission does not modify the collision dynamics, we cannot apply it for pion emission, where the back-reaction of the pion field changes the dynamics (at least above thereshold, when large numbers of pions are produced).

As explained in Sections IV.2, IV.3, we did not calculate the angular dependence of $d\sigma_{free}/\, d\Omega\, dk$, but averaged over the photon solid angle. A full calculation including angular dependency is beyond our numerical and data-storing capabilities. Instead, we adopted the dipole emission approximation

$$\frac{d\sigma_{free}}{dk d\Omega} = \frac{1}{4\pi}\frac{d\sigma_{free}}{dk}\,\frac{3}{2}\sin^2(\theta_\gamma), \tag{4.36}$$

where θ_γ is the angle of photon emission, and all quantities are calculated in the center of mass of the colliding nucleons. The phenomenological cross sections used in Ref. 37 also have an approximate dipole emission pattern, and this pattern is characteristic of the soft photon approximation.[28,37]†

We ran the VUU code for C+C collisions at two energies, 40 and 84 MeV/A. Data are available for these systems,[23,24] and they were also simulated in the VUU framework, with a phenomenological expression for the elementary photon emission cross section, fitted to data from proton-nucleus collisions.[37] In Fig. 12 we show the differential emission cross section for $\theta_\gamma = 90^o$ (in the center of mass of the C+C system), and compare it to available data and simulations. For the 84 MeV/A reaction we overestimate the data by a factor 2, and for the 40 MeV/A reaction, by a factor of 5. Our results are higher than the results of Ref. 37 by a factor of ~ 3. This is consistent with our large elementary cross sections. As long as the

† Ref. 37 includes an additional monopole term of relative strength p_f^2/p_i^2; however, most hard photons are produced near the kinematical limit, where this term will be negligible.

discrepancies between different experiments are not settled, we cannot draw definite conclusions from our results; however, once definitive data become available, we can estimate the reduction of the $P + N \rightarrow P + N + \gamma$ cross section from its free space value, by scaling the results to fit the data. We can then estimate the elastic nucleon-nucleon cross section, if we assume that it scales like the photon production cross section. Naively, this procedure seems to be complicated by the explicit presence of σ_{NP} in Eqs. (4.34,4.35); however, this factor is compensated by the summation over collisions, because the number of collisions is proportional to σ_{NP}. The dependence on σ_{NP} enters mainly through its influence on the nucleons phase-space distribution. At the relatively low collision energies we used, the pressure term from the equation of state is small, so the results are not influenced by the equation of state that is used. We also checked this fact explicitly.

Notice that photon emission can be used to extract σ_{NP} only if it turns out that the VUU always overpredicts the data; it is very hard to imagine that the effective cross section in the medium is enhanced over its free space value.

The angular dependency of the total emission spectra is shown in Fig. 13. The dipole peak is retained, and this indicates that the initial collisions of the nucleons (that move along the nucleus-nucleus collision axis) are responsible for a large portion of the emission spectra; however, subsequent collisions also create a significant cross section for photons that are parallel to the collision axis. Due to Doppler shifting, the spectra are asymmetric for hard photons.

The time evolution of the emission spectra for zero impact parameter collisions is shown in Fig. 14. (The figure shows the evolution for 40 and 100 MeV/A collisions; the latter energy was used instead of 84 MeV/A, but the evolution is similar in both cases.) The code starts the evolution at a time when the nuclei are

two Fermi apart. Due to approximations inherent in the VUU code, a small fraction of the spectrum is emitted before the nuclei first touch, by unblocked collisions inside the nuclei; but these collisions are soft and affect only the soft-photon spectra, as shown in the figure. Once the nuclei collide, the spectrum quickly reaches its asymptotic value; for example, in the 40 MeV/A collision, 80% of the 100 MeV photon spectra is emitted after 9 fm/c $\sim 0.25\tau_C$, where

$$\tau_C = \frac{4R_C}{v_C} \tag{4.37}$$

is the time it would take for the nuclei to pass through each other if they were transparent (see footnote on p. 8). This suggests that the hard photons are emitted in the first collisions of the nucleons, before full equilibrium is achieved. Photons probe the equilibrium stage only for large systems. (The number of first collisions is proportional to the number of nucleons on the surface of the nuclei, so it scales as $A^{2/3}$; the number of collisions in the equilibrium stage scales as A^2, so even though collisions in the later stage are less energetic, they will dominate for very large A).

In conclusion, we find that our spectra differ from previous estimates based on a classical soft-photon approximation, lead to good agreement with the shape of the data, and conceivably can be used to extract the effective nucleon-nucleon cross section in heavy ion reactions.

V. PHOTON INTERFEROMETRY FOR HEAVY ION COLLISIONS

V.1 Introduction

In 1930 Dirac wrote:[38] "Interference between different photons never occurs." It took 28 years till Hanbury, Brown, and Twiss demonstrated that Dirac was wrong. Identical particle interferometry is possible, and even useful. Initially this method was used to measure stellar radii, and it was soon extended to particle physics and heavy ion reactions, where it is used to extract source sizes and lifetimes in reactions.

The first experimental measurements of correlations in heavy ion reactions were done by the Riverside group that measured proton correlations.[39,40] Since then this method has been extended to pions and light fragments,[14,40] and in view of recent measurements of inclusive photon spectra, it is natural to ask whether interferometry might be applied to these later particles as well. Measuring the interference of high-energy photons might be difficult experimentally because of the low photon production rates and high $\pi^0 \rightarrow 2\gamma$ background. However, the experimental effort may be well justified, since photons do not suffer from the reabsorption and final-state interactions that distort the spectra of strongly interacting particles, and therefore photon interferometry may be a more direct probe on the structure and lifetime of the central density region.

To use photon interferometry to probe nuclear collisions dynamics we first have to understand the dependence of the $\gamma\gamma$ correlation function on the emitting source size and lifetime. In this chapter, we examine the $\gamma\gamma$ correlations expected under

certain plausible assumptions about the form of the electromagnetic current. Our formulation follows the treatment of pion correlations in Ref. 41, but with variations due to the vector nature of the photons and their zero mass.

We first give a heuristic derivation of two-particle correlations before proceeding with a formal calculation. For simplicity, only scalars are considered. We assume that the identical scalars 1,2 with four-momenta k_1,k_2 are emitted from the space-time points r_1,r_2 and detected at the points x_1,x_2. Because the particles are identical, the amplitude for detection at x_1, x_2 is summed with the amplitude for detection at x_2, x_1 (Fig. 15). The differential emission distribution is then

$$dP_2 = P_1(k_1)\, P_1(k_2)\, \rho(r_1)\, \rho(r_2)\, d^4r_1 d^4r_2 \left| \frac{1}{\sqrt{2}} \left(e^{ik_1(x_1-r_1)} e^{ik_2(x_2-r_2)} + e^{ik_1(x_2-r_1)} e^{ik_2(x_1-r_2)} \right) \right|^2, \quad (5.1)$$

where P_1 is the one-particle inclusive distribution and $\rho(r)$ is the normalized source distribution function (and here we assume that the shape of the emission spectra at each point is independent of the particle four-momenta). The total emission probability is the integral of (5.1), and it can be expressed compactly by

$$F_2 = 1 + |\tilde{\rho}(k_1 - k_2)|^2, \quad (5.2)$$

where $\tilde{\rho}$ is the Fourier-transformed density and the correlation function, F_2, is defined by

$$F_2(k_1, k_2) = \frac{P_2(k_1, k_2)}{P_1(k_1) P_1(k_2)}. \quad (5.3)$$

The correlation function varies from a maximum of 2 when $k_1 = k_2$, to 1 when the difference in the momenta is large. The width of the maximum is $\sim R^{-1}$; R is a typical radius of the emitting region.

V.2 Photon interferometry from colliding source

The heuristic derivation is not capable of describing coherent current effects, which may be of some importance in photon correlations. We therefore turn now to a more formal derivation of photon correlations.

Denoting the amplitude to produce a photon with wave vector $\mathbf{k}$ and polarization ϵ by $M_{\epsilon k}$, the m-photon inclusive distribution is[41] ($\hbar = c = 1$)

$$P(\mathbf{k}_1 ... \mathbf{k}_m) \equiv C_m \frac{1}{\sigma_\gamma} \frac{d^{3m}\sigma_\gamma}{d\mathbf{k}_1 \ldots d\mathbf{k}_m} = \sum_\epsilon \langle |M_{\epsilon_1\, k_1}|^2 ... |M_{\epsilon_m\, k_m}|^2 \rangle, \tag{5.4}$$

where the cross section is averaged over the ensemble of different collisions and summed over photon polarizations. C_m are normalization constants. The two-photon correlation function is defined as

$$F(\mathbf{k}, \mathbf{k}') \equiv \frac{P(\mathbf{k}, \mathbf{k}')}{P(\mathbf{k}) P(\mathbf{k}')}. \tag{5.5}$$

In the classical approximation, the photon production amplitude is

$$M_{\epsilon,k} = \epsilon \cdot \mathbf{J}(\mathbf{k}), \tag{5.6}$$

where $\mathbf{J}(\mathbf{k})$ is the Fourier transform of the electromagnetic current $\mathbf{J}(\mathbf{x},t)$ (see Eq. 4.25).

In a cascade picture, the current can be represented as a sum of contributions from individual nucleon-nucleon collisions,

$$\mathbf{J}(\mathbf{x}, t) = \sum_\alpha \mathbf{j}_\alpha (\mathbf{x} - \mathbf{x}_\alpha, t - t_\alpha),$$

and therefore,

$$\mathbf{J}(\mathbf{k}) = \sum_\alpha \mathbf{j}_\alpha(\mathbf{k}) e^{ik \cdot x_\alpha}, \tag{5.7}$$

where l is a collision-labeling index and x_α is the space-time location of the l-th collision.

Let us first neglect the coherent electromagnetic current due to the collective deceleration of the two nuclei. In this approximation of an incoherent current,

$$\langle \mathbf{j}_\alpha(\mathbf{k}) \rangle = 0. \tag{5.8}$$

We now make two further approximations: (i) all collisions are assumed to produce the same magnitude of electromagnetic current;[41] (ii) due to the approximate isotropy of the nuclear force, currents from different collisions are assumed to have uncorrelated directions

$$\langle \mathbf{j}_\alpha \cdot \mathbf{j}_{\alpha'} \rangle = 0, \qquad \text{if} \quad \alpha \neq \alpha'.$$

The first assumption is somewhat crude because collisions in the central, high-temperature region of the colliding nuclei are likely to create more electromagnetic current than peripheral collisions. We will return to this point below. With regard to the second assumption, note that in the dipole approximation the current from proton-proton and neutron-neutron collisions vanishes. These collisions, which do not produce electromagnetic current, will reduce the correlations between consecutive photon-producing neutron-proton collisions.

With these two simplifying approximations, the electromagnetic current has the form:

$$\mathbf{J}(\mathbf{k}) = j(k) \sum \hat{\mathbf{v}}_\alpha e^{i\mathbf{k}\cdot\mathbf{x}_\alpha}, \tag{5.9}$$

where now $j(k)$ depends only on the photon energy (not on its direction) and $\hat{\mathbf{v}}_\alpha$ is a random unit vector. Using Eqs. (5.3-5.9) and the definition of ensemble average,

$$\langle e^{ikx} \rangle = \int e^{ikx} \rho(x)\, d^4x = \rho(k), \tag{5.10}$$

where $\rho(x)$ is the normalized space-time density of collisions, we can readily calculate the one-photon and two-photon inclusive distributions:

$$P(\mathbf{k}) = \frac{2N}{3} |j(k)|^2,$$

$$P(\mathbf{k},\mathbf{k}') = P(\mathbf{k})\,P(\mathbf{k}')\left(1+\frac{1+(\hat{\mathbf{k}}\cdot\hat{\mathbf{k}}')^2}{2}\,\frac{|\rho(k+k')|^2+|\rho(k-k')|^2}{2}\right), \qquad (5.11)$$

where N is the number of the current-producing collisions, and we have used the simple identities:

$$\langle \epsilon\cdot\hat{\mathbf{v}}_\alpha\,\epsilon'\cdot\hat{\mathbf{v}}_{\alpha'}\rangle = \frac{\epsilon\cdot\epsilon'}{3}\,\delta_{\alpha\alpha'}\ , \qquad (5.12)$$

and

$$\sum_{\epsilon\,\epsilon'}(\epsilon\cdot\epsilon')^2 = 1+(\hat{\mathbf{k}}\cdot\hat{\mathbf{k}}')^{\mathbf{2}}. \qquad (5.13)$$

The correlation of parallel photons with equal energy is thus

$$F(\mathbf{k},\mathbf{k}) = \frac{3}{2}+\frac{|\rho(2k)|^2}{2}, \qquad (5.14)$$

and for high photon energies, ($\geq$ 40 MeV) $|\rho(2k)| \ll 1$ so

$$F(\mathbf{k},\mathbf{k}) \to \frac{3}{2}.$$

The limiting value of 3/2 differs from the limiting value for scalar emission, 2, due to the polarization average.

Notice that the equation analogous to (5.14) for massless scalar emission is valid only in the high-energy limit:

$$k > \tau^{-1}, \qquad (5.15)$$

where τ is the lifetime of the emitting region. The reason for the difference is that for scalars the incoherence is due to the vanishing of the relative phase factor:

$$\langle e^{ik(x_\alpha - x_{\alpha'})}\rangle = |\rho(k)|^2 \ll 1. \qquad (5.16)$$

Photons will also be incoherent at wavelengths where (5.16) is not satisfied due to the vanishing of the current direction average, which is unrelated to the photon

energy. Of course, at very low photon energies the correlation function is modified by the coherent current due to the motion of the nuclei, which was neglected in our formulae. However, this current is negligible for photon energies higher than the inverse of the nuclear radii,

$$k > {R_N}^{-1}. \tag{5.17}$$

For high-energy heavy ion collisions, the lifetime and radius of the fireball are comparable, $R \sim \tau$. Since the radius of the particle-emitting region, R, may be much smaller than the radius of the colliding nuclei R_N, it follows from Eqs. (5.15,5.17) that intermediate-energy photons ($R_N^{-1} < k < \tau^{-1}$) are produced incoherently, while a massless scalar particle with the same energy would have been produced coherently.

To obtain numerical estimates of the photon correlation function, we model the space-time collision density for heavy ion collisions as a spherically symmetric Gaussian shaped fireball[42 43]:

$$\rho(\mathbf{x},t) = \frac{1}{4\pi^2 R^3 \tau} \exp(-\frac{x^2}{2R^2} - \frac{t^2}{2\tau^2}), \tag{5.18}$$

where R and τ characterize the fireball radius and lifetime, respectively, and may depend on the collision energy. One can probably assume

$$R \sim v\tau, \tag{5.19}$$

where v is a typical velocity of the nucleons. For an intermediate energy heavy ion collision, the fireball model predicts

$$v = \sqrt{T/m}, \tag{5.20}$$

where m is the nucleon mass and T is an average participant temperature, while for high-energy heavy ion collisions, $v = 1$. As previously mentioned, collisions of peripheral nucleons are less violent and create less current than collisions in the center

of the fireball. The radius extracted from a comparison of (5.18) with experiment is a collision-strength-weighted radius and therefore will likely underestimate the radius of the photon emitting region.

In Fig. 16 we plot the correlation function for parallel photons as a function of their energy, and in Fig. 17, that for equal energy photons as a function of their opening angle. The curves are shown for various source radii and lifetimes. Notice that for low photon energies the decrease of the correlation function with increasing relative angle is due solely to the polarization average term, (5.11), not to a decrease of the Fourier-transformed density, $|\rho(k-k')|$. To check whether a measured variation of the correlation function is related to $|\rho(k-k')|$, one should measure the correlation function for antiparallel photons. However, photons from pion decay greatly complicate this measurement.[44] In principle, one could also distinguish the two factors by checking the value of the correlation function at its minimum. If the energy of the photons is low enough so that $|\rho(k-k')|$ is approximately constant, the polarization average will decreases the correlation function to a minimum value that is greater than 1.25 (for perpendicular photons), while at high energies the $|\rho(k-k')|$ term will reduce the minimum correlation function to 1. However, this method may not be feasible due to experimental difficulties in extracting the absolute normalization of the correlation function.[44]

At low and intermediate photon energies ($\leq$ 60 MeV) Eqs. (5.11,5.14) for the photon distribution functions will be modified by the coherent current caused by the collective deacceleration of the two nuclei. For colliding nuclei with equal charge and mass, the coherent current in the long wavelength limit has the form

$$\mathbf{J}_c(\mathbf{k}) = i\ j_c(k)(\hat{\mathbf{k}}\cdot\hat{\mathbf{z}}\,)\ \hat{\mathbf{z}}, \tag{5.21}$$

where the subscript c stands for "coherent"and $\hat{\mathbf{z}}$ is a unit vector along the collision

axis. The scalar function $j_c(k)$ depends on the details of the collision, and in particular on the deacceleration time. The current is imaginary in Fourier space because the real-space current is antisymmetric under reflection. Adding both coherent and incoherent currents, the one and two photon distribution functions can be shown to be:

$$P(\mathbf{k}) = P_\gamma(k) + P_c(\mathbf{k}) \tag{5.22a}$$

$$\begin{aligned} P(\mathbf{k},\mathbf{k}') = {} & P(\mathbf{k})P(\mathbf{k}') \\ & + P_\gamma(k)P_\gamma(k')\frac{1+(\hat{\mathbf{k}}\cdot\hat{\mathbf{k}}')^2}{2}\,\frac{|\rho(k+k')|^2+|\rho(k-k')|^2}{2} \\ & + B\,N\Big(-j_c(k)\,j_c(k')\,j_\gamma^*(k)\,j_\gamma^*(k')\,\rho^*(k+k') \\ & \quad + j_c(k)\,j_c^*(k')\,j_\gamma^*(k)\,j_\gamma(k')\,\rho^*(k-k') + C.C.\Big), \end{aligned} \tag{5.22b}$$

where :

$$P_c(\mathbf{k}) = (\hat{\mathbf{k}}\cdot\hat{\mathbf{z}})^2(1-(\hat{\mathbf{k}}\cdot\hat{\mathbf{z}})^2)\,|j_c(k)|^2, \tag{5.23}$$

and

$$B \equiv \frac{\hat{\mathbf{k}}\cdot\hat{\mathbf{z}}\;\hat{\mathbf{k}}'\cdot\hat{\mathbf{z}}}{3}\Big(1-(\hat{\mathbf{k}}\cdot\hat{\mathbf{z}})^2-(\hat{\mathbf{k}}'\cdot\hat{\mathbf{z}})^2+(\hat{\mathbf{k}}'\cdot\hat{\mathbf{k}})(\hat{\mathbf{k}}\cdot\hat{\mathbf{z}})(\hat{\mathbf{k}}'\cdot\hat{\mathbf{z}})\Big). \tag{5.24}$$

The index γ refers to the expressions obtained in the presence of the noncoherent current alone, Eq. (5.11). From (5.22) we can calculate the correlation function for identical photons, and, in the limit of high energy, $|\rho(2k)| \ll 1$, find

$$F(\mathbf{k},\mathbf{k}) = \frac{3}{2} - \frac{1}{2}\frac{P_c(\mathbf{k})}{P(\mathbf{k})}. \tag{5.25}$$

However, notice that this equation is valid only for hard photons, for which it is natural to expect that the coherent current vanishes. Thus (5.25) cannot be used to extract the coherent current from the experimental two-photon correlation function,

and, in any case, it is obviously easier to extract it from the angular distribution of the one-photon distribution, Eq. (5.22a). However, the coherent current has to be included in (5.22) because its presence affects the shape of the distribution function and thus the extracted source size. Fig. 18 shows the effect of a large coherent current on the correlation function.

In conclusion, we find that both the polarization average and a possible coherent component complicate the extraction of the size and lifetime of the emitting source from the correlation function.

APPENDIX A. MONTE- CARLO EVALUATION OF THE MOMENTUM INTEGRALS

From Eqs. (4.4, 4.5, 4.6, 4.7), the local emission rate of photons from nuclear matter in equilibrium is

$$\frac{d^7N}{d^4x\,dk\,d\Omega} = \frac{8}{4\pi}\int \frac{p_{1\,i}^2\,d\Omega_{1\,i}}{(2\pi)^3}\frac{p_{2\,i}^2\,d\Omega_{2\,i}}{(2\pi)^3}\frac{d\Omega_f}{4\pi}\,f(\mathbf{p}_{1i})\,f(\mathbf{p}_{2i})\,(1-f(\mathbf{p}_{1i}))\,(1-f(\mathbf{p}_{2i}))$$
$$|\mathbf{v}_{12i}|\frac{k}{k_d}\frac{d\sigma_{free}(E_{cm})}{dk_d}\Theta(E_{cm}-k_d), \qquad (A.1)$$

where we use the notation of Chapter IV, and the theta function is explicitly included to recall that the elementary cross section vanishes when the photon energy exceeds the collision energy.

The 8-dimensional integral is evaluated by the Monte-Carlo method, the only known practical method for evaluating multidimensional integrals (beyond 5 or 6 dimensions). Here we will only outline this method. For a more pedagogical exposition of this method, we refer the reader to Ref. 45.

Consider an M-dimensional integral $\int d^M\mathbf{x}\,f(\mathbf{x})$; $\mathbf{x}$ is an M-dimensional vector. Let us, for simplicity, constrain the range of integration to the M-dimensional unit cube, so the integral is also the average of f. We know from probability theory that, when we pick a series of N random vectors, the average of f over this series is an approximation of the average over the range, with the error proportional to $1/\sqrt{N}$

$$\frac{1}{N}\sum_{\alpha=1}^{N} f(\mathbf{x}_\alpha) \sim \int d^M\mathbf{x}\,f(\mathbf{x}) \pm \frac{\sigma_f}{\sqrt{N}}. \qquad (A.2)$$

Notice that the error is independent of the dimension of the domain and depends only on the fluctuation of the function over the range, σ_f. (The more uniform a

function is, the faster the approximation will converge.) The fluctuation can be estimated from

$$\sigma_{fN}^2 \equiv \frac{1}{N}\sum_{\alpha=1}^{N} f(\mathbf{x}_\alpha)^2 - \left(\frac{1}{N}\sum_{\alpha=1}^{N} f(\mathbf{x}_\alpha)\right)^2 = \sigma_f^2 + O\left(\frac{1}{N}\right). \qquad (A.3)$$

To use formula $(A.2)$, we need to convert the 8 variables to a new set of variables that lie in the range $[0,1]$. The angular variables are easily transformed:

$$d\Omega = \sin(\theta)\; d\theta\, d\phi = 4\pi\; d\left(\frac{1-\cos(\theta)}{2}\right)\; d\left(\frac{\phi}{2\pi}\right). \qquad (A.4)$$

For the momentum variables, p_1, p_2; that lie in the range $[0,\infty)$, we need to use a monotonic integration variable

$$dp = \frac{dp}{d\omega}\, d\omega, \quad 0 \le \omega \le 1. \qquad (A.5)$$

To choose an appropriate integration variable, we need to estimate the values of p_1, p_2, where the integrand will be peaked. Physically, it is reasonable to assume that the largest contribution to the production will come from nucleons that have just enough energy to create a photon and still remain outside the Fermi-sea; i.e.,

$$E_{1\,peak} = E_{2\,peak} \sim \mu + \frac{k}{2}. \qquad (A.6)$$

The width of the optimal weight function is related to the temperature; we estimated that it is $\sim \sqrt{2mT}$. Therefore, the variable we chose is:

$$\omega(p) = e^{-\alpha|p-p_{peak}|/\sqrt{2mT}}, \qquad (A.7)$$

where $p_{peak} = \sqrt{E_{peak}^2 - m^2}$, and α is a parameter that is chosen empirically. Good convergence was found with $\alpha \sim 0.3$. This weight function is not monotonic, but this only introduces a minor technical complication.

For all values of k, μ, T that were used, the integral converged to better than 1% with less than 100,000 points. Since the integral converged fast enough with the crude weight function $(A.7)$, we did not seek a better weight function that will increase the rate of convergence.

References

(1) R. Stock, Phys. Rep. **135** (1986) 261.

(2) R. B. Clare and D. Strottman, Phys. Rep. **141** (1986) 177.

(3) S. E. Woosley, in *Explosive Nucleosynthesis*, eds. Schramm and Arnett (University of Texas press, Austin, 1973) p. 82.

(4) P. J. Siemens, to be published in the proceedings of the Workshop on the Nuclear Matter Equation of State, Berkeley, 1986.

(5) H. Stocker and W. Greiner, Phys. Rep. **137** (1986) 277.

(6) J. Cleymans, R. V. Gavani, and E. Suhonen, Phys. Rep. **130** (1986) 217.

(7) Proceedings of the Workshop on the Nuclear Matter Equation of State, Berkeley, 1986, to be published.

(8) P. J. Siemens and J. I. Kapusta, Phys. Rev. Lett. **43** (1979) 1486.

(9) H. Stocker, to be published in the proceedings of the Workshop on the Nuclear Matter Equation of State, Berkeley, 1986.

(10) J. Aichelin, to be published in the proceedings of the Workshop on the Nuclear Matter Equation of State, Berkeley, 1986.

(11) J. Aichelin and C. M. Ko, Phys. Rev. Lett. **55** (1986) 2661.

(12) D. Vasak, W. Greiner, B. Müller, Th. Sthal and M. Uhlig, Nucl. Phys. **A428** (1984) 291.

(13) R. Stock, to be published in the proceedings of the Workshop on the Nuclear Matter Equation of State, Berkeley, 1986.

(14) C. K. Gelbke, published in the proceedings of the Workshop on Intermediate Energy Nuclear Physics, Oak Ridge, 1985.

(15) R. Hanbury-Brown and R.Q. Twiss, Nature, **177** (1956) 27.

(16) S. E. Koonin, Ph. D. Thesis, M.I.T., 1975.

(17) Y. Yariv and Z. Fraenkel, Phys. Rev. **C20** (1979) 2227.

(18) J. Aichelin and G. Bertsch, Phys. Rev. **C31** (1985) 1730.

(19) S. E. Koonin and J. Randrup, to be published in proceedings of Fourth Winter Workshop on Nuclear Dynamics, Cooper Mountain, 1986.

(20) P. Carruthers and F. Zacharisen, Rev. Mod. Phys. **55** (1983) 245.

(21) M. L. Goldberger, Phys. Rev. **74** (1948) 1269.

(22) H. Mancher, Phys. Rep. **127** (1985) 309.

(23) E. Grosse, Bormio Meeting, 1984, and E. Grosse *et. al.*, Europhys. Lett. **2** (1986) 9.

(24) J. Stevenson *et. al.*, National Superconducting Cyclotron Laboratory preprint (1986).

(25) N. Alamanos *et. al.*, Phys. Lett. **173B** (1986) 392.

(26) H. Nifencker *et. al.*, proceedings of the XIV international winter meeting on Nuclear Physics, Bormio, 1986.

(27) H. Nifenecker and J.P. Bondorf, Nucl. Phys. **A442** (1985) 478.

(28) J. D. Jackson, *Classical Electrodynamics* (Wiley, New York, 1975) p. 671 and p. 706.

(29) C. M. Ko, G. Bertsch and J. Aichelin, Phys. Rev. **C31** (1985) 2324.

(30) R. Shaym and J. Knoll, Nucl. Phys. **A448** (1986) 332.

(31) P. Signel, in *Advances in Nuclear Physics*, eds. M. Baranger and E. Vogt (Plenum, New York, 1969) pp. 257-283.

(32) V. R. Brown and J. Franklin, Phys. Rev. **C8** (1973) 1706, and V. R. Brown, Phys. Rev. **177** (1969) 1498.

(33) G. E. Bohannon, Phys. Rev. **C17** (1978) 865, and G. E. Bohannon, L. Heller, and R. H. Thompson, Phys. Rev. **C16** (1977) 284.

(34) A. Messiah, *Quantum Mechanics* (Wiley, New York, 1976) p. 822.

(35) R. V. Reid, Ann. Phys. (N.Y.) **50** (1968) 411, and B. D. Day, Phys. Rev. **C**24 (1981) 1203.

(36) G. B. Rybicki and A. P. Lightman, *Raidative Processes in Astrophysics* (Wiley, New York 1979) p. 156.

(37) W. Bauser, G. Bertsch, W. Cassing, and U. Mosel, Michigan State University preprint, 1986, and T. Biro, U. Mosel, M. Tohyama, and W. Bauer, Michigan State University preprint, 1986.

(38) P. A. M. Dirac, *The Principles of Quantum Mechanics* (Clarendon, 1967) revised fourth edition, p. 9. Notice that Dirac has not erased this phrase in the revised edition, even though it appeared eleven years after the work of Hanbury-Brown and Twiss.

(39) S. Y. Fung *et. al.*, Phys. Rev. Lett. **141** (1978) 1592, and D. Beavis *et. al.*, Phys. Rev. **C27** (1983) 910.

(40) W. Zajc *et. al.*, Phys. Rev. **C29** (1984) 2173.

(41) M. Gyulassy, S. K. Kauffmann, and Lance W. Wilson, Phys. Rev. **C20** (1979) 2267.

(42) F. B. Yano and S. E. Koonin, Phys. Lett. **78B** (1977) 556.

(43) S. E. Koonin, Phys. Lett. **70B** (1977) 43.

(44) K. Wolf, private communication.

(45) S. E. Koonin, *Computational Physics* (Benjamin/Cummings, Menlo Park, California, 1986) p. 185.

(47) National research council, *Physics through the 1990s,* vol. 6, *Nuclear Physics* (National Academy Press, Washington D.C., 1986) p. 91.

PART 2

STRUCTURE OF MATTER IN STRONG MAGNETIC FIELDS

INTRODUCTION

Atomic structure in very strong magnetic fields ($B = 10^{12} - 10^{13}$G) is of relevance to neutron star studies.[1,2,3,4] Of particular importance is the question of whether the surface matter is solid or is a gas of isolated atoms. For example, if the cohesive energy of the solid is ≤ 3 keV per atom, the surface matter will not support a finite electric-field boundary condition.[5] Models of surface heating by impact of solid matter also depend on whether material will solidify in strong magnetic fields.[6]

In this part of the thesis we present variational Hartree-Fock calculations for matter in strong magnetic fields. We calculate the energy of both isolated atoms and linear chains. The physical justification for the single chain assumption is that perpendicular to the field, electrons are constrained to stay in the Landau orbitals; their orbitals will not be modified by the Coulomb field, so Pauli repulsion is going to keep them apart.

Our calculations are the first self-consistent ones treating exchange properly for atoms heavier than helium [7] in high fields and are therefore particularly important for neutron star surfaces, where the dominant material is believed to be iron. Previous studies of this problem include restricted variational[8] and density-functional calculations;[9,10] the isolated atom case was also studied using the Thomas-Fermi-Dirac method.[11] However, a more exact treatment is needed to obtain quantitative results, because the errors introduced by these methods are of the same order as

the cohesive energy (a few percent of the total energy). The lack of correlations in the Slater determinant we assume probably underestimates the absolute binding energies by less than 1% (Chapter III). Moreover, since we are interested in the energy difference between the isolated atom and the solid, the deficiences of the Hartree-Fock method partially cancel.

We find that for elements with atomic number $Z > 2$ at $B_{12} = 1$ (and $Z > 4$ at $B_{12} = 5$) the isolated atom is energetically favored over the molecular chain (here, and in the following, we use the convention $B_12 = B/10^{12}G$). The physical reason for this is that in strong fields all electron spins are directed along the field; by the Pauli principle, the spatial wavefunction is totally antisymmetric. Therefore, the zero-field bonding mechanism, where two atoms bind together in a spin-singlet spatially symmetric state, will not be effective in strong fields.

This part is organized as follows: In Chapter I we discuss qualitatively the atomic structure in strong fields and introduce relevant parameters. In Chapter II we justify our ansatz for the isolated-atom wavefunction: the Hartree-Fock wavefunction in the adiabatic approximation. From this wavefunction, we derive the one-dimensional Hartree-Fock equations in Chapter III, and explain their solution. In Chapter IV we explain the chain approximation for three-dimensional matter and discuss different choices for the Bloch wavefunctions. Chapter V is analogous to Chapter III: we derive the Hartree-Fock equations for one-dimensional chains. The extension to infinite chains introduces complications, some of which are dealt with by the standard method of Fourier transform; others require analytical manipulations. Numerical results are presented in Chapter VI, along with comparisons

with previous calculations.

For the convenience of the reader, we separated the presentation of all approximations that require physical justification (Chapters I, II, and IV) from the presentation of the solutions of equations (Chapters III and V).

I. BASIC CONCEPTS

The Hamiltonian of a neutral atom in a uniform magnetic field is

$$\begin{aligned} H =& H_B + V_{en} + V_{ee} \\ =& \sum_i \frac{1}{2M}\left(\mathbf{p}_i + \frac{e}{c}\mathbf{A}_i\right)^2 + \sum_i \frac{e}{mc}\mathbf{B}\cdot\mathbf{S_i} - Ze^2\sum_i \frac{1}{r_i} + e^2\sum_{i<j}\frac{1}{r_{ij}}, \end{aligned} \quad (1.1)$$

where the index i labels the electrons, Z is the atomic charge, and $\mathbf{p}, \mathbf{r}, \mathbf{S}$, are the momentum, position, and spin, respectively. M and $-e$ are the electron's mass and charge (we include the negation sign in order to have $e > 0$). $\mathbf{A}$ is the electromagnetic potential of a constant magnetic field,

$$\mathbf{A} = \frac{1}{2}\mathbf{B}\times\mathbf{r}. \quad (1.2)$$

We adopted the Born-Oppenheimer approximation, i.e., neglected the motion of the nucleus.[12] The errors in this approximation are of the order of the electron-nucleus mass ratio and are too small to affect our calculations of the cohesive energy. However, since the binding energies are very large in strong fields (see below), the energy splittings that the motion of the nucleus induces are much higher than in the zero field case. The splittings may reach few eV and they modify the opacities at these frequencies; this, in turn, strongly changes the radiation spectra, as the temperature in neutron stars surfaces is expected to be in the 1-100 eV range.[3]

In this chapter, our discussion is qualitative; we therefore neglect the electron-electron repulsion, which is, in fact, dominated by the nucleus-electron attraction.

(The repulsion is included later, but only via the mean field it creates; see Chapter II.) The wavefunction is thus a Slater determinant of single-electron orbitals.

The orbitals' structure is dictated by the relative strength of the magnetic and Coulomb interactions. When the magnetic field vanishes, the potential is spherical. As we show below, we are interested in the opposite extreme, strong magnetic fields perturbed slightly by Coulomb interaction.

To study the strong field limit, we first neglect the Coulomb interaction. The electron then moves under the sole influence of the magnetic field. Before proceeding to the formal solution of this problem, we present a semiclassical derivation. The classical force balance equation reads

$$\frac{eBv_\phi}{c} \sim M\omega^2\rho, \tag{1.3}$$

and since

$$v_\phi = \omega\rho, \tag{1.4}$$

it follows that

$$\omega \sim \frac{eB}{Mc}\ . \tag{1.5}$$

Here we introduced the usual cylindrical coordinates (ρ, ϕ, z). v_ϕ, w, and L_z denote, respectively, the electron's velocity perpendicular to B, the cyclotron frequency and the z component of the angular momentum. From the Bohr-Sommerfeld quantization rule

$$L_z = M\omega\rho^2 \sim m\hbar, \qquad m = 0, \pm 1, \pm 2, \ldots, \tag{1.6}$$

it follows that

$$\rho_m \sim \hat{\rho}\sqrt{|m|}, \tag{1.7}$$

where ρ_m denotes the radius of the m'th orbital, and $\hat{\rho}$ is the Landau radius,

$$\hat{\rho} = \left(\frac{\hbar c}{eB}\right)^{1/2} = 2.5 \times 10^{-10}\text{cm} \times B_{12}^{-\frac{1}{2}}. \tag{1.8}$$

The exact expression (see below) is

$$\rho_m = \hat{\rho}\sqrt{2m+1}. \tag{1.9}$$

The semiclassical derivation can also be used to derive the critical field strength, below which the magnetic field ceases to dominate the motion. At the critical field strength,

$$\frac{Ze^2}{\rho_m^2} \sim \frac{eB_m v_m}{c} \sim \frac{eB_m \omega}{c\rho_m}. \tag{1.10}$$

This implies

$$B_m \sim \frac{Z^2}{(2m+1)^2} B_C, \tag{1.11}$$

where B_C, the critical field strength for hydrogen, is

$$B_C \sim 2.3 \times 10^9 \text{G}. \tag{1.12}$$

The Coulomb field has the strongest effect on the innermost orbital, $m = 0$ (Eq. 1.11). The magnetic field completely dominates only for $B > Z^2 B_C$. For iron this field is $\sim 10^{12}$G.

We now turn to the quantal solution of particle motion in a magnetic field. The problem was first solved by Landau, and the derivation is repeated in most quantum mechanics textbooks;[13] we will omit the details here, and will state only the results that are relevant for our purpose.

The magnetic Hamiltonian, H_B, separates into three parts,

$$H_B = H_z + H_\perp + H_S. \tag{1.13}$$

H_z governs the motion parallel to the field, $H_\perp$ the motion perpendicular to the field, and H_S the spin degree of freedom.

The magnetic field does not exert any force in the direction of the field, so that H_z includes only a kinetic energy part, $P_z^2/2M$. The eigenfunctions of H_z are plane waves and the spectra is continuous. $H_\perp$, on the other hand, has an infinitely degenerate, discrete harmonic-oscillator spectrum

$$E_\perp = \hbar\omega(2n - m + |m| + 1) \qquad n \geq 0, \tag{1.14}$$

where from (1.5),

$$\hbar\omega = 11.5 \text{ keV} \times B_{12}. \tag{1.15}$$

The integers n and $m = -L_z/\hbar$ label the eigenfunctions of $H_\perp$,

$$\Psi_{m\,n}(\rho, \phi) = W_{m\,n}(\rho) e^{-im\phi}, \tag{1.16}$$

where we introduced the Landau functions,

$$W_{m\,n}(\rho) = \frac{\sqrt{n!}}{\sqrt{2\pi(n + |m|)!\,\hat{\rho}^2}} \left(\frac{\rho}{\sqrt{2}\hat{\rho}}\right)^{|m|} e^{-\rho^2/4\hat{\rho}^2} L_n^{|m|}\left(\frac{\rho^2}{2\hat{\rho}^2}\right), \tag{1.17}$$

where $L_n^{|m|}$ are the associated Laguerre polynomials. We will need only the lowest-energy Landau functions. As we mentioned already, these functions are peaked at $\rho_m = \hat{\rho}\sqrt{2m+1}$.

The spectrum (1.14) is degenerate only for $m \geq 0$, but it increases linearly with $|m|$ for $m < 0$. This corresponds to the fact that classically, the electron moves only counterclockwise around the field; i.e., it has positive angular momentum.

The spin part of the Hamiltonian, H_S, is proportional to S_z

$$H_S = \frac{eB}{Mc} S_z = \pm \frac{\hbar\omega}{2}.$$

The one-body eigenfunctions of H_B are then products of the eigenfunctions of $H_z, H_\perp$ and H_S:

$$X_{n\,m\,k\,S} = W_{m\,n}(\rho) e^{-im\phi} e^{ikz} \mid S_z\rangle. \tag{1.18}$$

We now turn to the effects of the perturbing nucleus-electron attraction. The attraction breaks the degeneracy in m, since lower-m orbitals are closer to the nucleus. L_z is conserved by the spherically symmetric attraction, so orbitals with a different Landau index, m, are not mixed. Similarly, orbitals with different spin-projections are not mixed.

For sufficiently strong magnetic fields (Eq. 1.14), the excitation energy of orbitals with a non-zero quantum number, n, is much larger than the matrix elements of the Coulomb perturbation

$$\langle V_{en} \rangle \sim \frac{Ze^2}{\hat{\rho}} \sim 5\,\mathrm{keV} \times B_{12}^{\frac{1}{2}}. \tag{1.19}$$

Therefore, to zeroth order n remains a good quantum number.

Along the field, the Coulomb interaction localizes the electrons. The plane-wave is replaced by a real, localized, function with a finite number of nodes,

$$e^{ikz} \rightarrow f_{n\,m\,\nu}(z)$$

$$\int f^*_{n\,m\,\nu}(z) f_{n\,m\,\nu'}(z)\,dz = \delta_{\nu\,\nu'}, \tag{1.20}$$

where the index ν labels the number of nodes. In the following, we omit the index n from $f_{n\,m\,\nu}$, as only $n = 0$ states are considered. Higher-n orbitals have large energies ($\geq \hbar\omega$) and are not populated at the ground state. Notice that the difference between the effect of the perturbation on $H_\perp$ and H_z is due to the fact that the former has a discrete spectra.

Since the perturbation changes only the form of the eigenfunctions of H_z, the one-body orbitals remain separable,

$$X_{m\,\nu\,S} = W_{m\,0}(\rho) e^{-im\phi} f_{m\nu}(z) \mid S_z = -\frac{1}{2}\rangle. \tag{1.21}$$

The quantum numbers of the lowest energy state are: $m = 0,\ \nu = 0$. In the hydrogen atom, the single electron occupies this state. We can estimate the longitudinal extension of its wavefunction by replacing the probability distribution with that of a long cylinder, with radius $\hat{\rho}$ and length ℓ.[1] Roughly

$$E \sim \frac{\hbar^2}{2M\ell^2} - \frac{Ze^2}{\ell}\log(\frac{\ell}{\hat{\rho}}), \tag{1.22}$$

and minimization with respect to ℓ yields

$$\ell \sim \left(\frac{a_0/Z\hat{\rho}}{\log(a_0/Z\hat{\rho})}\right)\hat{\rho}, \tag{1.23}$$

and

$$E \sim -\frac{\hbar^2}{M(a_0/Z)^2}\log^2\left(\frac{a_0}{Z\hat{\rho}}\right) \sim -\frac{Ze^2}{\ell}\log\left(\frac{a_0}{Z\hat{\rho}}\right), \tag{1.24}$$

where $a_0 = 0.5 \times 10^{-8}$cm is the Bohr radius. In strong fields,

$$\hat{\rho} \ll \ell \ll a_0/Z, \tag{1.25}$$

so that the atom looks like a small cigar (Fig. 19).

It can be shown that in very strong fields the energy required to put the electron in a higher node state ($\nu > 0$) is higher than the energy required to put it in higher Landau orbitals, $m > 0$. We can undersand this fact qualitatively by noticing that a typical distance from the nucleus to electrons in states with one or more nodes is greater than ℓ, so their binding energy is of the order $1/\ell$

$$|E| \leq \frac{Ze^2}{\ell}. \tag{1.26}$$

On the other hand, the energy of an electron in a $\{m > 0, \nu = 0\}$ state is similar to (1.22), with $\hat{\rho}$ replaced by ρ_m; as the dependence of E on $\hat{\rho}$ is logarithmic, the energy is almost the same. The electron will lie in the state that is closer to the nucleus. Hence, in strong fields, the electrons of a general atom will occupy the states $\{m = 0, ..., Z-1; \nu = 0\}$. For intermediate-strength fields, the inner Landau orbitals are populated by several electrons; for example, the first six Landau orbitals of iron at 10^{12}G are each occupied by two or more electrons.

Although the ansatz (1.21) is strictly valid only for very strong fields, we can use it to calculate the cohesive energies, even at moderate field strengths, $B \sim Z^2 B_C$. The Coulomb perturbation will mix higher-n states only for the inner-m orbitals; these orbitals, however, are in the core of the atoms and will remain almost unmodified when the atoms join together to form a chain. Therefore, their contributions to the cohesive energy (as a function of separation) will almost cancel. For the same reason, we can ignore relativistic effects. These effects have also been shown to be much smaller than naively expected, because the wavefunction is also separable to perpendicular and parallel components in the relativistic case;[14] therefore, rather

than being proportional to $\hbar\omega/Mc^2$, the corrections are proportional to v_{en}/Mc^2, where v_{en} is the attraction of the nucleus felt by a single electron. From Eqs. (1.8,1.9) we deduce that even for the innermost orbital of iron, $m = 0$, the corrections are less than 4% for $B = 10^{13}$G, with much smaller corrections for the other electrons.

II. THE ANSATZ FOR ISOLATED ATOMS

Our main goal is to calculate the cohesive energy–the difference between the energy of isolated atoms and the minimum energy of atoms in crystals. These two binding energies are comparable, and for a meaningful calculation of their difference–or at least its sign (which tells us whether or not crystals are bound)–the errors in the calculations of the binding energies must be smaller than the cohesive energy. Experience with zero-field calculations leads us to expect that if the atoms are bound, the cohesive energy is a few percent of the total energy; the calculations must therefore be accurate to 1%. This argument can be reversed: in the event that no binding is found with a method that is accurate to at least 1% (as in our case), then the atoms are probably not bound, and the calculation does not have to be refined further.

We decided to use the Hartree-Fock method for the calculation. This method is more accurate than the restricted variational method .[8] Density-functional calculations for zero fields are also very successful, and therefore this method was adapted to strong fields, using an expression for the exchange energy taken from studies of uniform gas in strong fields.[9] However, the electron densities for strong fields are localized near the nucleus, and the deviations from uniformity will modify the exchange energy. Indeed, we later (Chapter VI) compare the Hartree-Fock and density-functional results and find that the later overestimate the exchange energies

by more than 30%, or 2% of the total binding energy.

In the Hartree-Fock method, the wavefunction is approximated by a Slater determinant of one-electron orbitals. These wavefunctions are determined by solving the variational equation,

$$\frac{\delta}{\delta\chi}\left(\frac{\langle\Psi|H|\Psi\rangle}{\langle\Psi|\Psi\rangle}\right) = 0. \tag{2.1}$$

The Slater determinant does not include electron-electron correlations, and the repulsion is included only through the mean field. The mean field is smaller in magnitude than V_{en}, and it does not break the cylindrical symmetry of the problem; it can therefore be ignored for the sake of our qualitative discussion. In strong fields, the one-body orbitals (1.11) are separable; the only unknowns are the one-dimensional functions $f_{m\nu}(z)$. The Hartree-Fock equations therefore reduce to a set of one-dimensional (coupled) equations

$$\frac{\delta}{\delta f_{m\nu}(z)}\left(\frac{\langle\Psi \mid H \mid \Psi\rangle}{\langle\Psi \mid \Psi\rangle}\right) = 0. \tag{2.2}$$

Most of the error in zero-field Hartree-Fock calculations is caused by the symmetrization of the spatial wavefunction of electrons in a spin-singlet state. In the full wavefunction, the electron-electron repulsion causes a depletion of the wavefunction for small relative distances (Coulomb hole); naive symmetrization of the orbitals causes the opposite effect. For electrons in a spin-triplet state, the antisymmetrization of the spatial wavefunction creates a hole that imitates the Coulomb hole. In strong fields, the spins are all aligned antiparallel to the field; all electron-pairs are in a spin-triplet state, and the Slater determinant reduces to a totally antisymmetric spatial determinant. The error is therefore significantly smaller than the 1% error associated with zero-field calculations.[12]

In the Hartree-Fock method, only the wavefunction is approximated, and the Hamiltonian is left intact. By the variational principle, first-order errors in the wavefunction induce only second-order errors in the Hamiltonian. Moreover, $\langle H \rangle$ is bounded from below, so successive improvements in the approximation can be seen. The method thus has an advantage over those that approximate the Hamiltonian. For zero-fields, the parameters in these latter approximations can be obtained by fitting the calculations to experimental data but for strong fields, no such comparison is possible.

III. CALCULATIONS FOR ISOLATED ATOMS

In the adiabatic approximation the expectation value of the Hamiltonian (1.1) in the wavefunction (1.18) is

$$E = \langle H \rangle = \langle H_B \rangle + \langle V_{en} \rangle + \langle V_{ee} \rangle, \tag{3.1}$$

where

$$\langle H_B \rangle = \langle H_z \rangle = \frac{\hbar^2}{2M} \sum_{m\nu} \int |f'_{m\nu}(z)|^2 \, dz \tag{3.2a}$$

$$\langle V_{en} \rangle = -\frac{Ze^2}{\hat{\rho}} \sum_{m\nu} \int V_m(z) \, |f_{m\nu}(z)|^2 \, dz \tag{3.2b}$$

$$\langle V_{ee} \rangle = \frac{e^2}{\hat{\rho}} \sum_{m\nu m'\nu'} \Big(\int D_{mm'}(z-z') \, |f_{m\nu}(z)|^2 \, |f_{m'\nu'}(z')|^2 - E_{mm'}(z-z') \, f_{m\nu}(z) f_{m'\nu'}(z') f^*_{m'\nu'}(z) f^*_{m\nu}(z') \Big) \, dz \, dz \,, \tag{3.2c}$$

with the nuclear, direct, and exchange kernels

$$V_m(z) = \int \frac{|W_{m0}(\rho)|^2}{\sqrt{\rho^2+z^2}} \rho \; d\rho \, d\phi = \int \frac{e^{-\frac{\rho^2}{2}} \rho^{2m+1}}{2^m m! \sqrt{\rho^2+z^2}} d\rho \tag{3.3a}$$

$$D_{mm'}(z-z') = \int \frac{e^{-\frac{\rho^2+\rho'^2}{2}} \rho^{2m+1} \rho'^{2m'+1}}{2^{m+m'} m! m'! \sqrt{(\rho-\rho')^2+(z-z')^2}} d\rho \, d\rho' \tag{3.3b}$$

$$E_{mm'}(z-z') = \int \frac{e^{-\frac{\rho^2+\rho'^2}{2}} (\rho\rho')^{m'+m+1} e^{-i(m-m')(\phi-\phi')}}{2^{m+m'} m! m'! \sqrt{(\rho-\rho')^2+(z-z')^2}} d\rho \, d\rho' \frac{d\phi}{2\pi} \frac{d\phi'}{2\pi}, \tag{3.3c}$$

and we used the fact that for the $n = 0$ orbitals, $\langle H_z \rangle = -\langle H_\perp \rangle$. The Hartree-Fock equations for the ground-state orbitals, (2.2), are equivalent to

$$\frac{\delta \langle \Psi | H | \Psi \rangle}{\delta f^*_{m\nu}(z)} = \epsilon_{m\nu} \frac{\delta \langle \Psi | \Psi \rangle}{\delta f^*_{m\nu}(z)}, \tag{3.4}$$

where the Lagrange multipliers, $\{\epsilon_{m\,\nu}\}$, ensuring the orthogonality relations (1.20), are the single-particle energies. From (3.1) – (3.3), it can be shown explicitly that these equations are

$$\left[-\frac{\hbar^2}{2M}\frac{d^2}{dz^2} - \frac{Ze^2}{\hat{\rho}}V_m(z) + \frac{e^2}{\hat{\rho}}K_m(z) - \epsilon_{m\nu}\right] f_{m\nu}(z) = \frac{e^2}{\hat{\rho}}J_{m\nu}(z), \tag{3.5}$$

where

$$K_m(z) \equiv \sum_{m'\nu'} \int D_{mm'}(z-z')|f_{m'\nu'}(z')|^2 dz' \tag{3.6a}$$

$$J_{m\nu}(z) \equiv \sum_{m'\nu'} f_{m'\nu'}(z) \int E_{mm'}(z-z') f^*_{m'\nu'}(z') f_{m\nu}(z') dz'. \tag{3.6b}$$

The Hartree-Fock equations are nonlinear and coupled. They are solved by iteration: in each iteration step, the direct and exchange terms, K and J, are calculated from the wavefunctions, and the equations (3.5) are then solved for the new set of wavefunctions. This procedure is easily represented in an algorithm form:

(i) Take a set of quantum numbers, $\{m\,\nu\}$, large enough to include those of all occupied states.

(ii) Guess the wavefunctions, f, and guess which states are occupied.

(iii) From (3.6) and the wavefunctions of the occupied states, obtain the integrals $\{K_m, J_{m\,\nu}\}$.

(iv) Calculate the total energy (3.2).

(v) Calculate the single-particle energies by taking the scalar products of equation (3.5) with the wavefunctions $f_{m\,\nu}$. The Z states with the lowest energy will be the occupied states.

(*vi*) With the kernels and the single-particle energies, solve (3.6) for the new wavefunctions. With the K and J, the equations are uncoupled and inhomogeneous; they are easily solved by the Green's function method.[15]

(*vii*) Orthonormalize the new wavefunctions.

(*viii*) Repeat (*iii*) – (*vii*) until the total energy converges.

There are several technical details that have to be explained; they will be described in the remainder of this chapter.

The energy is invariant with respect to reflections through the plane $z = 0$. Therefore the wavefunctions $\{f_{m\nu}\}$ are real and have a definite symmetry under $z \to -z$. The boundary conditions on the wavefunctions therefore are

$$f'_{m\nu}(0) = 0, \qquad \nu \text{ even}; \tag{3.7a}$$

$$f_{m\nu}(0) = 0, \qquad \nu \text{ odd}; \tag{3.7b}$$

$$f_{m\nu}(\infty) = 0; \tag{3.7c}$$

$$2\int_0^\infty f^2_{m\nu}(z)\,dz = 1. \tag{3.7d}$$

Notice that the wavefunctions of crystals do not have similar symmetries because they must satisfy the complex Bloch condition $f(x + a) = e^{ika} f(x)$.

The orbitals decay exponentially for large z, so we replace the half-line $[0, \infty)$ by a large cell $[0, \ell]$. By trial and error, we find that ℓ has to be at least as large as $50\hat{\rho}$. The differential equations and the quadratures are discretized in a uniform mesh, spanning the cell. Typically, a few hundred points are sufficient for convergence.

We used Fourier transformations to evaluate the convolution integrals in (3.6), since this method is faster than direct quadrature. For an array of N points, con-

volution using the Fast Fourier Transform algorithm[16] requires $\sim N \log_2 N$ arithmetical operations, while direct quadrature requires N^2 operations (since there are two independent variables, z and z'). Direct numerical evaluation of the Fourier transform is complicated by the $1/z$ falloff of the kernels, so we used the analytic expressions[7]

$$V_m(z) = \int_0^\infty L_m\left(\frac{q^2}{2}\right) e^{-q^2/2} e^{-q|z|} dq \tag{3.8a}$$

$$D_{mm'}(z) = \int_0^\infty L_m\left(\frac{q^2}{2}\right) L_{m'}\left(\frac{q^2}{2}\right) e^{-q^2} e^{-q|z|}\, dq \tag{3.8b}$$

$$E_{mm'}(z) = \int_0^\infty \left(\frac{m!}{m'!}\right)\left(\frac{q^2}{2}\right)^{m'-m} \left[L_m^{m'-m}\left(\frac{q^2}{2}\right)\right]^2 e^{-q^2} e^{-q|z|} dq, \tag{3.8c}$$

where L_n is the Laguerre polynomial and $L_n^{(\alpha)}$ is the associated Laguerre polynomial. We can assume $m' > m$ with no loss of generality. (These equations are proved in Ref. 7.) From the definition of the Laguerre polynomials, it is easy to show that the Fourier transform of the nuclear kernel is

$$\begin{aligned} V_m(q) \equiv \int_{-\infty}^{\infty} e^{iqz} V_m(z)\, dz &= \int_0^\infty \frac{y^m}{(y+q^2/2)^{m+1}} e^{-y}\, dy \\ &= \frac{\sqrt{2} m!}{|q|} e^{q^2/4} U_{-\frac{1}{2}-m,0}\left(\frac{q^2}{2}\right), \end{aligned} \tag{3.9}$$

where U is the Whittaker function, and the last equality follows from Eq. (13.1.33) in Ref. 17.

For small q we evaluate the Whittaker function from its expansion in $q^{2k} \log q$;[18] for larger q we integrate (3.9) numerically, by a change of variables,

$$y \to t = \frac{y}{y + y_{max}}, \tag{3.11}$$

where y_{max} is the point where the integrand reaches its maximum

$$y_{max} = \frac{1}{2}\left(\sqrt{\left(\frac{q^2}{2}+1\right)+2mq^2} - \left(\frac{q^2}{2}+1\right)\right), \tag{3.11}$$

The direct and exchange kernels are evaluated by expanding the product of the polynomials as a sum of Laguerre polynomials,

$$L_m\left(\frac{y}{2}\right) L_{m'}\left(\frac{y}{2}\right) = \sum_{s=0}^{m+m'} d_s(m,m')L_s(y) \tag{3.12a}$$

$$\frac{m!}{m'!}\left(\frac{y}{2}\right)^{m'-m}\left[L_m^{m'-m}\left(\frac{y}{2}\right)\right]^2 = \sum_{s=0}^{m+m'} g_s(m,m')L_s(y)\ , \tag{3.12b}$$

where the d's and g's are constant coefficients (i.e., independent of y). The direct kernels are then

$$D_{mm'}(z) = \frac{1}{\sqrt{2}}\sum_{s=0}^{m+m'} d_s(m,m')V_s\left(\frac{z}{\sqrt{2}}\right) \tag{3.13a}$$

$$D_{mm'}(q) = \sum_{s=0}^{m+m'} d_s(m,m')V_s(q\sqrt{2}), \tag{3.13b}$$

with a similar expression for the exchange kernels. The expansion (3.12) is essential for the calculation of the chain energy (Chapter V).

The coefficients d and g are evaluated by the Gram-Schmidt procedure. However, it turns out that here the calculation involves a delicate cancellation between different terms, and it runs into numerical instabilities. To overcome this problem, we use integer arithmetic. We first cast (3.12) in the form

$$\left(2^m\tilde{L}_m\left(\frac{y}{2}\right)\right)\left(2^{m'}\tilde{L}_{m'}\left(\frac{y}{2}\right)\right) = \sum_{s=0}^{m+m'}\tilde{d}_s(m,m')\tilde{L}_s(y) \tag{3.14}$$

where:

$$\tilde{L}_m(y) \equiv m!L_m(y) = e^y\frac{d^m(y^me^{-y})}{dy^m}, \tag{3.15}$$

$$\tilde{d}_s(m,m') \equiv \frac{2^{m+m'}(m+m')!}{s!} d_s(m,m'). \tag{3.16}$$

These polynomials have integer coefficients, and their leading coefficient is ± 1; from this follows that the $\tilde{d}$'s and the $\tilde{g}$'s are integers, and that the Gram-Schmidt reduction of (3.14) employs only integers. We wrote an integer arithmetic program that evaluates exactly all the coefficients with indexes $m, m' \leq 50$, $\ell \leq 100$. It was checked by testing the relations (3.12) for a few random y's.

The initial wavefunctions, taken from restricted variational studies, were of the form[8,19]

$$f_{m\nu} \propto \; z^{\nu} \exp(-a_{m\nu}|z|). \tag{3.17}$$

We used the parameters $\{a_{m\,\nu}\}$ as given in Ref. 19 but checked to see that the final solution is insensitive to wide variations in the parameters.

Since we do not know *a priori* which are the Z one-body states with the lowest energies, we have to calculate the single-particle energies of a large number of states. For our calculations of atoms up to iron, $Z \leq 26$, it is sufficient to include all zero-node states with $0 \leq m \leq Z-1$, together with 1- and 2-node states for $m \leq 10$. We verified that the results are not affected by the choice of initially occupied orbitals. Lists of occupied orbitals in the final solutions for various field strengths are presented below in Table 5.

IV. THE ANSATZ FOR MOLECULAR CHAINS

In this chapter we explain our ansatz for the calculation of structure of matter in strong fields. We follow earlier approaches in assuming that matter is composed of linear chains of regularly spaced stationary nuclei (Charge Z, spacing a), oriented along the magnetic field. [1,8] The ground-state spacing is found by minimizing the energy per atom as a function of a. As explained in the introduction, different chains are kept apart by Pauli repulsion, since the electrons are constrained to stay in the Landau orbitals. Electrons move freely along the field but not perpendicular to it. In other words, matter in strong fields is a conductor along the field line and an insulator perpendicular to the field, like a classical plasma in a magnetic field.

Since the chain-chain interaction does not change the structure of the chain, the interaction can be calculated with the wavefunctions of the single-chain approximation. A numerical study in Ref. (10) shows that the additional attraction is very small (less than 1% of the binding energy). With the curves of energy *vs.* spacing used in Ref. (10), this attraction will bind iron weakly; however, the curves we calculated are much stiffer, and the attraction will therefore bind iron very weakly, if at all.

The ansatz for the chain-wavefunction is similar to the isolated-atom ansatz. We assume a determinental trial wavefunction composed of single-particle wavefunctions. In the adiabatic approximation the single-particle orbitals are

$$\psi_{m\nu k}(\rho,\phi,z) = L_{-m0}(\rho,\phi)\; f_{m\nu k}(z)\; |S_z = -\frac{1}{2}\rangle \;, \tag{4.1}$$

where the node index ν is supplemented by the continuous quasi-momentum index k. The quasi-momenta fill continuous bands

$$|k| \leq \frac{\sigma_{m\nu}\pi}{a}, \tag{4.2}$$

where we introduced the band-occupation index, $\sigma_{m\,\nu}$. The periodicity imposes the Bloch condition,

$$f_{m\nu k}(z+a) = f_{m\nu k}(z)e^{ika}. \tag{4.3}$$

We must make an ansatz for the k-dependence of $f_{m\,\nu\,k}$. This ansatz must be compatible with the Pauli principle–different orbitals must be orthogonal. As a corollary of the Bloch condition, orbitals with quasi-momenta k, k' that differ by noninteger multiples of $2\pi/a$ $\left(k \neq k' \bmod(2\pi/a)\right)$ will be automatically orthogonal

$$\begin{aligned}\int_{-\infty}^{\infty} f^*_{m\nu' k'}(z)\; f_{m\nu k}(z)\; dz &= \left(\sum_{n=-\infty}^{\infty} e^{i(k-k')na}\right) \int_{-a/2}^{a/2} f^*_{m\nu' k'}(z)\, f_{m\nu k}(z)\; dz \\ &= 0, \qquad \text{if } k \neq k' \bmod(\frac{2\pi}{a});\end{aligned} \tag{4.4}$$

but we must impose orthogonality for $k = k' \bmod(2\pi/a)$.

We adopt the plane-wave ansatz,

$$f_{m\nu k}(z) = f_{m\nu}(z)e^{ikz}, \tag{4.5}$$

where $f_{m\,\nu}$ are k-independent periodic functions (period a). These functions are determined by the variational equations (Chapter III). As in the isolated-atom case, the functions must satisfy

$$\int_{-a/2}^{a/2} f^*_{m\nu'}(z)\, f_{m\nu}(z)\; dz = \delta_{\nu\,\nu'}. \tag{4.6}$$

In addition, we must impose

$$\int_{-a/2}^{a/2} f^*_{m\nu'}(z)\, f_{m\nu}(z) e^{i(k-k')z}\, dz = 0 \qquad \text{if } (k-k') = \frac{2n\pi}{a},\ n \neq 0. \tag{4.7}$$

The simplest way to satisfy (4.7) is to ensure that the condition on the right will never be satisfied, i.e., to choose

$$\sigma_{m\nu} < 1. \tag{4.8}$$

An alternative choice for the k-dependence, which allows the use of high quasi-momenta, $\sigma_{m\,\nu} > 1$, is to modify the phase dependence [20]

$$f_{mk}(z) = e^{ika\int^z |f_m|^2 dz} f_m(z). \tag{4.9}$$

In order to satisfy the Pauli principle, we allow only one k-independent function, $f_{m\,\nu}$, for each Landau orbital. In the ground state, all these functions have zero nodes, $\nu = 0$, and we omit the ν index.

The two alternative phase factors, ikz and $ika\int |f_{m\,0}|^2\, dz$, have the same variation along the unit cell, a. The modified phase varies most rapidly in the region of largest amplitude, unless f_m is constant (in which case the phase factors are equal); consequently, the kinetic energy associated with it is higher. $\langle V_{en}\rangle$ and $\langle V_{ee}\rangle$ depend only on the amplitude of the wavefunction, and therefore do not depend on the choice of phase.

The two choices correspond to two different physical pictures. For large internuclear spacing, the z-dependent wavefunctions should approach the isolated-atoms wavefunctions; in that case the plane-wave ansatz, (4.5), is appropriate. Note, however, that for very large spacings the Bloch-wave ansatz is not appropriate. Lower

kinetic energy is obtained by replacing the z in the phase factor with any function that varies only in the region where f is very small.

$$f_{m\nu k}(z) = f_{m\nu}(z)e^{ikg(z)}, \quad g(z+a) = a + g(z)$$

$$g(z) \neq 0 \text{ only if } z \sim na + a/2, \quad n = 0, \pm 1, \pm 2, ... \tag{4.10}$$

In this ansatz, the kinetic energy associated with g is proportional to

$$\int (dg/dz)^2 |f_{m\nu}(z)|^2 \, dz \sim |f_{m\nu}(a/2)|^2 \int (dg/dz)^2 dz,$$

so it decreases exponentially with a, rather than as a power of a.

The modified plane-wave choice seems more natural as an extension of a uniform-matter picture (f_m constant); higher nodes are replaced by high quasi-momenta, and the spectrum is continuous. In the uniform density limit, the phase-factors are equal; but for slight perturbations from uniformity, only the modified plane-waves can naturally accommodate the Pauli principle without artifically restricting the maximum band occupation, $\sigma_{m\nu}$, to be less than 1.

Only the plane-wave choice (4.5) allows a feasible calculation of the exchange term, so we could not check the alternative choice. However, we do not believe that the alternative choice gives a lower energy. At every spacing, only the inner cores (low m) have high occupations, $\sigma_m > 1$. Unless the spacing is small, the core-orbitals in a chain will be similar to those of isolated atoms; the plane-wave choice is more appropriate for them. For the high-m orbitals the incorporation of high quasi-momenta in the modified plane-wave choice is irrelevant, as even the zero-node band is not filled, $\sigma_{m0} < 1$ (Fig. 21). Without this advantage, the modified plane-wave choice is clearly inferior, as it induces higher kinetic and exchange energies.

V. CALCULATIONS FOR MOLECULAR CHAINS

The Hamiltonian of a molecular chain is the periodic extension of (1.1):

$$H = H_B + V_{en} + V_{ee} + V_{nn}, \tag{5.1}$$

where H_B, V_{ee}, and V_{en} are now:

$$H_B = \sum_i \frac{1}{2M}(\mathbf{p}_i + \frac{e}{c}\mathbf{A}_i)^2 - \sum_i \frac{e}{mc}\mathbf{B}\cdot\mathbf{S_i}, \tag{5.2}$$

$$V_{ee} = e^2 \sum_{i<j} \frac{1}{r_{ij}}, \tag{5.3}$$

$$V_{en} = -Ze^2 \sum_i \sum_{n=-\infty}^{\infty} \frac{1}{|\mathbf{r_i} - na\hat{\mathbf{z}}|}\ , \tag{5.4}$$

where a is the internuclear spacing and the index i labels all electrons in the chain. The new term, V_{nn}, accounts for the repulsion of different nuclei

$$V_{nn} = \frac{Z^2e^2}{2} \sum_{n\neq n'} \frac{1}{|n'a - na|}. \tag{5.5}$$

The Coulomb interactions, V_{en}, V_{ee}, and V_{nn} each have an unphysical logarithmic divergence, but since the system is neutral, their sum is finite.

We regularize the divergence by adopting periodic boundary conditions. We assume that the wavefunctions have a period Na, where N is large and the limit $N \to \infty$ is taken at the end of the calculations. This is different from assuming a finite chain with N atoms. Both regularizations give the same total energy in

the large N limit; however, they give different numbers for each part of the energy. The divergences in each part are independent of the regularization. Therefore, an inconsistent evaluation will produce a result that is finite but wrong. For example, inconsistent evaluation led Ref. 21 to obtain an erroneously large cohesive energy.

As a result of the periodic boundary conditions, the range of the z-integrals in $(5.1-5.2)$ is restricted to $-Na/2 < z < Na/2$ and $-Na/2+z < z' < Na/2+z$. Similar restrictions hold for the summations over nuclei. In addition, the Bloch momentum is discrete

$$k = 0,\ \pm\frac{2\pi}{Na},\ \pm\frac{4\pi}{Na},\ldots\ \pm\frac{2N_{m\nu}\pi}{Na}, \tag{5.6}$$

where the definition (4.2) of the occupation factor implies $N_{m\,\nu} = N\sigma_{m\,\nu}/2$.

In the adiabatic ansatz, the various terms in the total energy take the form:

$$\langle H_B\rangle = \langle\frac{P_z^2}{2M}\rangle = \frac{\hbar^2}{2M}\sum_{m\nu k}\left[k^2 + \int\limits_{|z|<Na/2} |f'_{m\nu}(z)|^2\,dz\right] \tag{5.7a}$$

$$\langle V_{en}\rangle = -\frac{Ze^2}{\hat{\rho}}\sum_{m\nu k}\int\limits_{|z|<Na/2} V_m(z)|f_{m\nu}(z)|^2\,dz \tag{5.7b}$$

$$\langle V_{ee}\rangle = \frac{e^2}{\hat{\rho}}\sum_{\substack{m\nu k\\ m'\nu'k'}}\int\limits_{\substack{|z|<Na/2\\ |z-z'|<Na/2}}\Big(D_{mm'}(z-z')\,|f_{m\nu}(z)|^2\,|f_{m'\nu'}(z')^2$$

$$-\,G_{mm'}(z-z')\,f_{m\nu}(z)\,f_{m\nu}(z')\,f^*_{m\nu}(z)\,f^*_{m\nu}(z')\,e^{i(k-k')(z-z')}\Big)\,dz\,dz' \tag{5.7c}$$

$$\langle V_{nn}\rangle = \frac{NZ^2e^2}{a\hat{\rho}}\sum_{n=1}^{N/2}\frac{1}{n}, \tag{5.7d}$$

with the nuclear, direct and exchange kernels as defined in (5.1). From the periodicity of the wavefunctions and from (5.6), it follows that the energies per unit cell

are

$$E_B \equiv \langle H_B \rangle / N = \frac{\hbar^2}{2M} \sum_{m\nu} \sigma_{m\nu} \left[\frac{1}{3} (\frac{\pi \sigma_{m\nu}}{a})^2 + \int |f'_{m\nu}(z)|^2 \, dz \right] \tag{5.8a}$$

$$E_{en} = -\frac{Ze^2}{\hat{\rho}} \sum_{m\nu} \sigma_{m\nu} \int \tilde{V}_m(z) \, |f_{m\nu}(z)|^2 \, dz \tag{5.8b}$$

$$E_{ee} = \frac{e^2}{\hat{\rho}} \sum_{m\nu m'\nu'} \sigma_{m\nu}\sigma_{m'\nu'} \int \Big(\tilde{D}_{mm'}(z-z') \, |f_{m\nu}(z)|^2 \, |f_{m'\nu'}(z')|^2 \tag{5.8c}$$

$$- \tilde{G}_{m\nu m'\nu'}(z-z') \, f_{m\nu}(z) \, f_{m\nu}(z') \, f^*_{m\nu}(z) \, f^*_{m\nu}(z') \Big) \, dz \, dz', \tag{5.8d}$$

where all integrals are now taken over the unit cell $[-a/2, a/2]$. The modified kernels are

$$\tilde{V}_m(z) = \sum_{n=-N/2}^{N/2} V_m(z_n) \tag{5.9a}$$

$$\tilde{D}_{mm'}(z) = \sum_{n=-N/2}^{N/2} D_{mm'}(z_n) \tag{5.9b}$$

$$\tilde{G}_{m\nu m'\nu'}(z) = \sum_{n=-\infty}^{\infty} \frac{\sin(\sigma_{m\nu} z_n \pi/a)}{\sigma_{m\nu} z_n \pi/a} \frac{\sin(\sigma_{m'\nu'} z_n \pi/a)}{\sigma_{m'\nu'} z_n \pi/a} G_{mm'}(z_n), \tag{5.9c}$$

where $z_n \equiv z - na$, and the modified exchange kernels depend on the nodes ν, ν', through their dependence on the occupation numbers. For large z, the Bloch factor in (5.9) falls as z^{-2}; therefore, the sum (5.9) is convergent, and we replace the limits $\pm N/2$ by $\pm\infty$.

As in Chapter III, we obtain the Hartree-Fock equations by differentiating the total energy. It is easy to show that the resulting equations are

$$\left[\frac{\hbar^2}{2M} \left(-\frac{d^2}{dz^2} + \frac{1}{3} \left(\frac{\sigma_{m\nu}\pi}{a} \right)^2 \right) - \frac{Ze^2}{\hat{\rho}} \tilde{V}_m(z) + \frac{e^2}{\hat{\rho}} \tilde{K}_m(z) - \epsilon_{m\nu} \right] f_{m\nu}(z)$$

$$= \frac{e^2}{\hat{\rho}} \tilde{J}_{m\nu}(z), \tag{5.10}$$

where

$$\tilde{K}_m(z) \equiv \sum_{m'\nu'} \sigma_{m'\nu'} \int \tilde{D}_{mm'}(z-z') \, |f_{m'\nu'}(z')|^2 dz' \tag{5.11a}$$

$$\tilde{J}_{m\nu}(z) \equiv \sum_{m'\nu'} \sigma_{m'\nu'} f_{m'\nu'}(z) \int \tilde{G}_{m\nu m'\nu'}(z-z') \, f^*_{m'\nu'}(z') \, f_{m\nu}(z') \, dz'. \tag{5.11b}$$

The occupation numbers are determined by the variational equations

$$\epsilon_{Fm\nu} \equiv \frac{\partial E}{\partial \sigma_{m\nu}} = \epsilon_F, \tag{5.12}$$

where the Fermi energy, ϵ_F, is the Lagrange multiplier associated with the fixed electron-number constraint,

$$\sum_{m\nu} \sigma_{m\nu} = Z. \tag{5.13}$$

ϵ_F is the binding energy of electrons on top of the Fermi sea; $\epsilon_{F\,m\,\nu}$ is the energy of electrons on top of the $m\,\nu$ band. In our ansatz (Chapter IV), the occupation numbers do not exceed 1, so the Fermi energy of fully occupied orbitals ($\sigma_{m\,\nu} = 1$) is lower than ϵ_F.

The maximum energy in a band is higher than the average energy of that band

$$\epsilon_{F\,m\,\nu} > \epsilon_{m\,\nu}. \tag{5.14}$$

The two energies differ in their kinetic energy coefficients and in their exchange kernels. From (5.9c, 5.12), the Fermi exchange kernel is

$$\tilde{G}_{F\,m\nu m'\nu'}(z) = \sum_{n=-\infty}^{\infty} \cos(\sigma_{m\nu} z_n \pi/a) \frac{\sin(\sigma_{m'\nu'} z_n \pi/a)}{\sigma_{m\nu} z_n \pi/a} G_{mm'}(z_n). \tag{5.15}$$

The occupation numbers are determined by iteration. We separate the single particle Fermi energy into the plane wave kinetic-energy part and the remainder

$$\epsilon_{Fm\nu} = \frac{\hbar^2}{2M} \left(\frac{\sigma_{m\nu}\pi}{a}\right)^2 + \left[\frac{\hbar^2}{2M} \int |f'_{m\nu}(z)|^2 + \frac{\partial E_{en}}{\partial \sigma_{m\nu}} + \frac{\partial E_{ee}}{\partial \sigma_{m\nu}}\right]. \tag{5.16}$$

In each iteration of the wavefunctions (Chapter III), we calculate the remainder in (5.16) using the old occupation numbers. We then find the new occupation numbers that solve (5.12, 5.13, and 5.16). These numbers are found by subiteration; the program guesses ϵ_F, determines $\sigma_{m\nu}$ from (5.12 and 5.13) (subject to $0 < \sigma_{m\nu} < 1$), and checks to see whether $\sum \sigma_{m\nu}$ is lower or higher than Z; if it is higher, the subiteration is repeated with a lower ϵ_F, and vice-versa.

The chain equations generalize the isolated-atom equations (the latter are a special case, $a = \infty$). The equations are solved similarly, except for a few technical complications thath occur for finite spacing.

The boundary conditions at infinity are replaced by

$$f'_{m\nu}\left(\frac{a}{2}\right) = 0 \qquad \nu \text{ even} \tag{5.17a}$$

$$f_{m\nu}\left(\frac{a}{2}\right) = 0 \qquad \nu \text{ odd}, \tag{5.17b}$$

The large cell $[0, \ell]$ is replaced by half of the unit cell, $[0, a/2]$.

The summation over cells is best handled by Fourier transformation. Let us remind ourselves of the definition of Fourier transformation:

$$h(z) = \frac{1}{a} \sum_{n=-\infty}^{\infty} e^{-iq_n z} h(q_n) \tag{5.18a}$$

$$h(q) \equiv \int_{z=-a/2}^{a/2} e^{iqz} h(z)\, dz, \tag{5.18b}$$

where $q_n \equiv 2\pi n/a$, and the integrals are over the unit cell. For a periodic kernel of the form (5.9),

$$\tilde{h}(z) = \sum_n h(z_n),$$

the integral over the unit cell is simply

$$\tilde{h}(q) = \int_{z=-Na/2}^{Na/2} e^{iqz} h(z)\, dz \to h(q), \tag{5.19}$$

with the exception of $q = 0$, where the integral diverges.

The transformation to Fourier space isolates the divergence in the $q = 0$ part, and eliminates the dependence of the divergence on the wavefunction:

$$\int V(z)|f(z)|^2 dz = \frac{1}{a}\sum_n \int V(q_n)|f(z)|^2 e^{-iq_n z} dz + \frac{1}{a}V(q=0), \tag{5.20}$$

with a similar expression for the direct kernel. The Fourier sum converges rapidly. The summation of the diverging parts must be done before the limit $N \to \infty$ is taken.

For the nucleus-electron interaction, the $q = 0$ part is

$$\begin{aligned} E_{en}\,(q=0) &= -\frac{Ze^2}{a\hat{\rho}} \sum_{m\nu} \sigma_{m\nu} \int_{-a/2}^{a/2} \tilde{V}_m(q=0)|f_{m\nu}|^2\, dz \\ &= -\frac{Ze^2}{a\hat{\rho}} \sum_{m\nu} \sigma_{m\nu} F_{m\nu} \int_{-Na/2}^{Na/2} V_m\,(z')\, dz', \end{aligned} \tag{5.21}$$

where

$$F_{m\nu} = \int_{-a/2}^{a/2} |f_{m\nu}\,(z)\,|^2\, dz = 1. \tag{5.22}$$

Note that $F_{m\,\nu}$ must be included explicitly because it contributes to $\delta E/\delta f_{m\,\nu}(z)$ and therefore to $\epsilon_{m\,\nu}$. To save space, we will occasionally omit it from the equations. From the representation of the nuclear kernel (3.3), we evaluate the integral. For large N,

$$\begin{aligned} &\int_{-Na/2}^{Na/2} V_m\,(z')\, dz' = \frac{2}{m!} \int_0^\infty e^{-y} y^m dy \int_0^{Na/2} \frac{dz}{\sqrt{2y+z^2}} \\ &\to \frac{2}{m!} \int_0^\infty e^{-y} y^m \log\left(\frac{Na}{\sqrt{2y}}\right) dy \;\; = 2\log(Na) - \psi(m+1), \end{aligned} \tag{5.23}$$

where $y \equiv \rho^2/2$, and $\psi(m)$ is the logarithmic derivative of the Γ function. The last two equations imply that

$$E_{en}(q=0) = -\frac{2e^2Z^2}{a\hat{\rho}}\left(\log(Na) - \frac{1}{2Z}\sum_{m\nu}\sigma_{m\nu}\psi(m+1)\right). \tag{5.24}$$

The $q=0$ part of the direct interaction is evaluated similarly:

$$\begin{aligned} E_{ee}(q=0) &= \frac{e^2}{a\hat{\rho}}\sum_{m\nu m'\nu'}\sigma_{m\nu}\sigma_{m'\nu'}\int_{-a/2}^{a/2}\tilde{D}_{mm'}(q=0)|f_{m\nu}(z)|^2\,dz|f_{m'\nu'}(z')|^2\,dz' \\ &= \frac{e^2}{a\hat{\rho}}\sum_{m\nu m'\nu'}\sigma_{m\nu}\sigma_{m'\nu'}F_{m\nu}F_{m'\nu'}\sum_l d_l(m,m')V_l(q=0) \\ &= \frac{e^2Z^2}{a\hat{\rho}}\left(\log\left(\frac{Na}{2}\right) - \frac{1}{2Z^2}\sum_{m\nu m'\nu'}\sigma_{m\nu}\sigma_{m'\nu'}Y_{mm'}\right), \end{aligned} \tag{5.25}$$

where

$$Y_{mm'} \equiv \sum_l^{m+m'} d_l(m,m')\psi(l+1), \tag{5.26}$$

and we used both the expansion (3.13) and the sum rule for the d coefficients

$$\sum_l d_l(m,m') = 1, \tag{5.27}$$

which is a special case ($y=0$) of the definition (3.12).

To the $q=0$ part we must add the nucleus-nucleus repulsion

$$E_{nn} = \frac{Z^2}{a\hat{\rho}}\sum_{j=1}^{N/2}\frac{1}{j} \to \frac{Z^2}{a\hat{\rho}}\left(\log\left(\frac{N}{2}\right)+\gamma\right), \tag{5.28}$$

where γ is the Euler constant, 0.577... .

The finite sum of the divergences (Eqs. 5.24, 5.25, and 5.28) is

$$E(q=0) = \frac{Z^2e^2}{a\hat{\rho}}\left(-\log(2a)+\gamma+\frac{1}{Z}\sum_{m\nu}\sigma_{m\nu}\psi(m+1) - \frac{1}{2Z^2}\sum_{mm'}\sigma_{mm'}Y_{mm'}\right). \tag{5.29}$$

This sum is the total potential energy of a chain of electrons that are distributed uniformly along the z axis $\left(f_{m\,\nu}(z) = \text{constant}\right)$. Numerical comparisons show that this expression agrees with the expression that Refs. (8, 21) obtained by a different method.

A careful inclusion of the $F_{m\,\nu}$ factors shows that the $q = 0$ contribution to the single-particle energies is

$$\epsilon_{m\nu} = \epsilon_{m\nu}\,(q \neq 0) + \frac{Ze^2}{a\hat{\rho}}\left(-2\log(2) + \psi(m+1) - \frac{1}{Z}\sum_{m'\nu'}\sigma_{m'\nu'}Y_{mm'}\right), \quad (5.30)$$

with an identical contribution to the Fermi energy.

The Bloch factor modifies the transformation of the exchange kernels to Fourier space

$$\tilde{G}_{m\nu m'\nu'}(q) = \frac{1}{2\pi}\int B(q')G_{mm'}(q-q')dq', \quad (5.31)$$

where we introduced the Fourier transform of the Bloch factor, $B(z)$,

$$B\,(z) = \frac{\sin(\sigma_{m\nu}z\pi/a)}{\sigma_{m\nu}z\pi/a}\frac{\sin(\sigma_{m'\nu'}z\pi/a)}{\sigma_{m\nu}z\pi/a}. \quad (5.32)$$

$B(q)$ is a "chopped tent" function

$$B(q)=\begin{cases} a\sigma_{m\nu}, & a|q|/\pi < (\sigma_{m\nu} - \sigma_{m'\nu'}) \\ a(\sigma_{m\nu}+\sigma_{m'\nu'}-a|q|/\pi), & (\sigma_{m\nu} - \sigma_{m'\nu'}) < a|q|/\pi < (\sigma_{m\nu} + \sigma_{m'\nu'}) \\ 0 & (\sigma_{m\nu} + \sigma_{m'\nu'}) < a|q|/\pi, \end{cases} \quad (5.33)$$

where, with no loss of generality, we assume $\sigma_{m\,\nu} > \sigma_{m'\,\nu'}$. The modified kernel can be written in the form

$$G_{m\nu m'\nu'} = \sum_l g_l(m,m')\left(\alpha\int V_l(q')dq' + \beta\int V_l(q')q'dq'\right), \quad (5.34)$$

where the coefficients (α, β) and the integration limits are functions of $q, \sigma_{m\,\nu}$, and $\sigma_{m'\,\nu'}$, that are easily read from (5.33). In our program we first calculate the integrals

$$\int_0^p V_l(q)dq, \qquad \int_0^p qV_l(q)dq, \tag{5.35}$$

for a sufficiently fine grid of p's. Then, for each set $\{m\,\nu, m'\,\nu', q_n\}$ we determine the integration limits in (5.34) and interpolate the two functions (5.35). We could avoid the interpolation by approximating the dependence of (5.34) on $\sigma_{m\,\nu}$ by an effective mass. Similar approximation is often used in band structure calculations; we did not use it because the errors it induces in this case are not necessarily small.

The number of p grid points that are necessary to reach convergence depends on the internuclear spacing, a; typically, a few thousand points for each Landau orbital are sufficient.

To reduce computation time, we replace the probability density of the outer-orbitals with a constant. The precise balance between the number of z-dependent and z-independent wavefunctions depends on the internuclear spacing; for iron, we found that beyond $l = 35$ constant wavefunctions were good approximations, at least for internuclear spacings where the outer orbitals are not empty.

The number of fully and partially occupied orbitals increases as the internuclear spacing is decreased; eventually it increases beyond our numerical capabilities. But with the 50 Landau orbitals that we use for calculating iron structure, the energy at the minimum radius is much higher than the isolated-atom energy (by $\sim 30\%$; see Chapter VI, Fig. 20). This energy is high enough that we can be certain that there is no deep minima in smaller spacing.

VI. RESULTS

Table 1 shows the energy of isolated helium, carbon, and iron atoms at two field strengths, $B_{12} = 1$ and $B_{12} = 5$, together with a comparison to previous calculations. Table 2 displays some properties of the iron atom solution. We reproduce the helium calculations of Ref. 7 to five significant digits. As another check, we note that for iron at $B_{12} = 5$ a combination of the Hartree energy (Ref. 9) with the exchange energy from variational calculations yields an approximate Hartree-Fock energy -106.18 keV (Ref. 9), in agreement with our result, -106.09 keV. Our binding energies are slightly lower than those in the density-functional calculations. As explained in Chapter III, we think that this difference can be attributed to the fact that the exchange functionals in the latter method are approximated by a uniform density expression, while the Landau orbitals for the present case are actually well localized in the plane perpendicular to the field and do not resemble plane waves.

Fig. 20 shows the energy per unit cell as a function of internuclear spacing. We find that helium is bound in chains, in agreement with Refs. 8 and 9; our binding energies are 25 eV for $B_{12} = 1$ and 150 eV for $B_{12} = 5$. However, we find that carbon and iron chains are not bound. Repeating our calculations for $Z = 3$ through 5, we find that atoms with $Z > 2(4)$ are unbound at $B_{12} = 1(5)$. The shapes of the curves agree approximately with the density-functional results; the differences can again be attributed to the approximate treatment of the exchange

interaction in Ref. 9

For large internuclear spacings, the binding energy of the chain (relative to that of the isolated atom) is dominated by the (a^{-2}) repulsion term from the Bloch plane-waves. However, as we explained in Chapter IV, for very large spacings the $e^{ikz}f(z)$ ansatz is not appropriate, and a better ansatz gives an exponentially decreasing kinetic energy. The total energy will therefore be dominated by the a^{-5} quadropole-quadropole attraction, which dominates the interaction energy of a system of two separated atoms.

The chain-chain interaction may bind atoms in a chain even if isolated chains are unbound. The cohesive energy is estimated to be smaller than 0.5 keV. However, most physical consequences of such weak binding are similar to those of no binding. For example, matter in the crust of neutron stars has to be bound by at least 3 keV to be able to resist the strong electric field, which tries to tear matter from the surface.

Our interest in this problem was sparked by the confusion over the results of restricted variational calculations.[8] Originally, these calculations predicted large cohesive energy; later, numerical errors were found and the corrected calculations predicted that chains are unbound. However, as Table 1 shows, even the corrected calculations underestimate the absolute binding energies by 5 percent, which is higher than the cohesive energy.

Table 3 shows the single-particle energies of isolated iron atoms at $B_{12} = 5$; also shown are the different components of the energies: kinetic, nucleus-electron Coulomb attraction, direct electron-electron repulsion, and exchange. Fig. 21 shows

the single-particle energies and the Fermi energies of helium, oxygen, and iron at $B_{12} = 5$, as functions of the internuclear spacing.

For completeness, Table 4 displays isolated-atoms energies for all atoms up to $Z = 18$ at various field strengths. As shown in Fig. 22, the energy follows a $Z^{9/5} B^{2/5}$ dependence, in accordance with theoretical studies[22]. From the figure we derive

$$E \sim -158\,\mathrm{eV} \times Z^{9/5} B_{12}^{2/5}, \tag{6.1}$$

while in Ref. 22 an approximate bound of -170 keV for the coefficient was found. This expression holds for fields that are strong, but not ultra-strong. In Ref. 19 it is shown that when the magnetic field is very large, $B \geq 2Z^3 B_C$, the $B^{2/5}$ dependence is replaced by a logarithmic dependence, in accordance with the qualitative estimates in Chapter I.

We found that for $Z \leq 18$ only zero-node ($\nu = 0$) and one-node ($\nu = 1$) states are occupied. Lists of occupied one-node states for all atoms up to $Z = 18$ and for iron, for various field strengths, are presented in Table 5.

The calculation breaks down and the Fermi energy increases above 0 at very small internuclear spacings, as a result of the finite number of orbitals that the calculation includes (Chapter V).

In conclusion, we find that chains of heavy atoms in strong magnetic fields are unbound. We expect that corrections to our calculations – correlation, k-dependence in bands, and chain-chain interactions – will not change this result; at most they will induce a very weak ($\sim 1\%$) cohesive energy.

References

(1) M. A. Ruderman, Phys. Rev. Lett. **27** (1971) 1306.

(2) R. Lenzen and J. Trümper, Nature **271** (1976) 216.

(3) S. Shapiro and S. Teukolsky, *Black Holes, White Dwarfs, and Neutron Stars* (Wiley, New York, 1983). This book contains a good introduction to the physics of neutron stars.

(4) H. Ruder, H. Herold, W. Rösner, and G. Wunner, Physica **127B** (1984) 11.

(5) F. G. Smith, *Pulsars* (Cambridge University Press, Cambridge, 1977) p. 52.

(6) E. R. Harrison, E. Tademaru, and G. Greenstein, Nature **308** (1984) 826.

(7) J. Virtamo, J. Phys. B. **9** (1976) 751, and P. Pröschel, W. Rösner, G. Wunner, and H. Herold, J. Phys. B. **15** (1982) 1959.

(8) E. G. Flowers, J. F. Lee, M. A. Ruderman, P. G. Sutherland, W. Hillbrandt, and E. Müller, Astrophys. J. **215** (1977) 291. Numerical errors in this paper were found and corrected by E. Müller, Astron. Astrophs. **130** (1984) 415.

(9) P. B. Jones, Phys. Rev. Lett., **55** (1985) 1338.

(10) P. B. Jones, Mon. Not. R. astr. Soc. **218** (1986) 477.

(11) J. E. Skjervold and E. Östgaard, Physica Scripta **29** (1984) 543.

(12) M. Weissbluth, *Atoms and Molecules* (Academic Press, New York, 1978) p. 400.

(13) L. D. Landau and E. M. Lifshitz, *Quantum Mechanics* (Pergamon Press, Oxford, 1965) second edition, p. 421.

(14) C. Angelie and C. Deutch, Phys. Lett. **67A** (1978) 353.

(15) S. E. Koonin, *Computational Physics* (Benjamin/Cummings, Menlo Park,

California, 1986) p. 49.

(16) W. H. Press, B. P. Flannery, S. A. Teukolsky, and W. T. Vetterling, *Numerical Recipes* (Cambridge University Press, Cambridge, 1986) p. 390.

(17) M. Abramowitz and I. A. Stegun, *Handbook of Mathematical Functions* (National Bureau of Standards, Washington D. C., 1970) p. 504.

(18) I. S. Gradshteyn and I. M. Ryzhik, *Table of Integrals Series and Products* (Academic Press, New York, 1965) Eq. (9.237), p. 1063.

(19) J. F. Lee, Ph. D. Thesis, Columbia University (1976).

(20) J. Callaway and N. H. March, Solid State Physics **38** (1984) 136.

(21) M. L. Glaser and J. I. Kaplan, Astrophys. J. **199** (1975) 208.

(22) A. R. P. Rau, R. O. Mueller, and L. Spruch, Phys. Rev. **A11** (1975) 1865.

Table 1

Absolute values of the ground-state binding energies of atoms as calculated in the Hartree-Fock scheme are compared with density-functional[9] (DF), density-functional with correlations[9] (SIC), Thomas-Fermi-Dirac[11] (TFD), and restricted-variational[8] (RV) calculations. Energies are given in keV. All references are from Part 2.

Z	B_{12}	HF	DF	SCI	TFD	RV
2	1	0.57532				0.545
	5	0.958	1.040			0.913
6	1	4.230			4.14	
	5	7.668	8.03		7.73	
26	1	55.10	56.1		56.21	53.13
	5	106.09	108.18	108.85	105.89	101.7

Table 2

Ionization and K-shell energies, and the kinetic, nuclear-electron, direct electron-electron and exchange contributions to the total iron atom energy at $B_{12} = 1, 5$. The energies are given in keV.

B_{12}	E_1	E_K	$\langle H_B \rangle$	$\langle V_{en} \rangle$	$\langle V_{ee} \rangle$ direct	$\langle V_{ee} \rangle$ exchange
1	0.12	−7.23	10.6	−95.4	32.7	−3.06
5	0.25	−13.86	19.78	−181.7	61.3	−5.41

Table 3

The single particle energies of iron atoms at (a) $B_{12} = 1$ and (b) $B_{12} = 5$, and their various components: kinetic, nuclear-electron, direct electron-electron, and exchange. The energies are given in keV.

(a) $B_{12} = 1$

m	ν	$\epsilon_{m\nu}$	$\langle h_B \rangle$	$\langle v_{en} \rangle$	$\langle v_{ee} \rangle$ direct	$\langle v_{ee} \rangle$ exchange
0	0	−7.23	1.79	−12.1	3.45	−0.427
0	1	−1.38	1.78	−5.95	3.06	−0.277
1	0	−3.60	0.810	−7.30	3.28	−0.387
1	1	−0.678	1.01	−4.24	2.79	−0.242
2	0	−2.36	0.535	−5.68	3.14	−0.358
2	1	−0.392	0.677	−3.42	2.57	−0.216
3	0	−1.71	0.399	−4.80	3.02	−0.333
3	1	−0.241	0.481	−2.89	2.36	−0.191
4	0	−1.31	0.317	−4.23	2.91	−0.312
4	1	−0.148	0.347	−2.48	2.15	−0.163
5	0	−1.04	0.262	−3.83	2.81	−0.290
5	1	−0.082	0.244	−2.12	1.92	−0.128
6	0	−0.839	0.227	−3.52	2.72	−0.268
7	0	−0.692	0.197	−3.27	2.64	−0.251
8	0	−0.582	0.171	−3.07	2.56	−0.238
9	0	−0.497	0.151	−2.90	2.48	−0.228
10	0	−0.430	0.134	−2.75	2.40	−0.219
11	0	−0.377	0.119	−2.62	2.33	−0.211
12	0	−0.334	0.107	−2.50	2.27	−0.203
13	0	−0.298	0.096	−2.40	2.20	−0.195
14	0	−0.268	0.088	−2.31	2.14	−0.187
15	0	−0.243	0.080	−2.23	2.08	−0.179
16	0	−0.219	0.073	−2.15	2.03	−0.169
17	0	−0.197	0.066	−2.08	1.97	−0.157
18	0	−0.174	0.059	−2.01	1.92	−0.142
19	0	−0.142	0.052	−1.94	1.86	−0.116

(*b*) $B_{12} = 5$

m	ν	$\epsilon_{m\nu}$	$\langle h_b \rangle$	$\langle v_{en} \rangle$	$\langle v_{ee} \rangle$ direct	$\langle v_{ee} \rangle$ exchange
0	0	−13.9	4.24	−23.9	6.58	−0.809
0	1	−0.987	2.55	−8.22	5.08	−0.397
1	0	−7.23	2.09	−14.9	6.27	−0.708
1	1	−0.417	1.43	−5.97	4.43	−0.302
2	0	−4.87	1.45	−11.7	6.03	−0.622
3	0	−3.62	1.11	−9.99	5.83	−0.571
4	0	−2.83	0.901	−8.84	5.64	−0.535
5	0	−2.29	0.753	−8.01	5.47	−0.506
6	0	−1.89	0.643	−7.36	5.31	−0.483
7	0	−1.59	0.558	−6.85	5.16	−0.463
8	0	−1.36	0.490	−6.43	5.02	−0.445
9	0	−1.17	0.435	−6.07	4.89	−0.428
10	0	−1.02	0.389	−5.76	4.77	−0.414
11	0	−0.897	0.350	−5.49	4.64	−0.400
12	0	−0.795	0.316	−5.25	4.53	−0.387
13	0	−0.710	0.288	−5.04	4.42	−0.375
14	0	−0.638	0.263	−4.85	4.31	−0.363
15	0	−0.578	0.242	−4.68	4.21	−0.352
16	0	−0.527	0.223	−4.52	4.11	−0.341
17	0	−0.482	0.206	−4.38	4.02	−0.330
18	0	−0.443	0.191	−4.25	3.93	−0.318
19	0	−0.408	0.177	−4.12	3.84	−0.305
20	0	−0.375	0.165	−4.01	3.76	−0.290
21	0	−0.342	0.152	−3.89	3.67	−0.271
22	0	−0.306	0.139	−3.78	3.58	−0.246
23	0	−0.255	0.124	−3.66	3.48	−0.203

Table 4

Absolute values of the ground-state energies of all atoms through $Z = 18$, for $B_{12} = 0.1, 0.5, 1$, and 5. The energies are given in keV. For the heavier atoms, calculations were done only for large fields, where the adiabatic assumption is valid.

Z \ β_{12}	0.1	0.5	1.0	5.0
1	0.0761	0.130	0.161	0.2550
2	0.255	0.454	0.574	0.9580
3	0.516	0.944	1.209	2.0760
4	0.846	1.580	2.042	3.5840
5	1.238	2.347	3.054	5.4560
6	1.678	3.22	4.20	7.60
7	2.17	4.22	5.54	10.20
8	2.71	5.32	7.02	13.00
9	3.36	6.51	8.63	16.10
10		7.819	10.39	19.57
11		9.197	12.25	24.64
12		10.72	14.23	27.17
13		12.32	16.34	31.35
14		14.00	18.60	35.74
15		15.79	20.95	40.35
16		17.67	23.43	45.22
17		19.64	26.07	50.30
18		21.72	28.82	55.95

Table 5

The number of occupied one-node states at the ground state for all atoms with $Z \leq 18$ and for iron, at various field strengths.

Z \ B_{12}	0.1	0.5	1.0	5.0
1–9	0	0	0	0
10		0	0	0
11		0	0	0
12		1	0	0
13		1	1	0
14		1	1	0
15		2	1	0
16		2	2	0
17		2	2	0
18		3	2	0
26			6	2

Figure 1

Conjectured phase diagram of nuclear matter; taken from Ref. 46 (Part 1). We added a sketch of the regions of the (ρ, T) plane which are probed by (a) monopole excitations, (b) supernova calculations, and (c) heavy ion reactions.

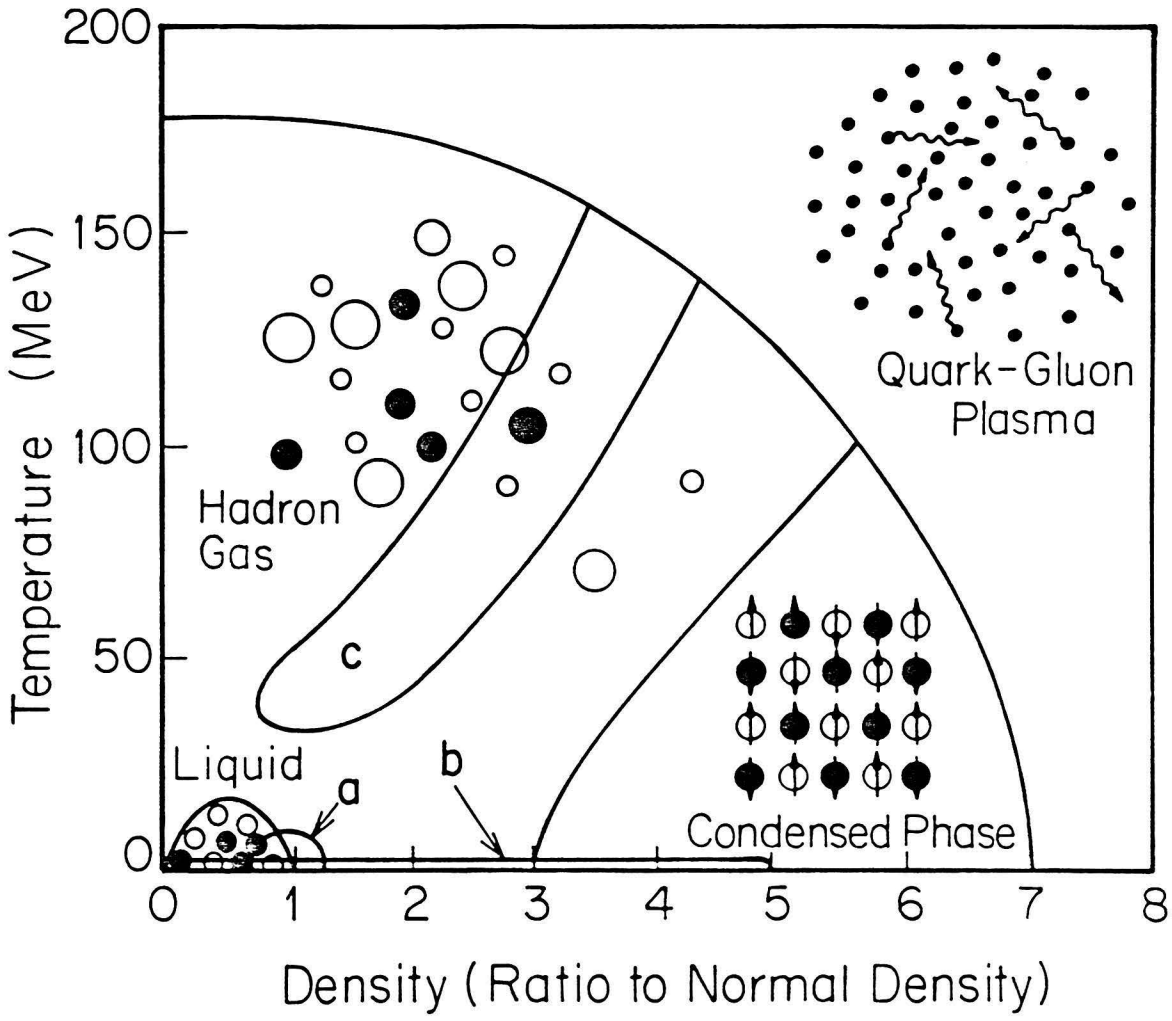
200
150
100
50
0
Temperature (MeV)
Quark-Gluon
Plasma
Hadron
Gas
c
Liquid
a
b
Condensed Phase
0
1
2
3
4
5
6
7
8
Density (Ratio to Normal Density)

Figure 2

Schematic diagram of the various stages of a heavy ion collision; the nuclei touch and interpenetrate (a), the pressure stops the nuclei and a hot dense piece of nuclear matter forms (b), the combined system expands (c), and breaks into fragments (d).

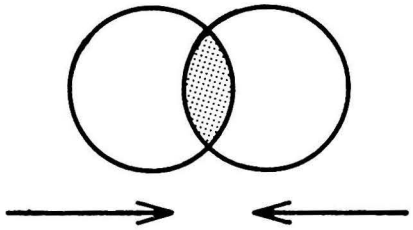

a

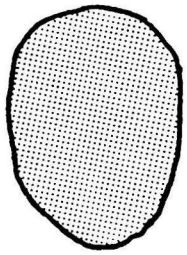

b

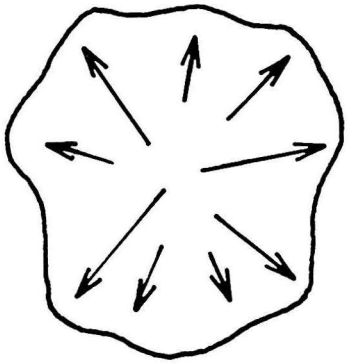

c

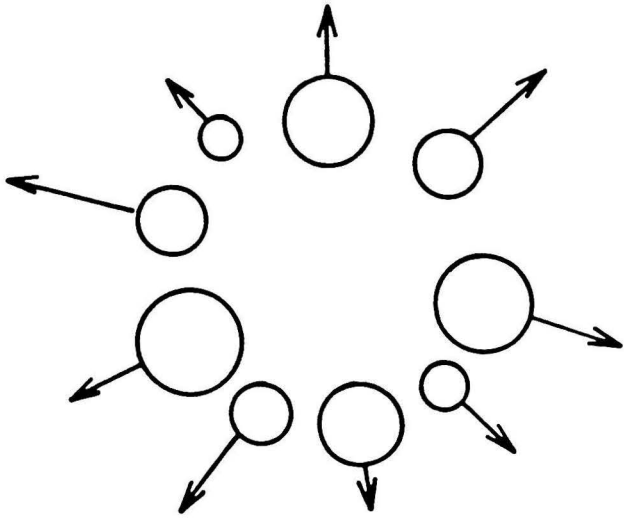

d

Figure 3

The evolution of the density contours as a function of the impact parameter, in a Nuclear Fluid Dynamics calculation of the system Ar+Ca at 400 MeV/A. Taken from Ref. 5 (Part 1.). We also draw explicitly the flow angle, θ_f.

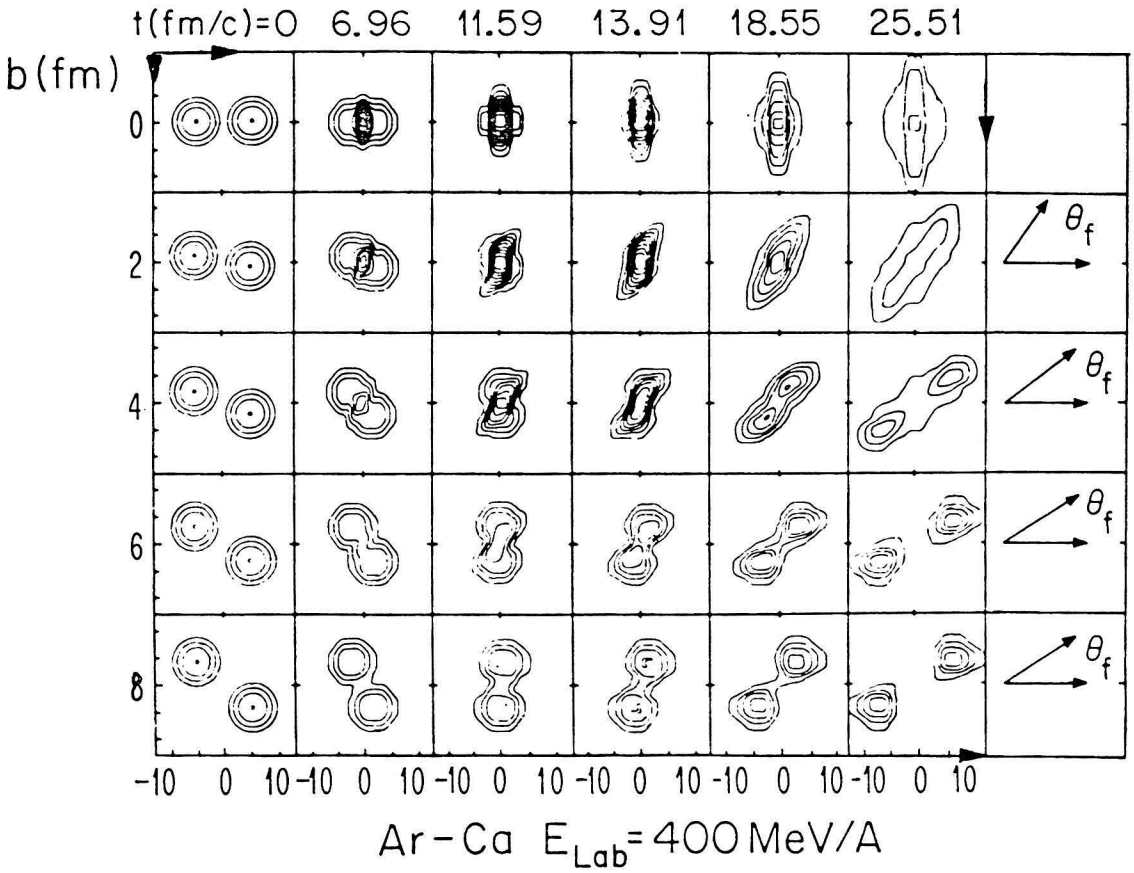
t(fm/c)=0 6.96 11.59 13.91 18.55 25.51
b(fm)
0
2
4
6
8
θ_f
-10 0 10 -10 0 10 -10 0 10 -10 0 10 -10 0 10 -10 0 10
Ar-Ca E_{Lab}=400 MeV/A

Figure 4

The participant-spectator model of heavy ion collisions. The participant fragment is heated up by the collision; the spectator fragments leave the collision with their original velocity and with relatively low temperature. Taken from Ref. 47 (Part 1).

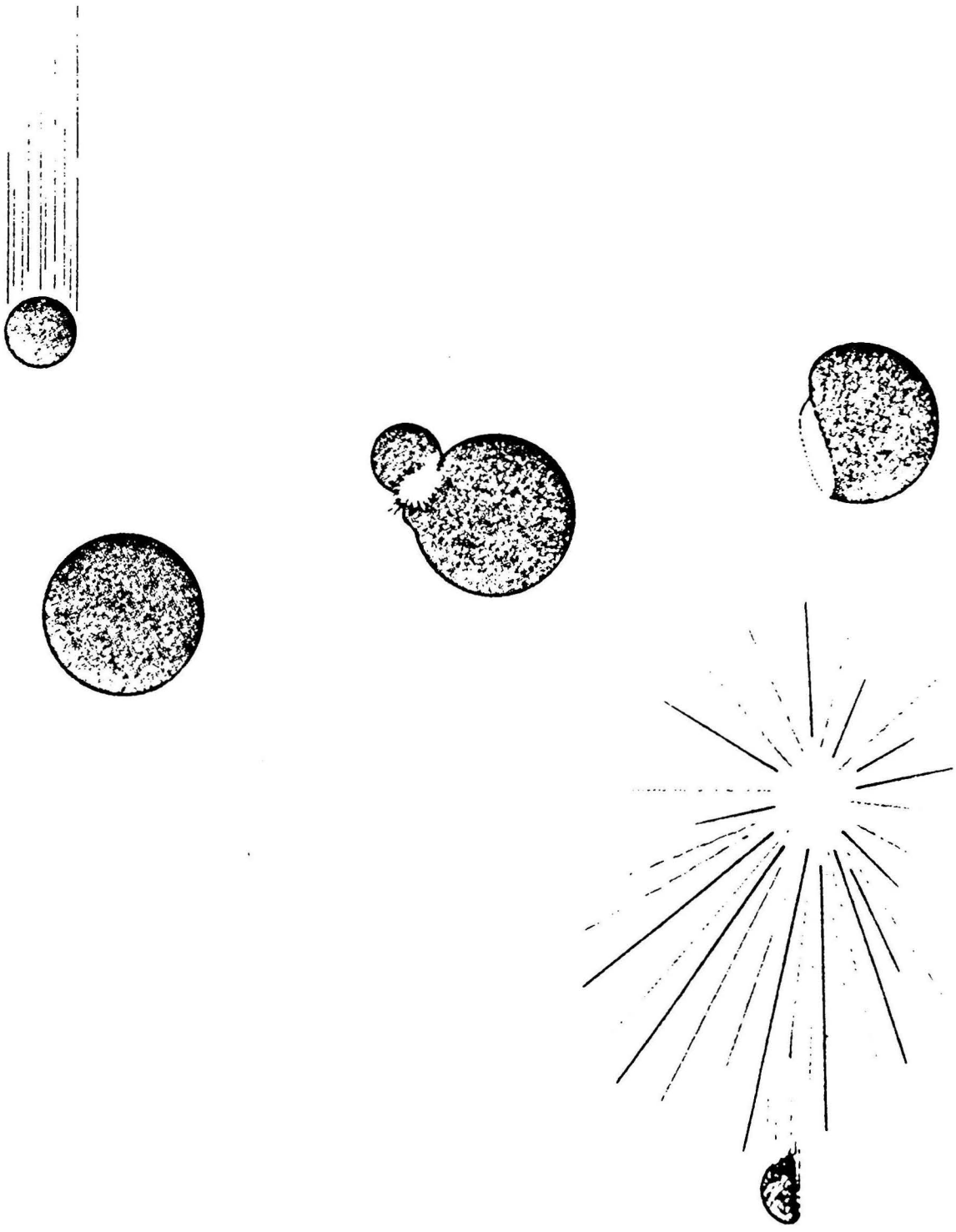

Figure 5

Data on photon emission cross sections for the systems (*a*) C+Pb at 40 MeV/A and (*b*) C+U at 84 MeV/A. Taken from Refs. 24 and 23 (Part 1).

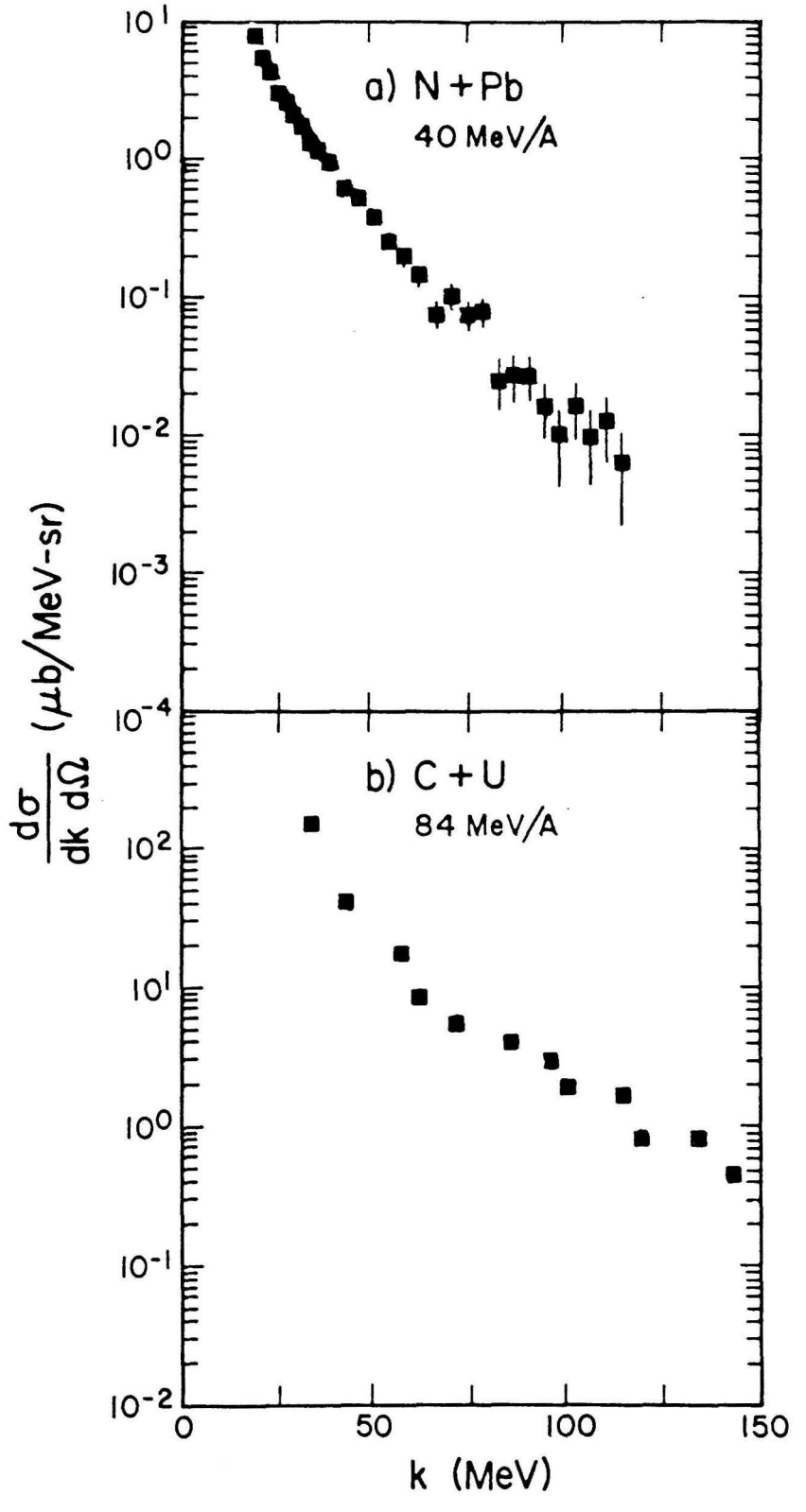
a) N + Pb
40 MeV/A
b) C + U
84 MeV/A
dσ/dk dΩ (μb/MeV-sr)
k (MeV)
10^1
10^0
10^-1
10^-2
10^-3
10^-4
10^2
0
50
100
150

Figure 6

Schematic pictures of Nucleon-nucleon scattering: (a) elastic collision, and (b) bremsstrahlung process. The strong interaction scattering matrix is represented by a thick blob. Bremsstrahlung processes probe the off-shell elements of the scattering matrix, in contrast to elastic collision.

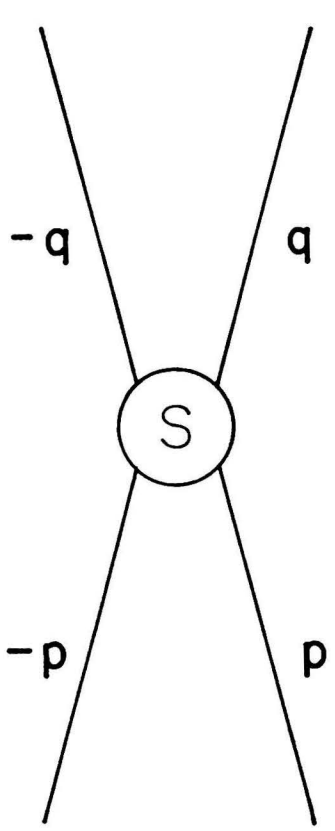

$|q| = |p|$

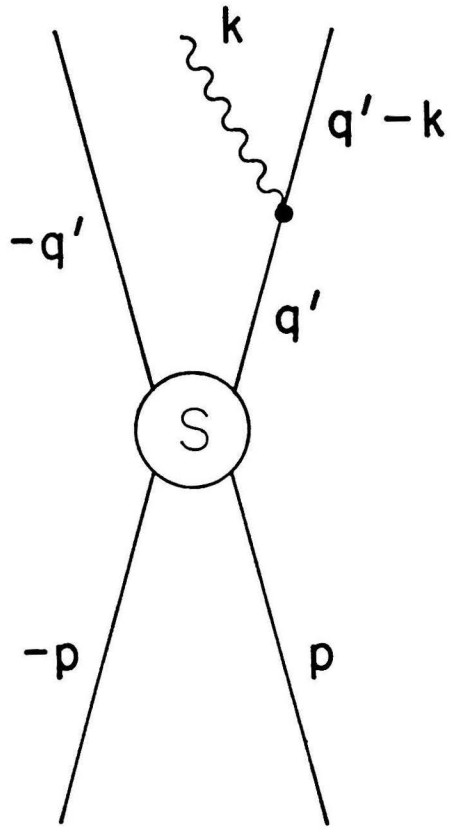

$|q'| < |p|$

Figure 7

Photon production cross sections for neutron-proton collisions in free space. Quantal (solid lines), classical (dashed lines), and modified classical calculations (dash-dotted lines) are shown as functions of the outgoing photon energy for center-of mass collision energies of (a) 50 MeV, and (b) 200 MeV.

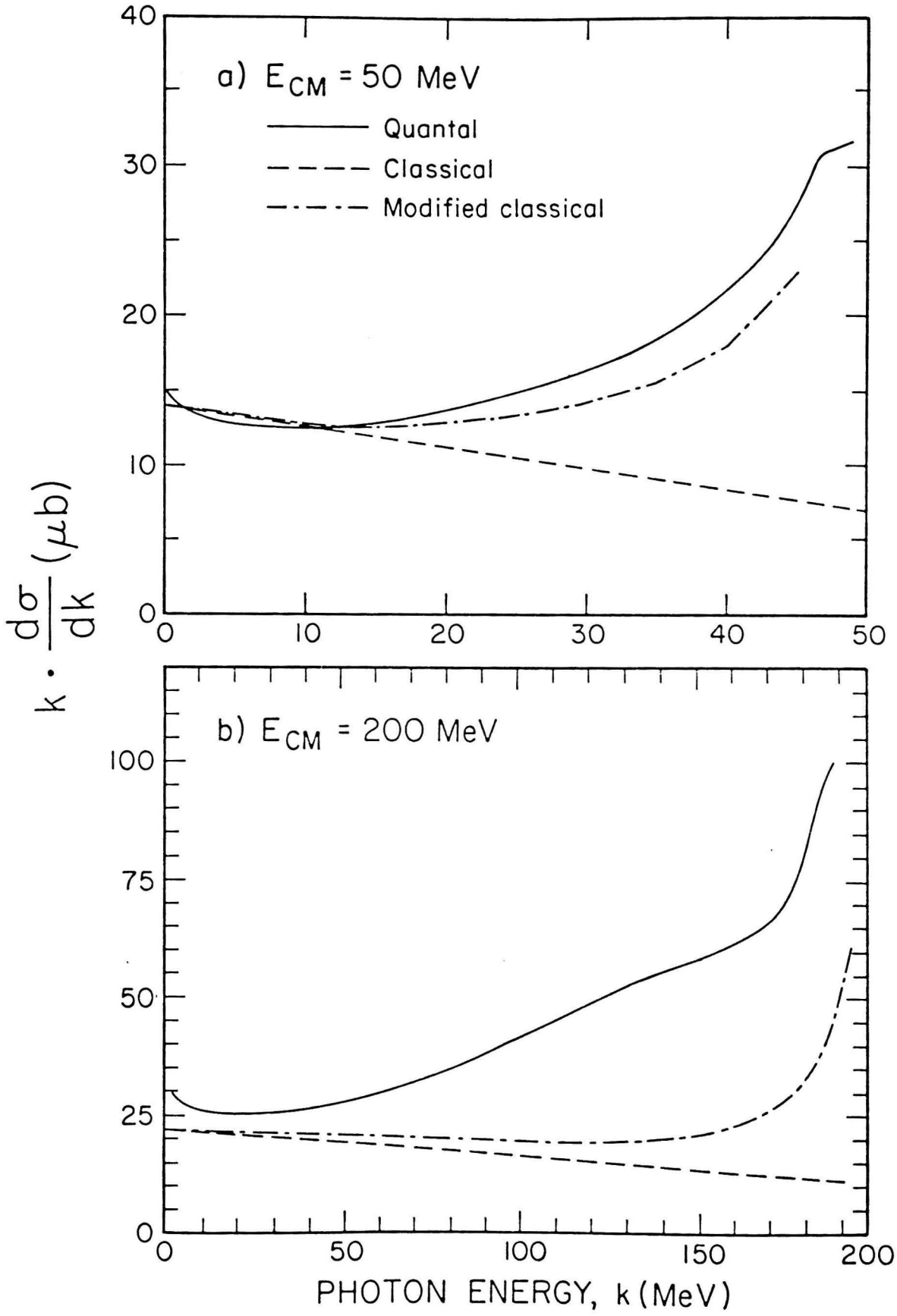
a) E_{CM} = 50 MeV
Quantal
Classical
Modified classical
b) E_{CM} = 200 MeV
$k \cdot \frac{d\sigma}{dk}$ (μb)
PHOTON ENERGY, k (MeV)
0
10
20
30
40
50
0
25
50
75
100
150
200

Figure 8

The photon emission rate from nuclear matter in thermal equilibrium at equilibrium density $n = 0.15$ fm^{-3} is shown for various temperatures. The number near each curve labels the temperature in MeV.

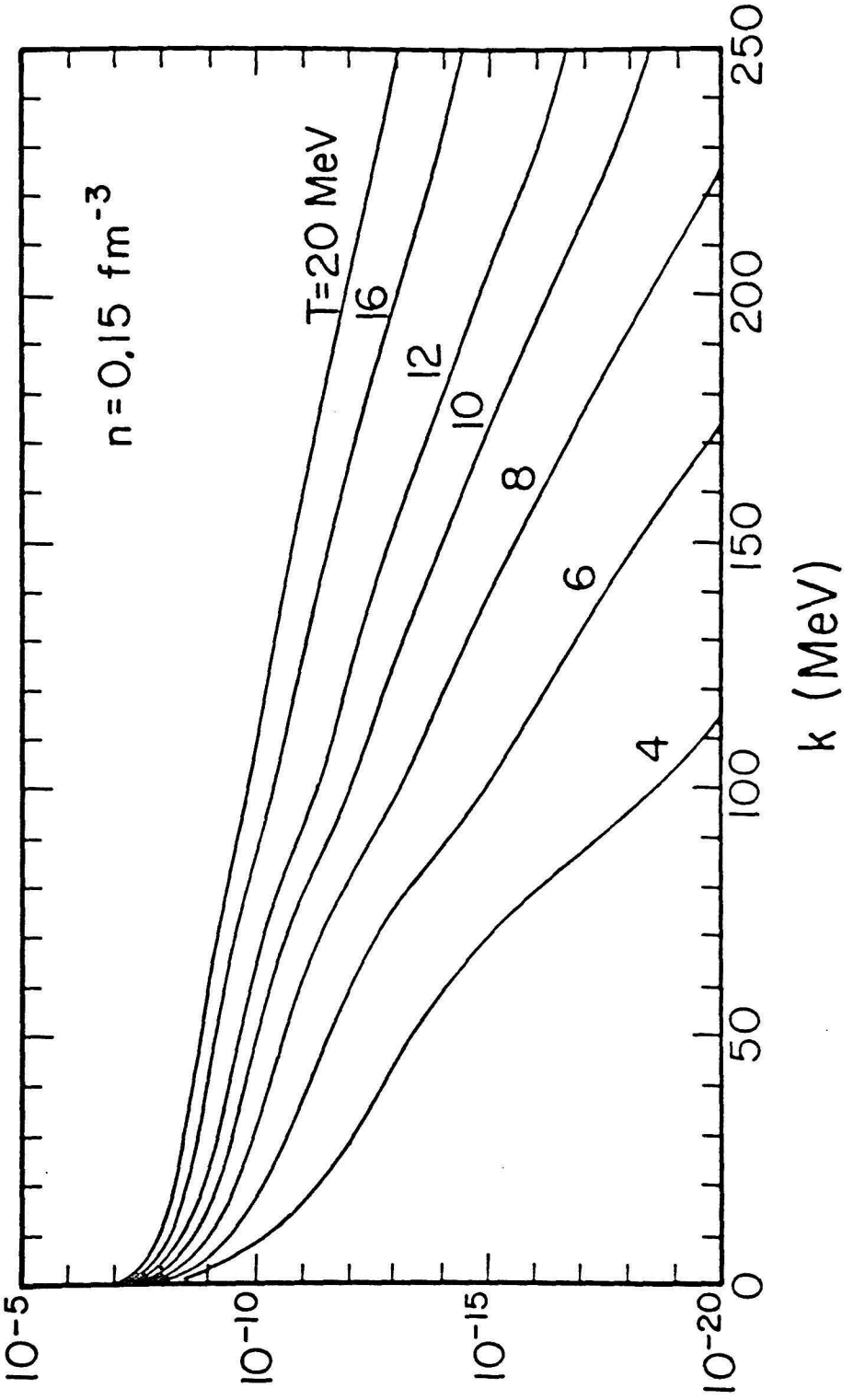
n=0.15 fm^{-3}
T=20 MeV
16
12
10
8
6
4
10^{-5}
10^{-10}
10^{-15}
10^{-20}
0
50
100
150
200
250
k (MeV)
$d^7N/d^4x\ dk\ d\Omega$
$((fm/c)^{-1}\ fm^{-3}\ MeV^{-1}\ sr^{-1})$

Figure 9

Ratios of quantal and classical emission rates from nuclear matter in thermal equilibrium, for various temperatures and densities, and for a Boltzman distribution function, ignoring Pauli blocking (labeled "B"). For a Boltzman distribution, the ratios are independent of density.

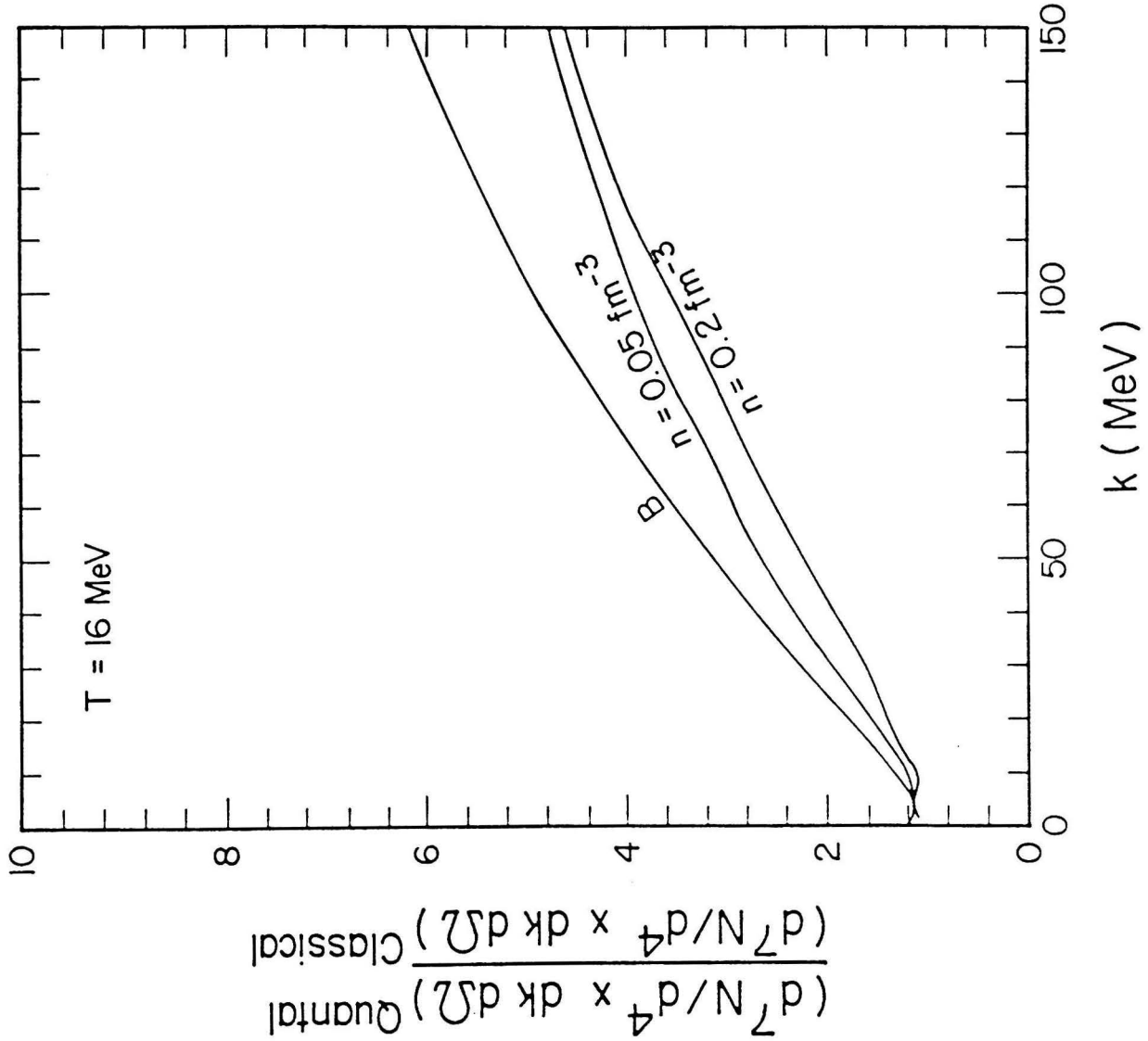
$\frac{(d^7N/d^4x\ dk\ d\Omega)_{Quantal}}{(d^7N/d^4x\ dk\ d\Omega)_{Classical}}$
T = 16 MeV
B
n = 0.05 fm^{-3}
n = 0.2 fm^{-3}
k (MeV)
0
2
4
6
8
10
0
50
100
150

Figure 10

Spectra from the fireball calculations, with (solid line) and without (dashed line) quantum mechanical modification are compared to experimental data (in squares) for the systems (*a*) C+Pb at 40 MeV/A and (*b*) C+U at 84 MeV/A. The data are redrawn from Figure 5.

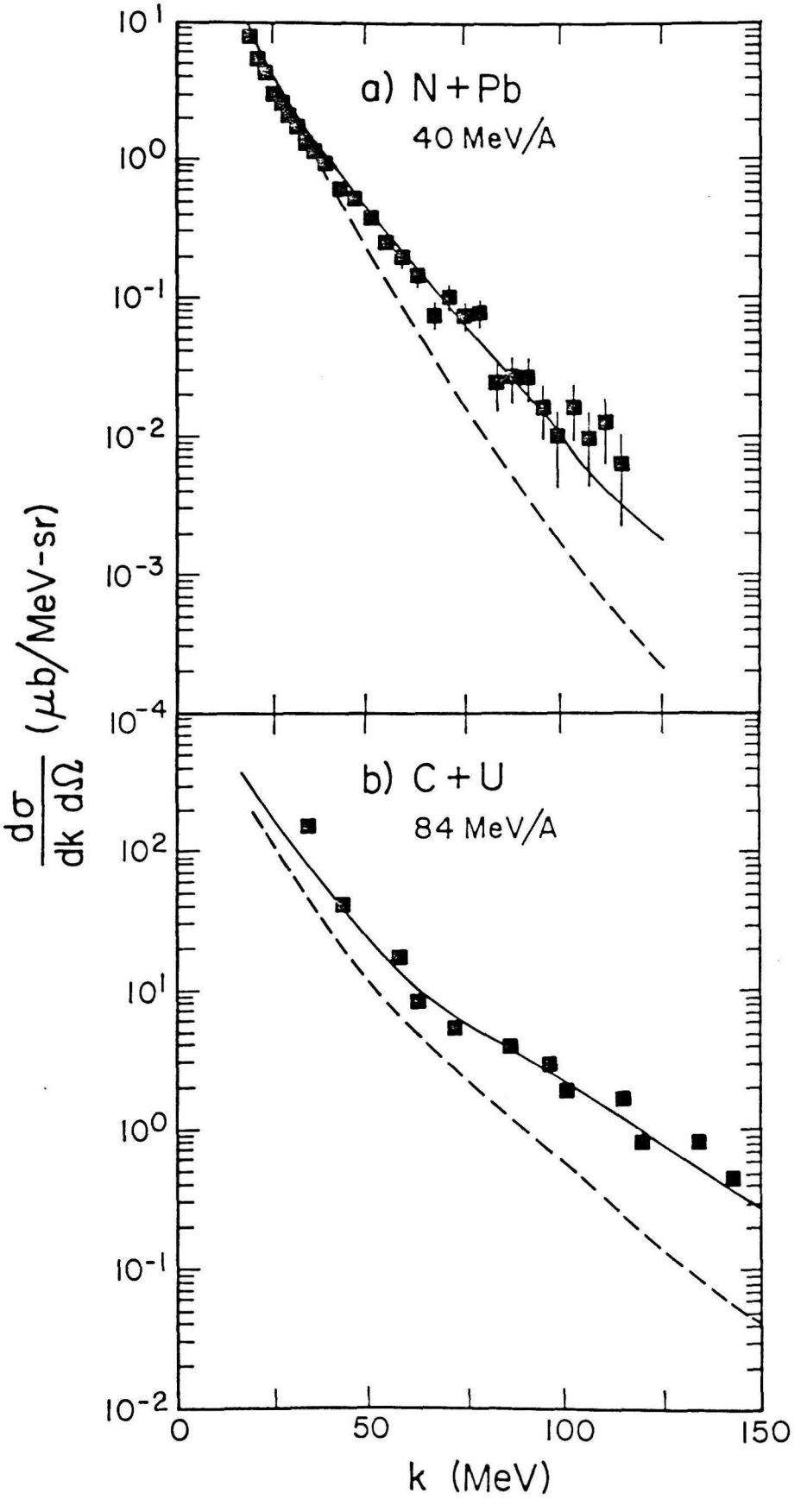
a) N + Pb
40 MeV/A
b) C + U
84 MeV/A
$\frac{d\sigma}{dk\, d\Omega}$ (μb/MeV-sr)
k (MeV)
10^{1}
10^{0}
10^{-1}
10^{-2}
10^{-3}
10^{-4}
10^{2}
10^{1}
10^{0}
10^{-1}
10^{-2}
0
50
100
150

Figure 11

The ensemble approach to the VUU model. Notice that nucleons collide only with nucleons in the same ensemble member. The ensemble provides only global (i.e., ensemble-member independent) Pauli-blocking and mean-field.

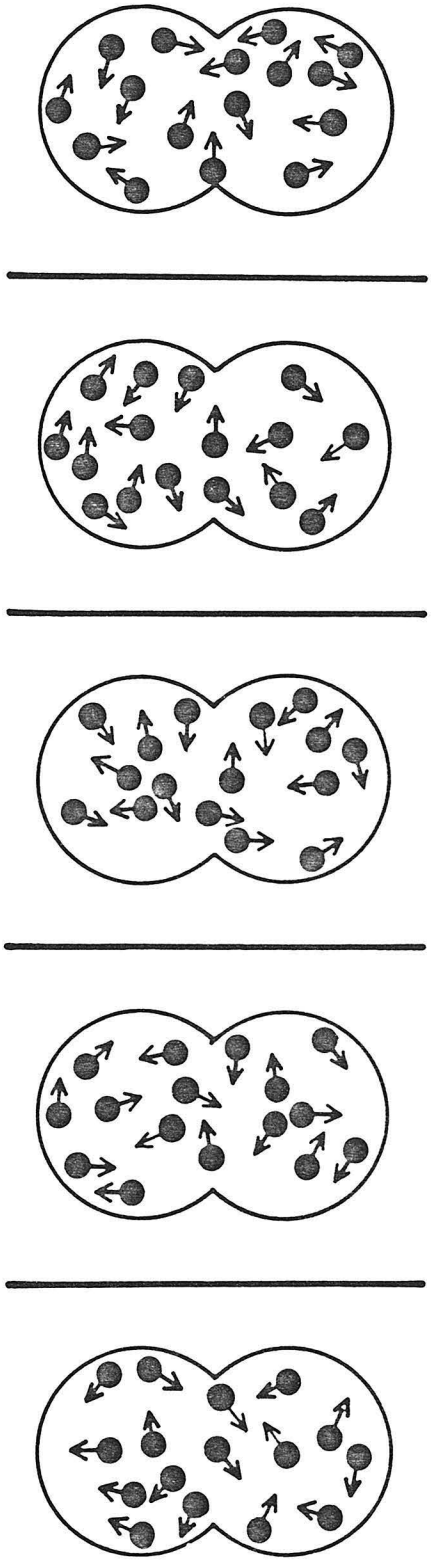

Figure 12

Spectra from VUU calculations with quantum mechanical modifications (solid lines) and phenomenological expressions for nucleon-nucleon bremsstrahlung cross sections (dashed lines) are compared to experimental data (in squares) for the system C+C at (*a*) 40 MeV/A and (*b*) 84 MeV/A. The emission angle of the photons is 90^o at the center of mass of the colliding nuclei. In (a) the data are for N+C reaction; this introduces a minor modification.

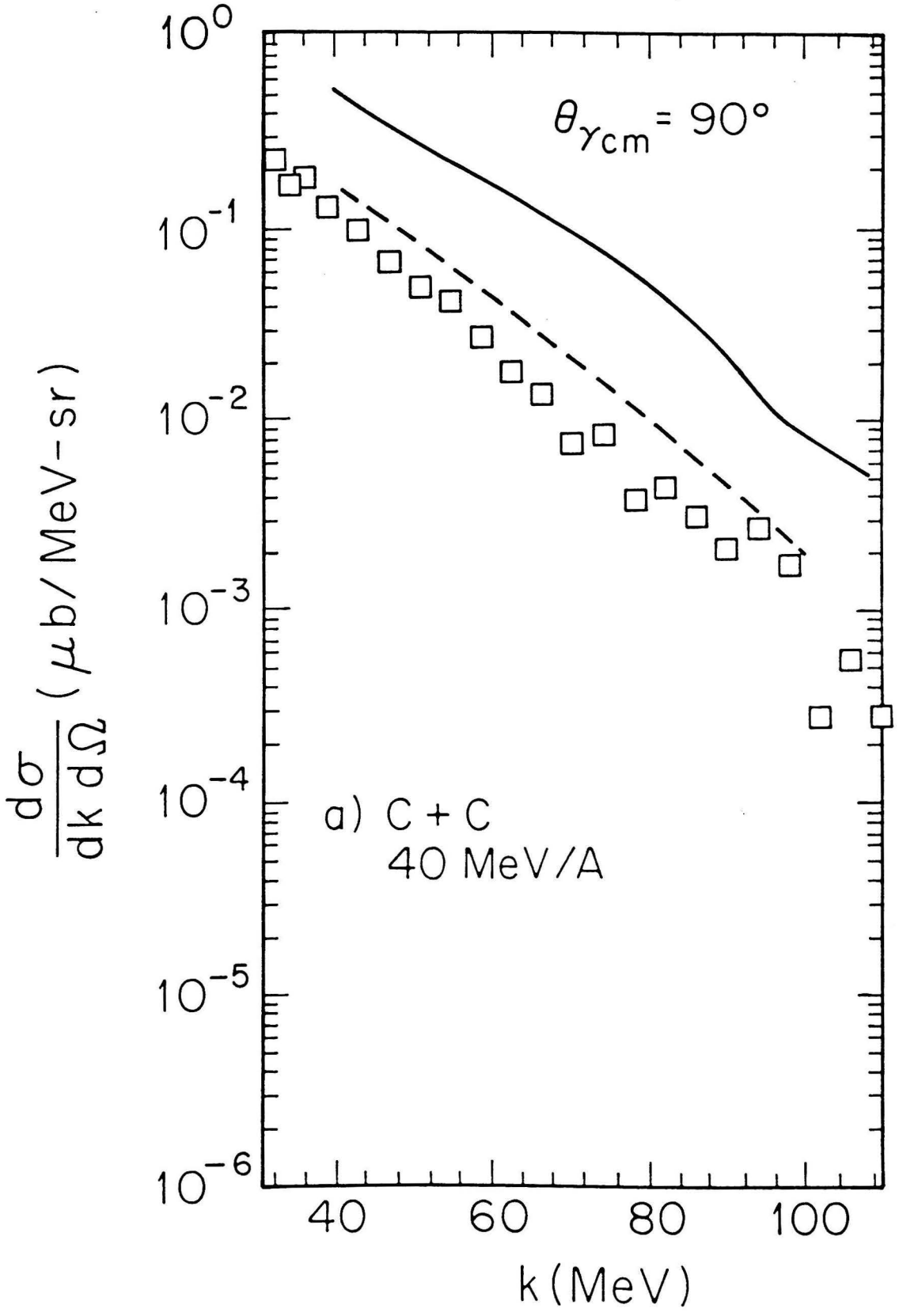
10^0
10^{-1}
10^{-2}
10^{-3}
10^{-4}
10^{-5}
10^{-6}
$\frac{d\sigma}{dk\, d\Omega}$ (μb/ MeV-sr)
$\theta_{\gamma cm}$ = 90°
a) C + C
40 MeV/A
40
60
80
100
k (MeV)

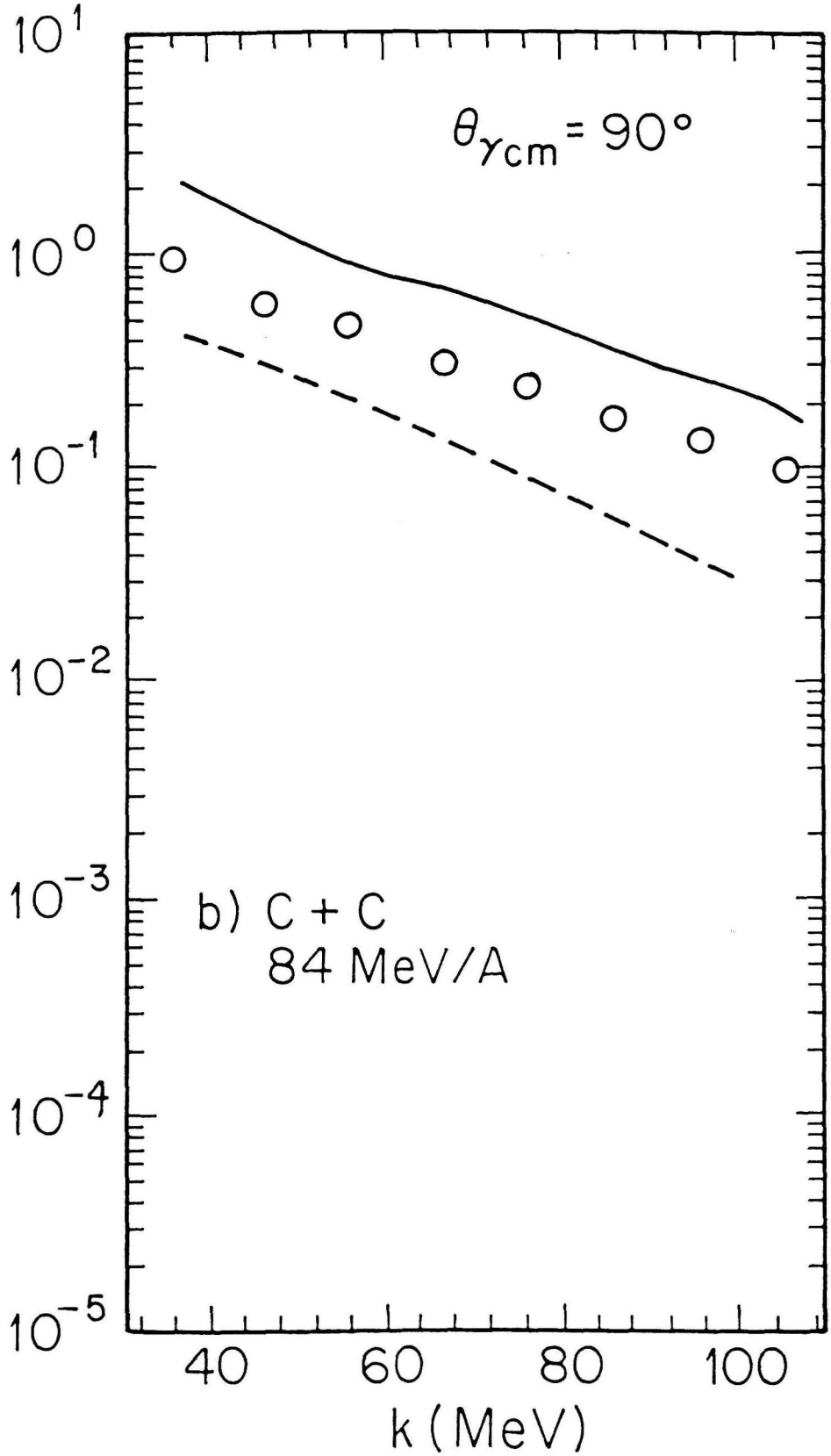
10^{1}
10^{0}
10^{-1}
10^{-2}
10^{-3}
10^{-4}
10^{-5}
$\theta_{\gamma cm} = 90°$
b) C + C
84 MeV/A
40
60
80
100
k (MeV)

Figure 13

Angular emission spectra from VUU calculations using a cross section with quantum mechanical corrections, for the system C+C at 84 MeV/A. The *ad hoc* dipole emission pattern for a nucleon-nucleon collision (Eq. 4.36, Part 1) is partially flattened in the total emission spectra.

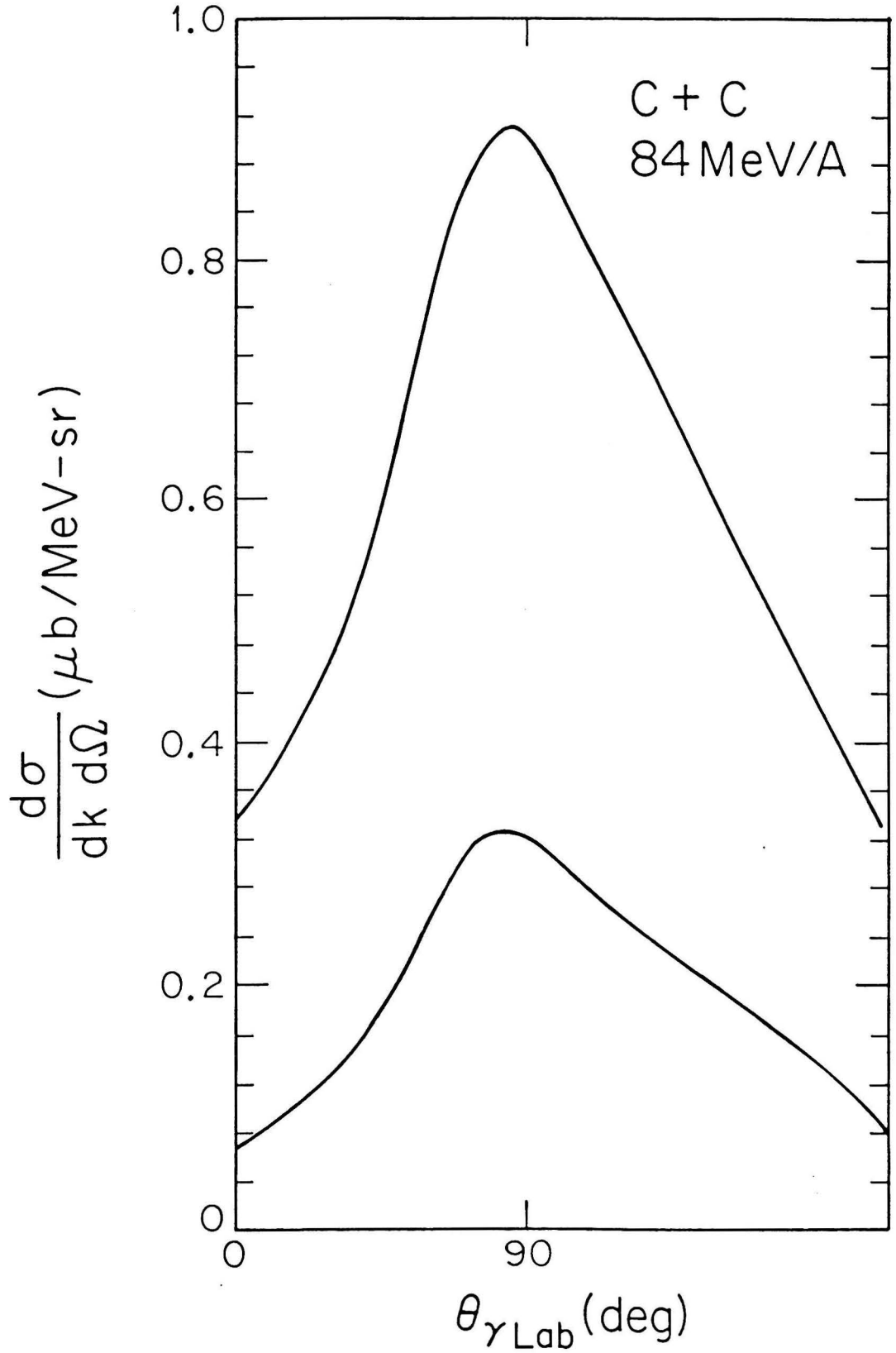
1.0
0.8
0.6
0.4
0.2
0
0
90
C + C
84 MeV/A
$\frac{d\sigma}{dk\, d\Omega}$ (μb/MeV-sr)
$\theta_{\gamma\,Lab}$ (deg)

Figure 14

The temporal evolution of the emission probability of 20, 50, and 100 MeV photons, calculated in the VUU model, for zero impact-parameter collisions of C+C at 40 MeV/A and 100 MeV/A. The photon emission angle is 36° at the Laboratory. The nuclei start at a distance 2 fm apart; their first-touch time, t_{touch}, is indicated on the figure. We also indicated the passage time for the case of no collisions, $4R/v$.

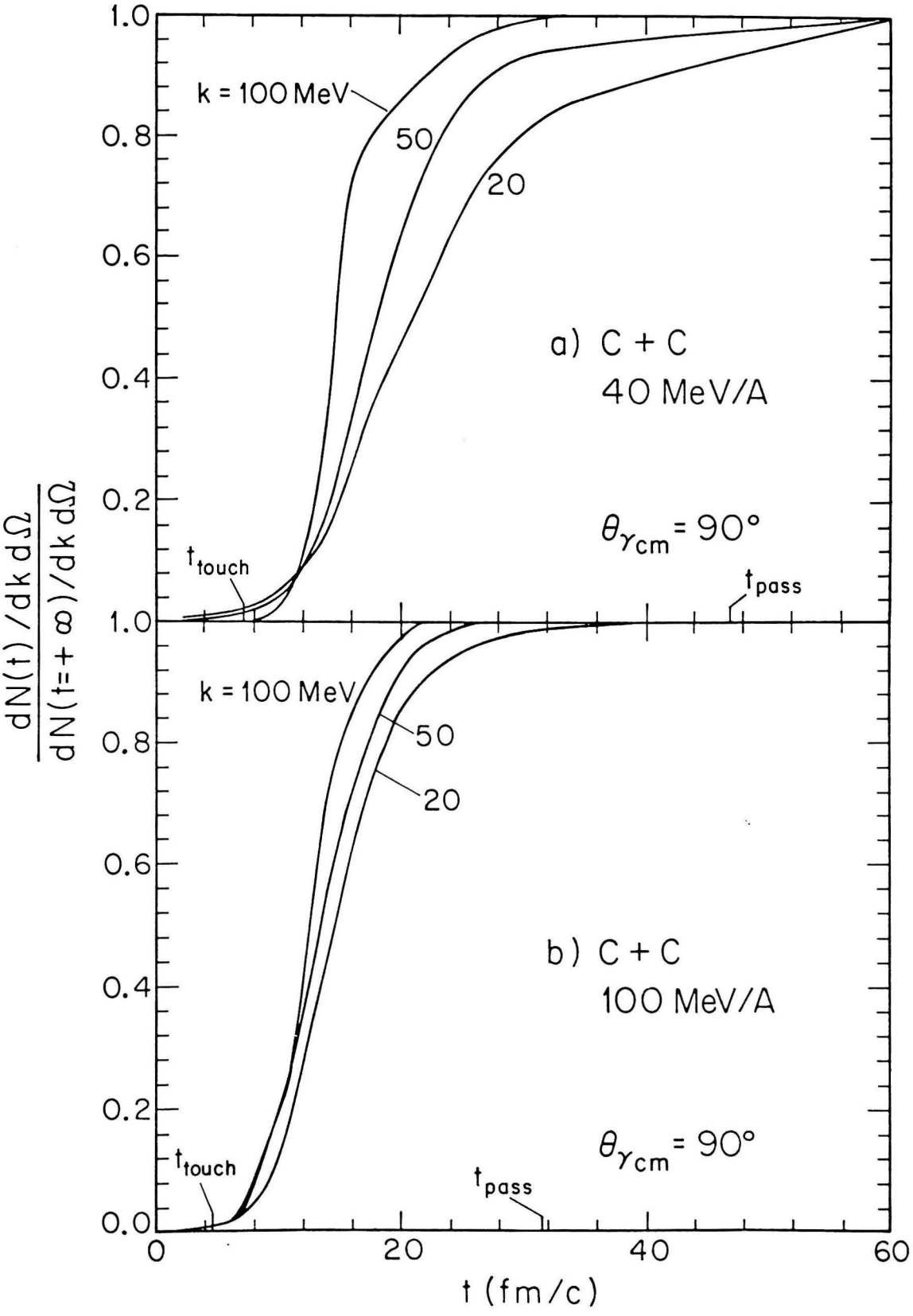
1.0
0.8
0.6
0.4
0.2
1.0
0.8
0.6
0.4
0.2
0.0
k = 100 MeV
50
20
a) C + C
40 MeV/A
$\theta_{\gamma cm}$ = 90°
t_{touch}
t_{pass}
k = 100 MeV
50
20
b) C + C
100 MeV/A
$\theta_{\gamma cm}$ = 90°
t_{touch}
t_{pass}
0
20
40
60
t (fm/c)
$\frac{dN(t)/dk\,d\Omega}{dN(t=+\infty)/dk\,d\Omega}$

Figure 15

The Hanbury-Brown Twiss effect: for identical particles, the amplitude for the process $x_1 \rightarrow r_1$, $x_2 \rightarrow r_2$ (solid lines) is added together with the amplitude for $x_1 \rightarrow r_2$, $x_2 \rightarrow r_1$ (dashed lines). Taken from Ref. 40, Part 1.

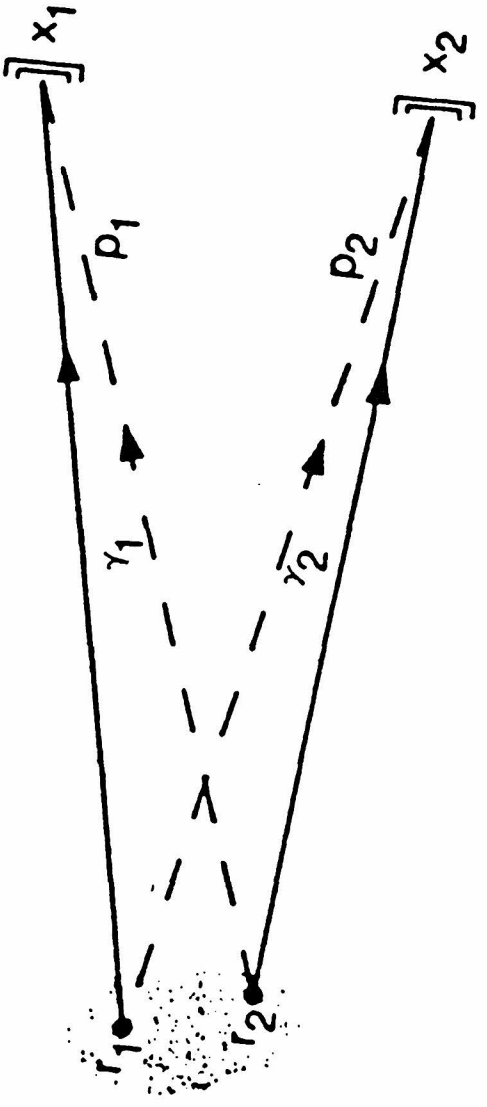
x1
x2
p1
p2
γ1
γ2
r1
r2

Figure 16

The correlation functions for parallel photons emitted from a Gaussian source are shown as functions of the photon energy difference, for several values of k, R, τ.

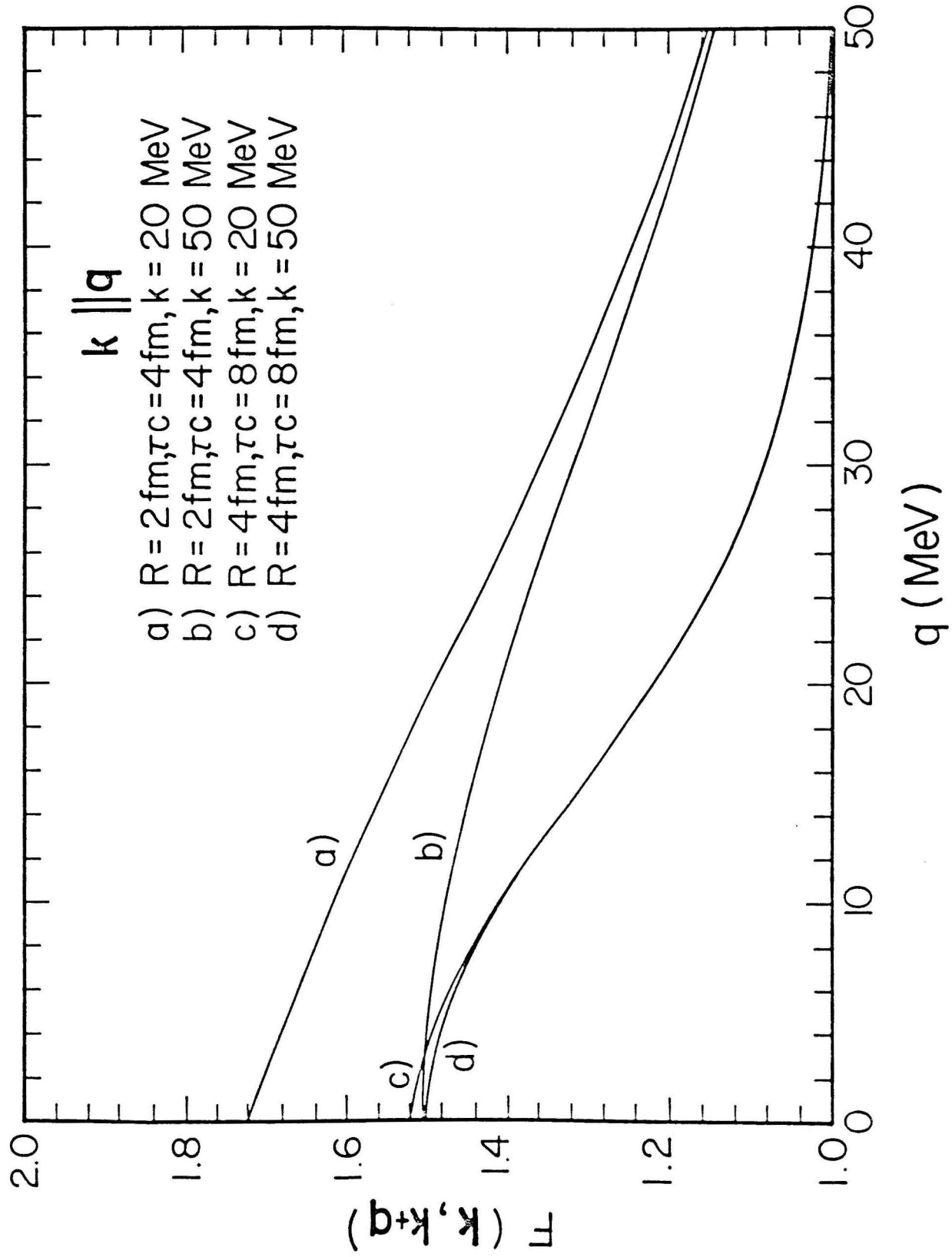
k ||q
a) R=2fm,rc=4fm,k=20 MeV
b) R=2fm,rc=4fm,k=50 MeV
c) R=4fm,rc=8fm,k=20 MeV
d) R=4fm,rc=8fm,k=50 MeV
a)
b)
c)
d)
Γ (k, k+q)
q (MeV)
2.0
1.8
1.6
1.4
1.2
1.0
0
10
20
30
40
50

Figure 17

The correlation functions for equal-energy photons are shown as functions of the relative angle between the photons, for the same sets of k, R, τ, shown in Fig. 16.

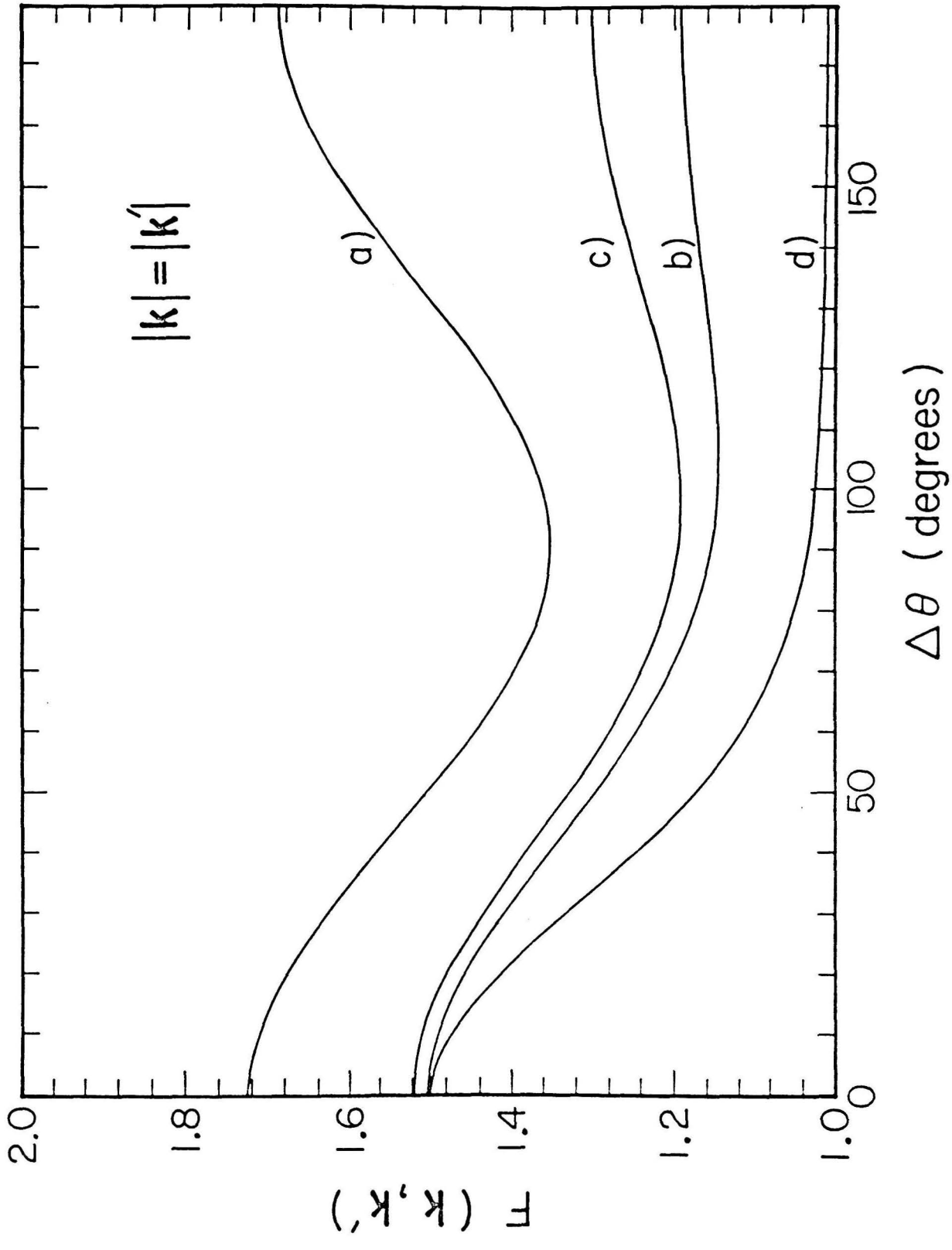
|k| = |k'|
a)
c)
b)
d)
Γ (k, k')
Δθ (degrees)
2.0
1.8
1.6
1.4
1.2
1.0
0
50
100
150

Figure 18

The correlation functions for equal-energy photons with (dashed line) and without (solid line), a coherent component of the same magnitude as the incoherent current ($|j_c(k)|^2 = P_\gamma(k)$), are shown as functions of the relative angle between the photons. One photon is held fixed at a polar angle of 45^o, and the other is varied in the plane defined by the z axis and the first photon. The Gaussian-source parameters are $R = 2$ fm and $\tau = 4$ fm/c, and the photon energy is 50 MeV.

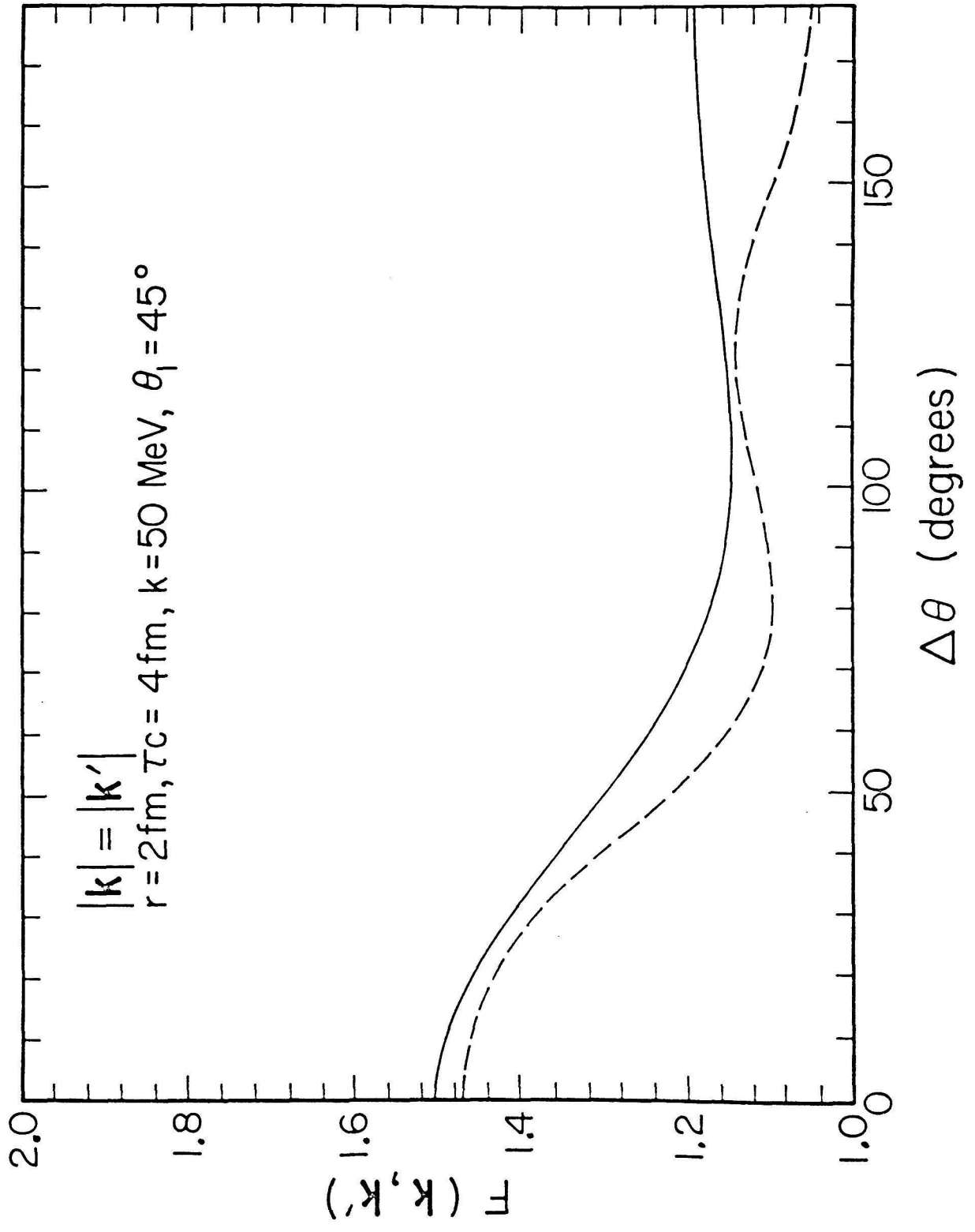
|k| = |k'|
r=2fm, τc= 4fm, k=50 MeV, θ1=45°
T (k, k')
Δθ (degrees)
2.0
1.8
1.6
1.4
1.2
1.0
0
50
100
150

Figure 19

Qualitative picture of hydrogen in very strong magnetic fields.

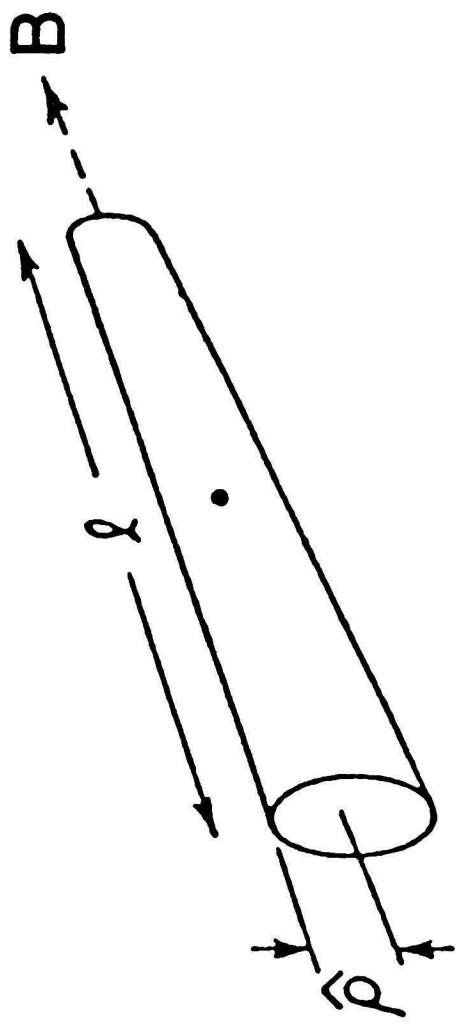
B
l
r

Figure 20

The ground-state energies per unit cell of infinite linear chains of helium (a), carbon (b) and iron (c) are shown as functions of the internuclear separation, for $B_{12} = 1$ (dashed lines) and 5 (solid lines). The energies are relative to the isolated atom values. The unit of length is $2.566 \times 10^{-10}\,\mathrm{cm} \times B_{12}^{-1/2}$.

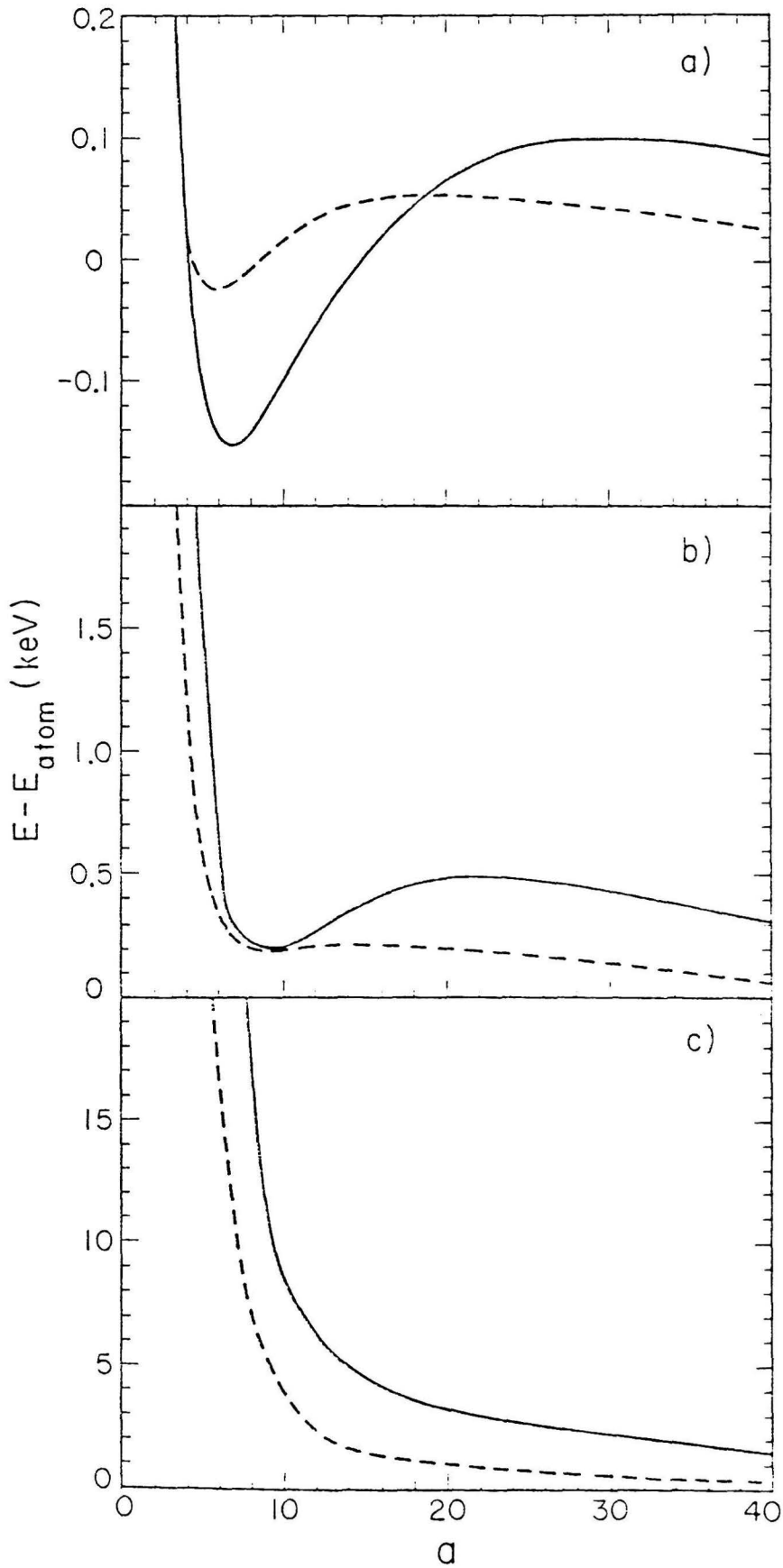
a)
b)
c)
0.2
0.1
0
-0.1
1.5
1.0
0.5
0
15
10
5
0
0
10
20
30
40
a
E-E_atom (keV)

Figure 21

The Fermi energies (dot-dashed lines) and the single-particle energies of electrons in zero-node states (solid lines), one-node states (dashed lines), and two-node states (dotted lines), for infinite linear chains of helium (a), carbon (b), and iron (c, d). The energies are shown as functions of the internuclear separation, for all occupied orbitals at $B_{12} = 1$. (d) is the same as (c), except that it uses a finer scale, to show clearly the energies of the upper orbitals. The unit of length is the same as in Figure 20.

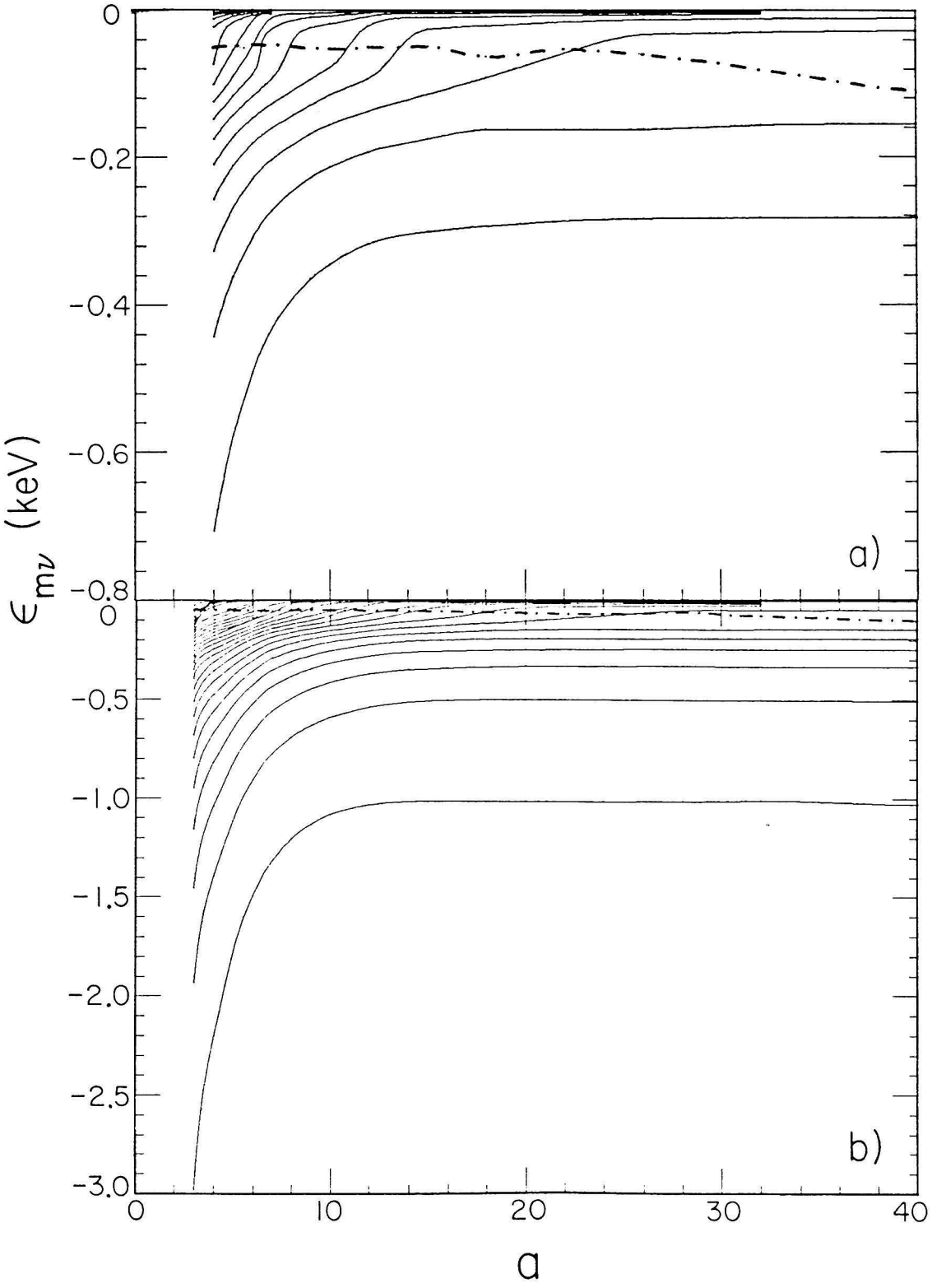
0
-0.2
-0.4
-0.6
-0.8
a)
0
-0.5
-1.0
-1.5
-2.0
-2.5
-3.0
b)
$\epsilon_{m\nu}$ (keV)
0
10
20
30
40
a

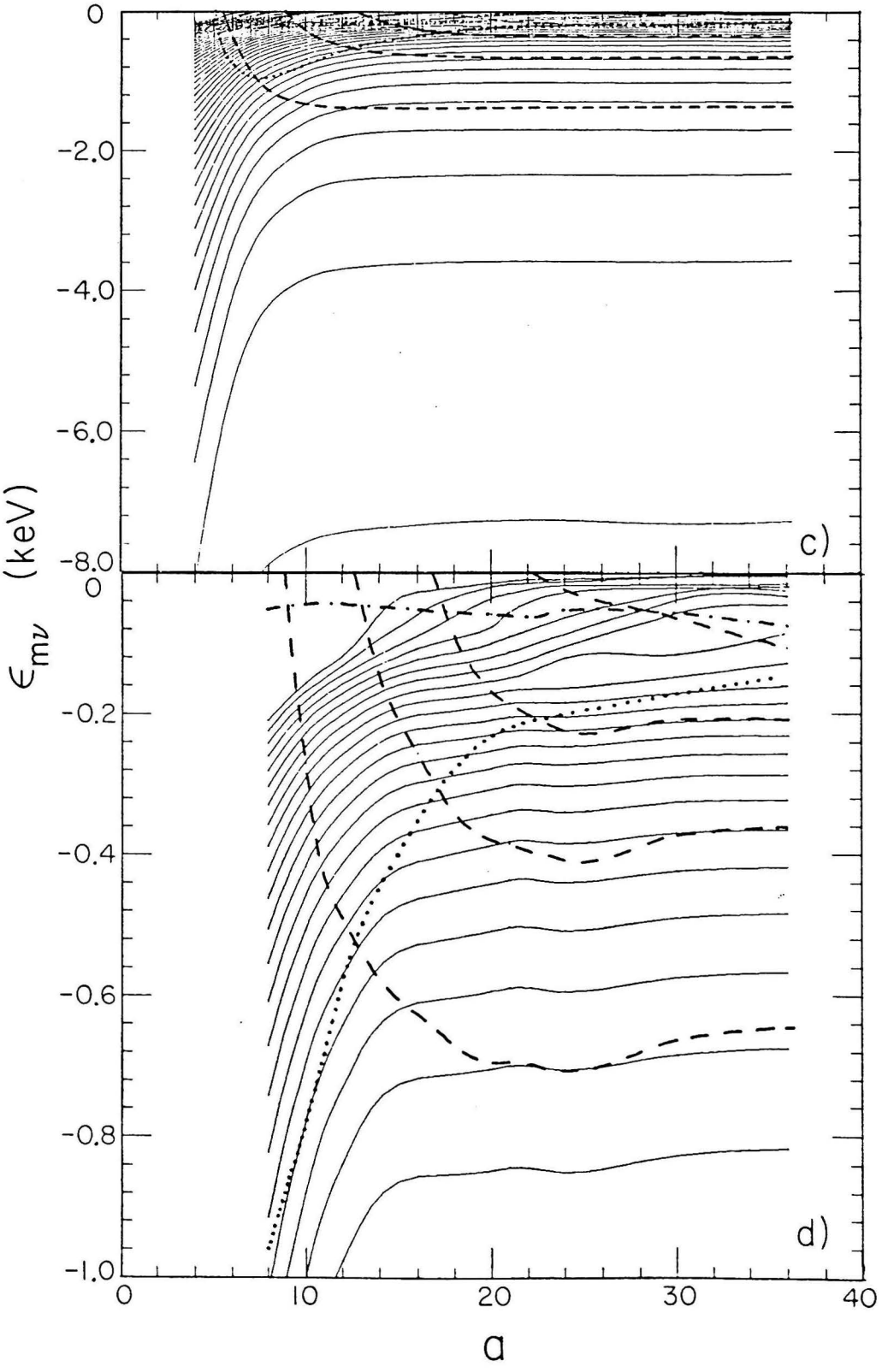
0
-2.0
-4.0
-6.0
-8.0
c)
$\epsilon_{m\nu}$ (keV)
0
-0.2
-0.4
-0.6
-0.8
-1.0
d)
0
10
20
30
40
a

Figure 22

The binding energies of isolated atoms in strong fields are shown as functions of Z, for $B_{12} = 0.1$,0.5,1, and 5. The energies are scaled by $B_{12}^{-2/5}$, and logarithmic scales are used, to show clearly the $Z^{7/8}B^{2/5}$ dependence.

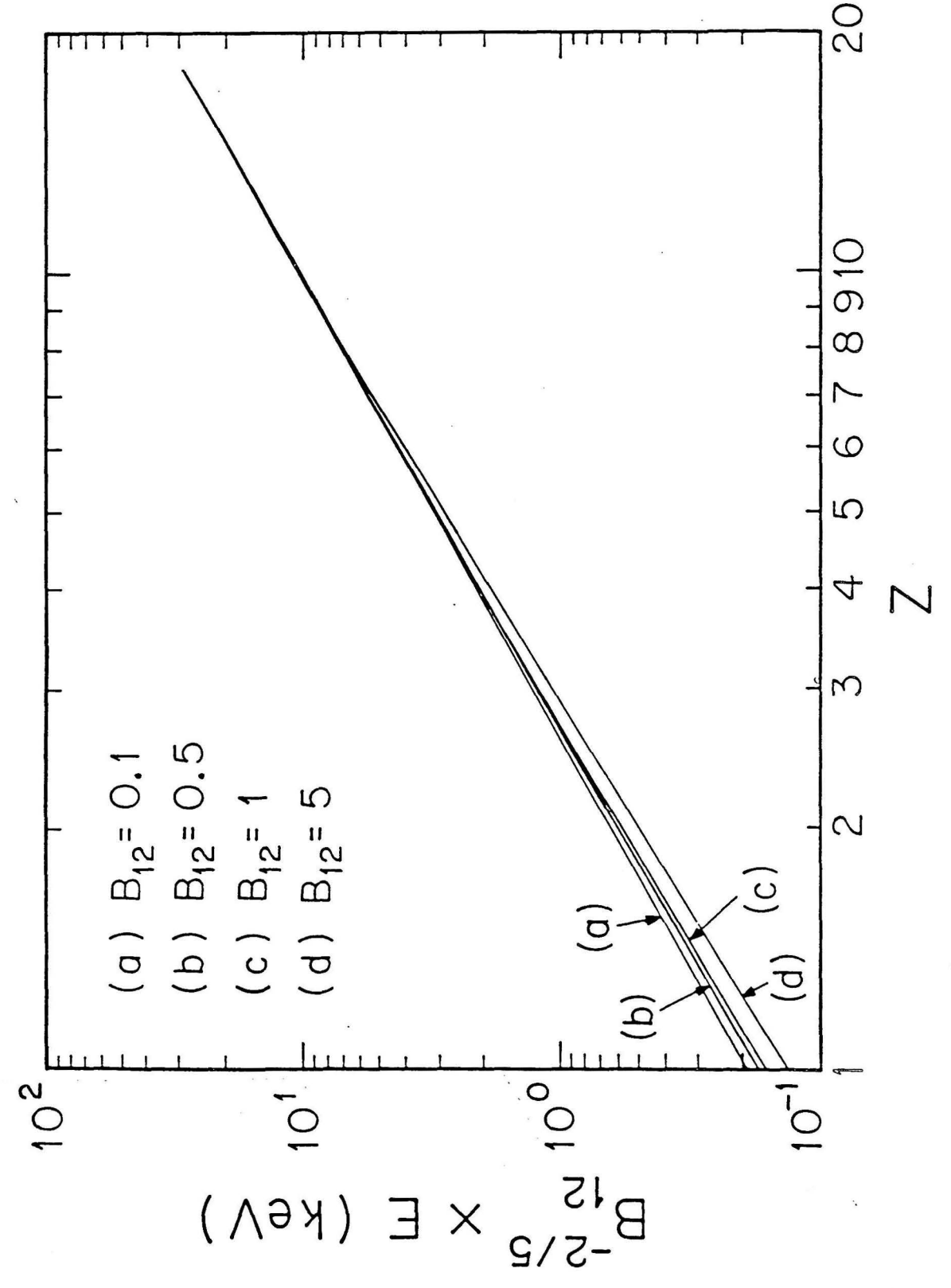
$B_{12}^{-2/5} \times E$ (keV)
10^2
10^1
10^0
10^{-1}
1
2
3
4
5
6
7
8
9
10
20
Z
(a) B_{12}= 0.1
(b) B_{12}= 0.5
(c) B_{12}= 1
(d) B_{12}= 5
(a)
(b)
(c)
(d)